INSTITUT POLYTECHNIQUE DE PARIS

NNT : 2020IPPAX072

Thèse de doctorat

ÉCOLE POLYTECHNIQUE

IP PARIS

Fragmentation of jets containing a J/ψ meson in pp and PbPb collisions at 5 TeV with the CMS detector

Thèse de doctorat de l'Institut Polytechnique de Paris
préparée à l'Ecole polytechnique

École doctorale n°626 Institut Polytechnique de Paris (IPP)
Spécialité de doctorat : Physique des particules

Thèse présentée et soutenue à Palaiseau, le 24/11/2020, par

BATOUL DIAB

Composition du Jury :

Yves Sirois Directeur de recherche, Laboratoire Leprince-Ringuet	Président
Roberta Arnaldi Chercheuse, Istituto Nazionale di Fisica Nucleare (INFN) - Sezione di Torino	Rapporteuse
Elena Ferreiro Professeur, Universidade de Santiago de Compostela	Rapporteuse
Andry Rakotozafindrabe Chargée de recherche, IRFU/DPhN, CEA Saclay	Examinatrice
Matthew Nguyen Chargé de recherche, Laboratoire Leprince-Ringuet	Directeur de thèse

My cartoon self makes a cameo appearance in this thesis (Sec. 3.1). When I added it, my friend asked me if it could cause me any problems since I don't look like a "standard" student here. This piece of work is dedicated to anyone who, at some point in their life or career, had to ask themselves a similar question, and for the people who didn't make me feel like I had to. No one should.

Batoul

Acknowledgements

I once read[1] that oneself is a collage of habits, ideas, styles, tics, hopes, and fears, that do not solely belong to us but are also a response to the other humans we interact with and the universe surrounding us. As a consequence, this piece of work is not just mine. It came to light thanks to the effort of many people that I want to thank here.

First, I want to thank my parents, who raised my siblings and me to try to be the best we can by only competing with ourselves and not others. They always pushed us to find our path in life and provided their support no matter what we chose. I want to thank my siblings, who requested to be thanked by name: Fayza, Hassan, Fatima, Narjess, Nour Al-Houda, and Ali. I always found at least one of you to ask for advice, to hug, or to share a laugh. Our bond is my pride and joy. That, of course, extends to all of your kids and families. I also want to thank my best friend, Malak, who is part of my family as well. We have been best friends for 25 years, and we will be for the rest of our lives.

I want to thank the people who made me survive five university years in the faculty of Sciences: Bouchra for all the exam nights we spent talking and not studying, Chourouk for being the better friend that deserved better than us, Fatima for listening to whatever I wanted to talk about even when she had no interest in it, Marwa for always pushing me to better myself, and Hiba for taking care of us. I want to also thank Marwa Jahjah for pointing me in the direction of particle physics.

For the years of my Ph.D., I want to first and foremost thank my supervisor, Matthew Nguyen, for giving me this opportunity. I truly believe that you are the best supervisor a student can get. Thank you for always being available whenever I had a question or needed help, for letting me express my opinions and concerns, and for rejuvenating my motivation whenever I wavered. You were my supervisor, office mate, and friend.
I also want to thank my colleagues at LLR: Inna, Javier, Mihee, François, Guillaume, Raphael, Tony, my mentor Deirdre, and all the students and researchers. Thank you for being welcoming and for the fun times we had together.

Lastly, I want to thank all the friends I made here in France: Laila for our discussions that made me see things from new perspectives, Hawraa for all the gatherings that made

[1] "I Am a Strange Loop" book by Douglas Hofstadter

us feel home even when we were far, Sakina, Hanine, and the rest for all the good times we had together. I want to thank the friends I made at CERN: Santona and Yeonju, and all my friends back home: Narjess, Zahraa(s), Batoul, Fatima(s), Hiba, and anyone who I might have forgotten.

Contents

Introduction

For years after its discovery, the electron was believed too small to be of interest to anyone outside a science lab. That, of course, has now changed. Many discoveries started by research that was purely driven by curiosity, and then led to new technologies that became an essential part of human life. Over the centuries, researchers have been pushing the boundaries of our understanding of the universe by exploring extreme limits: from the most fundamental constituents of the subatomic world to the biggest superclusters of galaxies in the universe.

One of the most successful theories of physics is the Standard Model, a framework that describes three of the four known fundamental forces of nature and classifies all known elementary particles. But despite its accuracy in describing many of the fundamental processes, there are still plenty of open questions to be answered.

The Standard Model describes the state of matter in nature as quarks and gluons confined in hadrons. Under extreme conditions, however, matter undergoes a phase transition to a plasma of quarks and gluons that are asymptotically free. The Quark-Gluon Plasma is believed to have existed microseconds after the Big Bang. It can be recreated in the laboratory when heavy nuclei are collided at high energies. Since the QGP has a short lifetime and cannot be directly seen, many particles are used as signatures of its formation and as tools to study its properties. One of them is a particle called "the J/ψ meson", made of a charm quark and its anti-quark. The production of the J/ψ, however, is still yet to be understood.

The goal of this thesis is to help better understand the J/ψ production in pp and PbPb collisions by measuring the fragmentation function of jets containing a J/ψ, i.e. checking the degree of isolation of the J/ψ meson while being produced.

Mainly, two analyses were done throughout this thesis. The first focused on the fragmentation of jets containing a J/ψ in pp collisions, both the prompt and nonprompt J/ψ components were reported. The second measured the fragmentation of jets containing prompt J/ψ mesons only, but in pp and PbPb collisions this time.

This manuscript is constructed as follows. Chapter 1 starts from the fundamental theory of Quantum-Chromodynamics to the questions that inspired this thesis, presenting the current status of our understanding of J/ψ production in hadronic collisions and its interaction with the QGP in PbPb collisions. Chapter 2 describes the machinery used to collect data for this study, starting with the Large Hadron Collider, then the Compact Muon Solenoid, going into the details of each of the subdetectors, the magnet system, and the trigger. Afterward, Chapter 3 describes the full procedure of measuring the frag-

mentation function, from the reconstruction of objects to the yield extraction and the determination of jet transverse momentum. The chapter also contains details about the datasets, the selection, and the corrections needed in the analyses. Finally, Chapter 4 and Chapter 5 contain the results of this thesis with a discussion about the physics and what could be done next to continue.

Chapter 1

From Quantum Chromodynamics to this thesis

1.1 The Quark-Gluon Plasma

1.1.1 Quantum chromodynamics

Quantum ChromoDynamics (QCD) is the theoretical framework dedicated to describing the strong interaction between quarks and gluons.
In analogy to QED, the theory that describes atomic interactions, the equivalent of the electrical charge is a property called color. The gluons are the force carriers, like photons are for the electromagnetic force. Similarly, a hadron is a composite made of quarks, held together by the strong force, like the molecules are held together with the electromagnetic force. For each color, there is an anti-color and the combination of each type of color charge (red + green + blue) is neutral. The quarks carry one color charge and the gluons carry a color and an anti-color which form an octet representation of SU(3). To form hadrons, which are colorless, a quark and an anti-quark can interact and form a bound state called a meson, or three quarks with one of each color charge can be bound together to form a baryon. Other larger combinations, such as the pentaquark, are also possible since they could also meet the colorless condition.

1.1.2 Confinement and deconfinement

The strong coupling constant, α_s, is the only free parameter of the Lagrangian of quantum chromodynamics if we consider the quark masses as fixed [1]. Fig. 1.1 shows that α_s decreases with the increase of the momentum transfer Q. The strong coupling vanishes when $Q \to \infty$, a phenomenon known as asymptotic freedom. When Q is close to the QCD scale ($\Lambda_{\mathrm{QCD}} \sim 200\,\mathrm{MeV}$) the coupling constant becomes large. This is the case inside hadrons where the coupling becomes too strong that it is impossible to isolate a quark from a hadron. This mechanism is known as confinement.
Due to this phenomenon, quarks and gluons have never been observed isolated in normal conditions. However, QCD lattice calculations [2] indicate that above a critical tem-

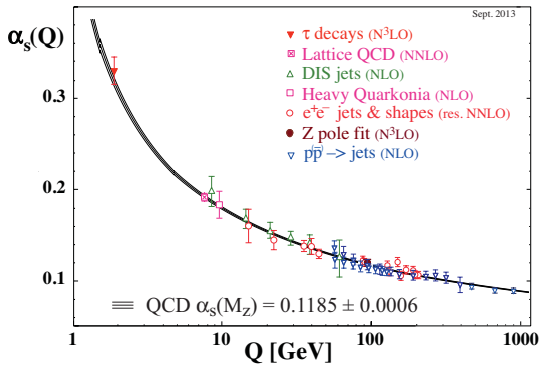

Figure 1.1: Current experimental status of the running of the strong coupling constant α_s with the momentum transfer Q [1].

perature, T_c, or energy density, ε_c, strongly interacting matter undergoes a phase transition to a new state where the quarks and gluons are no longer confined in hadrons [3]. The energy density is shown as a function of the temperature from lattice QCD calculations in Fig. 1.2.

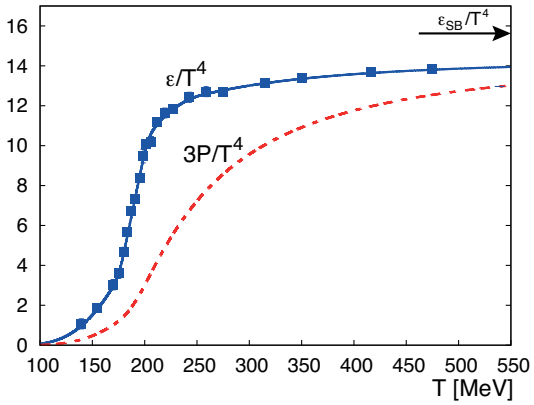

Figure 1.2: Energy density ε/T^4 (blue) and pressure $3P/T^4$ (red) as function of the temperature T from lattice calculations. The arrow indicates the Stefan Boltzmann limit of the energy density [4].

The jump in the energy density around $T_c \sim 200$ MeV, $\varepsilon_c \sim 1\,\mathrm{GeV/fm^3}$, indicates a jump in the degrees of freedom and sequentially a phase transition from hadronic matter to a state of matter is compared to a soup of quarks and gluons and called the Quark-Gluon Plasma, the QGP [5].

1.1.3 Experimental study of the QGP

Microseconds after the Big Bang, matter existed in the form of quark-gluon plasma. To recreate conditions similar to the early universe, powerful accelerators collide heavy nuclei to form many small fireballs in which the nucleons "melt" into a quark-gluon plasma. The following sections will explain, in detail, how the QGP forms in heavy-ion collisions and what are the tools used to study its properties.

Relativistic heavy-ion collisions

To create the de-confined state of matter, the conditions of high energy density and temperature should be reached. Heavy-ion colliders smash heavy nuclei at high energies such that the nucleons in the nuclei collide at energies of a few trillion electronvolts each, creating a high-temperature but low-density medium that allows a smooth crossover of the matter from hadronic to the QGP [6]. In 2000 CERN announced the discovery of a "new state of matter in heavy-ion collisions at the SPS" that "features many of the characteristics of the theoretically predicted quark-gluon plasma" based on many measurements from different experiments [7]. RHIC followed, in 2005, by publishing four papers summarizing the findings from the first three years of data [8, 9, 10, 11]. The creation of a new state of matter was confirmed in heavy-ion collisions.

Geometry of the collision A nucleus is an extended object made of nucleons, i.e. protons and neutrons. When colliding nuclei, the number of nucleon-nucleon interactions is highest when the collision is "head-on". In this case, the collision is called central and the nuclei overlap completely, as opposed to peripheral collisions where the nuclei only overlap partially. Since the QGP is formed in the overlap region, the collision centrality determination is of particular importance in heavy-ion physics results.

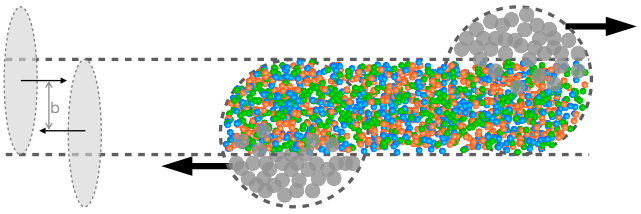

Figure 1.3: Illustration of two nucleus before and after the collision, adapted from Ref. [12]

Fig. 1.3 illustrates two colliding nuclei. The impact parameter, b, is the distance between the centers of the nuclei. It is a key characteristic of the collision's geometry. And it can take values from 0 to the sum of the radii of the two nuclei.
The number of participating nucleons that undergo at least one inelastic collision (N_{part}) and the number of binary nucleon-nucleon collision (N_{coll}) are both important quanti-

ties that cannot be determined directly from measured cross-sections. They can be determined, however, with a well-defined theoretical procedure called the Glauber model [13], which provides these abstract quantities averaged within "centrality classes". The Glauber model calculations have two main classes: the "optical limit" calculations where a smooth matter density is assumed inside the nuclei, and the "Glauber Monte Carlo" where the nucleus is modelled as uncorrelated nucleons sampled from measured density distributions.

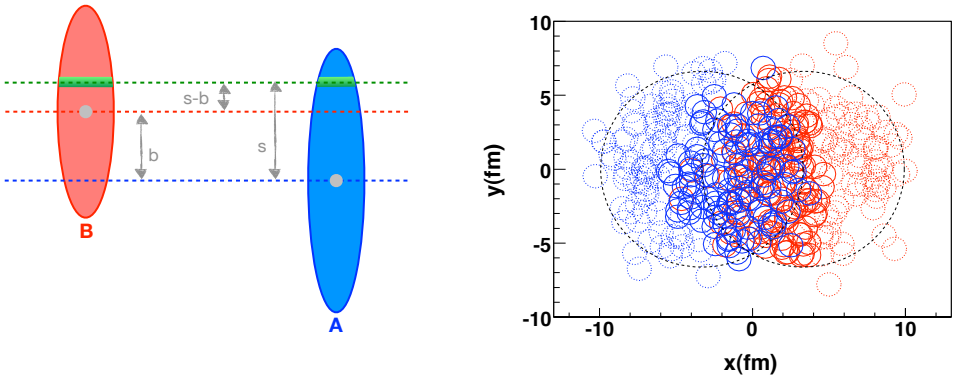

Figure 1.4: Left: Schematic view of the initial geometry of two collided ions A and B separated by an impact parameter b, adapted from Ref. [13]. Right: An example of a PbPb collision at LHC with $b \approx 7$ fm. The participants are indicated as solid circles [14].

In the left panel of Fig. 1.4, two nuclei A and B, with A and B nucleons respectively, are colliding with an impact parameter b, as described by the optical Glauber model geometry The tube located at a distance $\vec{s}$ from the center of the nucleus A overlaps with another tube in the nucleus B located at $\vec{s} - \vec{b}$ from the center. The thickness function of the nucleus is defined as the density of nucleons ρ per unit area $dxdy$ along the direction z at a distance $\vec{s}$ and, for the nucleus A, can be expressed as:

$$T_A(s) = \int dz \rho_A(s,z), \text{ normalized so that } \int d^2s T_A(s) = A \tag{1.1}$$

where ρ is the nuclear density distribution in a given nucleus, usually parameterized by a Wood-Saxon distribution [13]. The nuclear overlap function can then be defined as:

$$T_{AB}(b) = \int d^2s T_A(s) T_B(s-b) \tag{1.2}$$

N_{coll} and N_{part} for a given impact parameter b are then defined as:

$$N_{coll}(b) = AB\ T_{AB}(b).\sigma_{nn}^{inel} \tag{1.3}$$

$$\begin{aligned} \mathrm{N_{part}}(b) =& \mathrm{A} \int d^2s T_A(s) \left(1 - \left[1 - T_B(s-b)\sigma_{\mathrm{nn}}^{\mathrm{inel}}\right]^B\right) \\ &+ \mathrm{B} \int d^2s T_B(s-b) \left(1 - \left[1 - T_A(s)\sigma_{\mathrm{nn}}^{\mathrm{inel}}\right]^A\right) \end{aligned} \tag{1.4}$$

where $\sigma_{\mathrm{nn}}^{\mathrm{inel}}$ is the inelastic nucleon-nucleon cross section.
The nuclear overlap function can be thought of as the nucleon-nucleon luminosity (reaction rate per unit cross section) in an AB collision at a given impact parameter b.
The right panel of Fig. 1.4 shows an example of a PbPb collision at the LHC where the nucleons have a more realistic representation in the nuclei, described by the Glauber Monte Carlo. The participants are drawn with solid circles while the dashed circles show the spectators, i.e. the nucleons that do not experience any inelastic collision.
In heavy-ion experiments, $\mathrm{N_{coll}}$, $\mathrm{N_{part}}$ and T_{AA} cannot be determined directly. The events are classified into centrality classes (procedure explained in Section. 3.3), and the mean parameters $\langle \mathrm{N_{coll}} \rangle$ and $\langle \mathrm{N_{part}} \rangle$ are obtained by performing Monte Carlo Glauber simulations.

Evolution of nuclear collision The time evolution of a nucleus-nucleus collision is represented in Fig. 1.5.

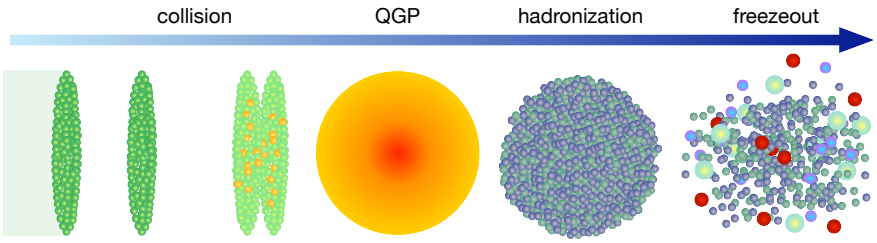

Figure 1.5: Schematic illustration of the evolution of a relativistic heavy-ion collision.

It can be described as follows:

- In the laboratory frame, the two incoming nuclei are Lorentz contracted. Parton scatterings start at this stage. Hard processes take place.
- The parton interactions start producing new particles increasing the density of the system. This can lead to the formation of the QGP. The system then starts to expand and cool down.
- When the system cools down to the critical point, hadrons start forming.
- The chemical freezeout is reached when no more inelastic interactions are taking place. After this point, the number of hadrons stays unchanged. Then a kinetic

freezeout is reached when no more elastic interactions take place, fixing the kinematic distributions of the hadrons.

Probing the QGP

Since the QGP only exists for a very short time, it cannot be measured directly. But it can be studied indirectly by measuring how certain particles are modified by its presence. Those particles are called probes or signatures of the QGP. They are separated into soft and hard probes depending on the momentum of their production processes.

Soft probes The majority of particles produced in the collisions are soft particles. They are used to study the thermal and hydrodynamical evolution of the medium. As examples, the elliptic flow and the strangeness enhancement are discussed in the following part.

- **Elliptic flow**: In non-central heavy-ion collisions, the colliding matter takes an oval shape as shown in Fig. 1.6. This shape causes an azimuthal anisotropy for the coordinate and momentum distributions. The azimuthal anisotropy in particle production is the clearest experimental signature of collective flow in heavy-ion collisions [4]. The elliptic flow (v_2) is the second coefficient of the Fourier expansion of the azimuthal distribution with respect to the reaction plane, defined by the beam axis and the impact parameter vector of the colliding nuclei. The triangular flow (v_3) is the third coefficient and the quadrangular (v_4) is the fourth [15].
  The anisotropic flow is especially sensitive to the early stages of system evolution,

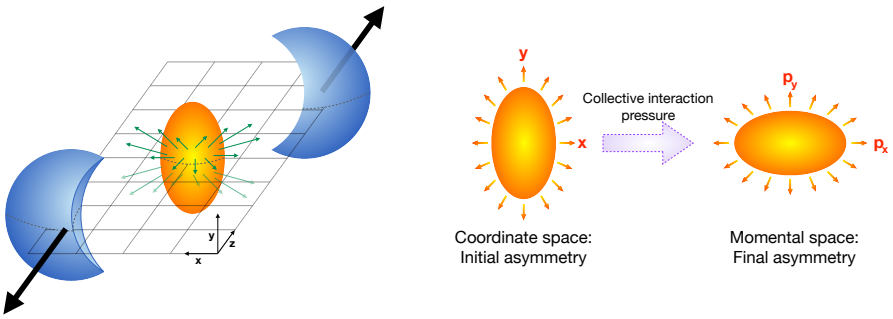

Figure 1.6: A schematic representation of the collision zone between two incoming nuclei with initial- and final-state anisotropies in the collision zone in the coordinate and momental space respectively, adapted from Ref. [16]

making it an important observable when studying the hydrodynamical properties of the expanding medium such as the viscosity and temperature. However, the anisotropic flow can also be affected by the late-stage interactions and resonance decays.

- **Strangeness enhancement**: The quantum number called strangeness quantifies the number of strange quarks in a decay. It can take values of 1 for strange quarks, -1 for the strange anti-quarks, and 0 for the other quarks. Due to the higher mass of strange quarks, strange hadrons are less abundant than light quark hadrons, like pions, in pp collisions. In heavy-ion collisions, however, the large gluon density in the QGP enhances the production of $s\bar{s}$ pairs via gluon fusion. At high collision energies, the strange quarks can also bind to b and c quarks, producing strange hadrons like kaons or D_s. Enhanced production of strange hadrons in heavy-ion has been observed by many experiments like WA97/NA57 [17, 18] at SPS, STAR [19] at RHIC, and ALICE [20] at the LHC.

Hard probes They are ideal tools to study the structure of the system since they are believed to be produced early in the collision and to often live through the QGP. In the following sections, important examples of hard probes are discussed: jets, electroweak bosons, and heavy flavor production.

- **Jets**: During hadronic collisions, partons can scatter with very large momentum transfers. The partons quickly radiate gluons which split into multiple quarks that form hadrons. The produced hadrons tend to move along the same direction as the original fragmented parton, forming a localized spray of particles called a jet. In heavy-ion collisions, if the jets are formed in the center of the collision, they have to traverse the medium before they escape. The energy of the jets is attenuated and the jets are considered quenched by the medium.
  Jets are found by identifying a fast hadron, called the trigger, and associated hadrons within a selected p_T threshold. Measuring the azimuthal angle of the associated hadrons relative to the jet indicates a strong correlation with the leading particle.

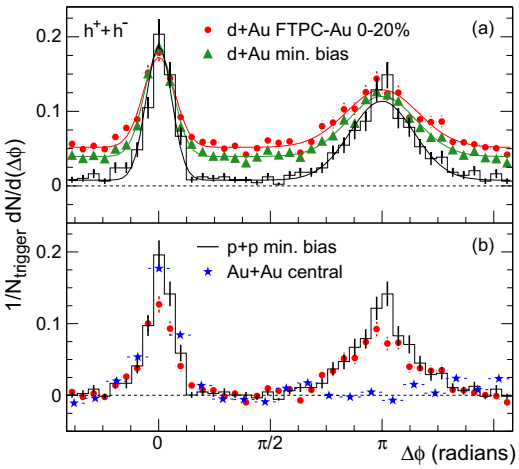

Figure 1.7: two-particle azimuthal distributions [21].

Fig. 1.7 shows the azimuthal angle ($\Delta\phi$) between high momentum hadrons in dAu, pp and AuAu collisions [21]. In all systems, a narrow peak, a jet, is found centered around $\Delta\phi = 0^o$. Momentum conservation would suggest a second peak at $\Delta\phi = 180^o$, which is seen clearly in pp and dAu collisions but is absent in AuAu collisions. This is consistent with a picture in which one jet is usually produced near the surface and the other jet needs to traverse the medium and is then completely absorbed.

- **Electroweak bosons**: Photons, $W^{\pm}$ and Z are the electroweak bosons. They do not have color charges, thus are not affected by the strongly interacting medium. They are created in the initial hard collisions, so they are used as clean probes of nuclear effects other than the QGP. They are also used as controls to estimate the initial transverse momentum of recoil partons [22, 23].

- **Heavy flavor production**: Hadrons containing heavy quarks, *b* and *c*, are believed to probe the whole phase of the QGP due to the early production of their constituents. The effect of the hot medium is studied by measuring the nuclear modification factor, R_{AA}.
  R_{AA} is the ratio that compares the per-event yield in heavy-ion collisions to the expectation from pp collisions, by scaling the cross section of the latter by T_{AA}, the average effective nucleon-nucleon luminosity delivered by a single heavy ion collision for a given centrality selection. In the absence of nuclear effects $R_{AA} = 1$. Fig. 1.8 shows the R_{AA} of some heavy-flavor hadrons compared to charged hadrons

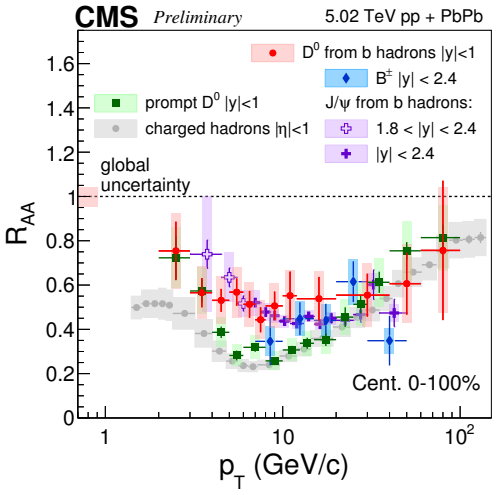

Figure 1.8: R_{AA} of charged hadrons [24], D^0 [25], $B^{\pm}$ [26], and J/ψ coming from b hadron decays [27].

that consist mainly of light flavor. The dominant contributions to charged hadrons

are pions[1], kaons[2] and protons. They are all made of light quarks.
On the heavy flavor side, D^0 is the meson made of a charm quark and an up antiquark. The B^+ meson is made of a charm quark and a beauty antiquark, B^- being its anti-particle. J/ψ is the meson made of a charm quark and its antiquark.
The R_{AA} shows suppression of heavy flavor over the p_T spectrum. While traversing the plasma, the heavy quarks interact with the partons radiating gluons and losing energy. This process is called radiative E_{Loss} as opposed to the collisional E_{Loss} where the gluons interact with the QGP before forming the quarks at later times. Since massive quarks are predicted to lose less energy than light partons, the R_{AA} shows less suppression for heavy-flavor hadrons when compared to light hadrons.

- **Quarkonium production**: Quarkonium states are the bound states of $c\bar{c}$ and $b\bar{b}$, called charmonia and bottomonia respectively. In the presence of a hot deconfined medium, the bound states dissociate causing the suppression of quarkonia in heavy-ion collisions compared to pp. The mechanisms causing the dissociation will be explained in detail in the next section when discussing the most abundant charmonium state, called the J/ψ meson.

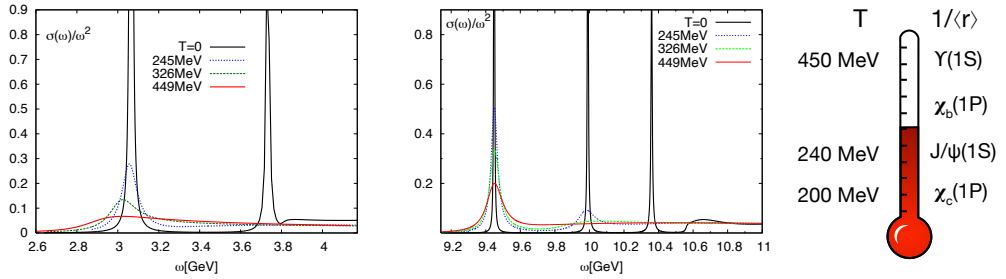

Figure 1.9: Charmonium (left) and bottomonium (middle) spectral functions calculated in a potential model with complex potential, and a cartoon of the QGP thermometer (right) provided by the sequential melting of quarkonia [28].

Quarkonium suppression happens sequentially: strongly bound states require a higher temperature to dissociate than loosely bound states. A certain state's melting can also be affected by the melting of more excited states because they feed down to less excited states. The sequential melting can be clearly seen in Fig. 1.9, where the spectral functions of charmonia and bottomonia are shown at different temperatures. With increasing temperature, the peak gets wider and shifts slightly to lower ω until it gets completely suppressed, starting with the more excited, thus

[1]Pions (π^0 and $\pi^\pm$) are the lightest hadrons. They consist of a quark and an antiquark. The quarks can be up or down quarks or their antiquarks

[2]Kaons are the bound states of a strange quark (or antiquark) and an up or down antiquark (or quark)

more loosely bound, states. The study of the QGP can thus be measured using quarkonia as a thermometer as shown in Fig. 1.9 on the right.

1.2 J/ψ production in heavy-ion and pp collisions

The J/ψ meson was discovered independently by two research groups [29, 30] granting a Nobel prize for both group leaders. The discovery was considered revolutionary at the time since it established the quark model as a credible description of nature. Fig. 1.10 shows the charmonium states with selected decay modes and transitions [31], with the J/ψ highlighted in red.

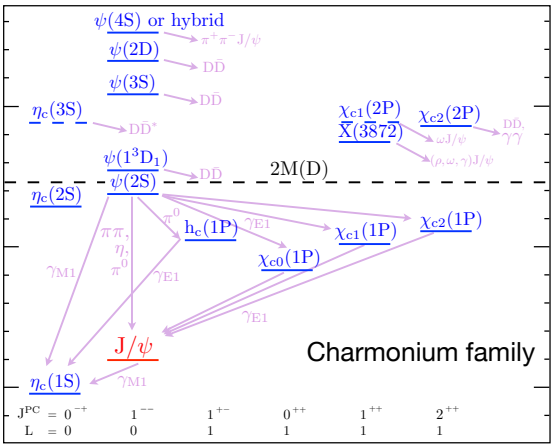

Figure 1.10: Known charmonium states and candidates, with selected decay modes and transitions, based on the figure in Ref. [31].

The J/ψ has a rest mass of 3.0969 GeV/c^2, a mean lifetime of 7.2×10^{-21} s, and a spin of 1 [32]. The J/ψ can decay leptonically or hadronically with the branching ratios shown in Table 1.1.

Decay channel	branching ratio (%)
$\mu^+\mu^-$	5.961 ± 0.033
e^+e^-	5.971 ± 0.032
hadrons	87.7 ± 0.5

Table 1.1: Branching ratios for decays of the J/ψ meson [32]

1.2.1 J/ψ in heavy-ion collisions

When a $c\bar{c}$ pair is produced in a nuclear collision that results in a quark-gluon plasma, the $c\bar{c}$ finds itself in a deconfining environment where quarks and gluons are not confined in color-neutral hadrons. The interaction between quarks, mediated by gluons, is screened

by the color charges in the medium. This phenomenon is known as Debye screening [33]. If the temperature of the medium is sufficiently high the screening radius, $r_D \propto 1/T$, becomes smaller than the binding radius between the $c\bar{c}$ and the resonance interaction to form the binding state cannot take place. The production of J/ψ is then prohibited which causes its suppression [34]. Since J/ψ can be produced by the feed down of excited states, some of the J/ψ suppression could also be caused by the melting of excited states.
Figure 1.11 shows the R_{AA} of J/ψ in AuAu collisions, measured by the PHENIX experiment at 0.2 TeV, in two rapidity ranges. It shows suppression of J/ψ in all centrality bins.

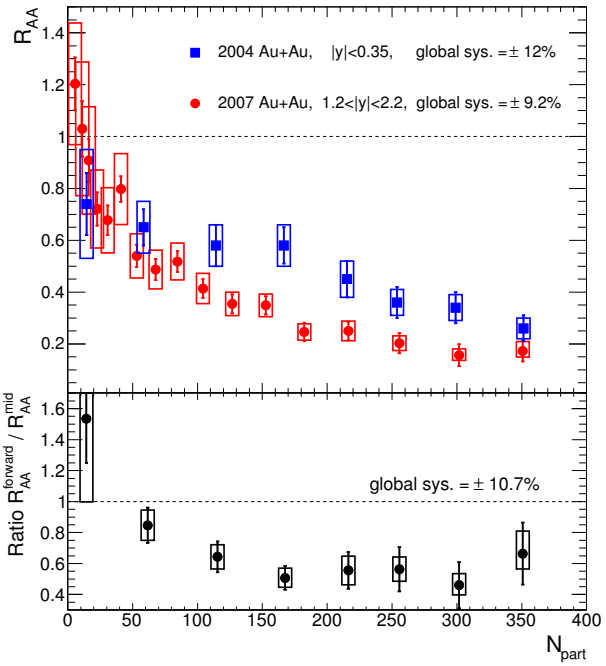

Figure 1.11: The nuclear modification factor (R_{AA}) for inclusive J/ψ as a function of the number of participants in AuAu collisions with the PHENIX detector [35].

At high collision energy, there is a significant number of initially produced charm and anti-charm quarks in the medium which could come close enough in phase space to form a charmonium state. J/ψ mesons can thus be regenerated in the most central collisions from the combination of initially uncorrelated charm quarks. Since the charm density increases with the center-of-mass energy, the recombination effect is important at higher energies [36]. This is shown in Fig. 1.12 where the R_{AA} of J/ψ at three energies is shown: AuAu collisions at 0.2 TeV by PHENIX and PbPb collisions at 2.76 and 5.02 TeV by ALICE. The enhancement at higher energies at low p_T is caused by the regeneration of J/ψ states.

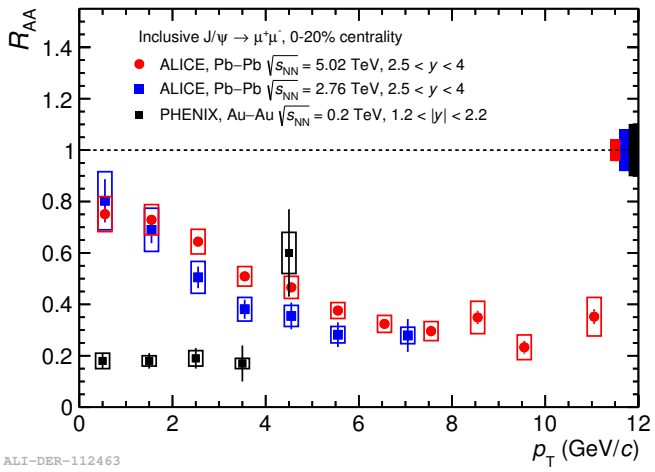

Figure 1.12: R_{AA} for inclusive J/ψ as a function of p_T in PbPb collisions with the ALICE detector [37, 38] and in AuAu collisions with the PHENIX detector [39].

1.2.2 Cold nuclear matter effects

In addition to the hot medium, the J/ψ meson is affected by the Cold Nuclear Matter (CNM) present in the collision [40]. The CNM effects are studied in pPb collisions where the QGP is not expected to form. Understanding CNM effects is important to be able to characterize the QGP produced in heavy-ion collisions. For brevity, the CNM effects are not going to be discussed in detail in this thesis. Instead, the following is a list of the main effects with references that provide more information:

- Nuclear absorption: When the $c\bar{c}$ pair is traveling through the nucleus it might scatter with the target nucleons. This can break the charm quarks that can then hadronize into open-charm mesons [41].

- Gluon shadowing: The Parton distribution functions (PDFs) represent the probability of finding a parton with a specific flavor carrying fraction x of the colliding hadron's longitudinal momentum at a given energy scale Q. The x-range of charmonia in the CMS rapidity is in the shadowing region of the nuclear PDFs leading to a suppression of the charmonium production [42, 43].

- Energy loss and Cronin effect: High-energy partons can lose energy while traversing the nuclear medium through gluon radiation. The partons can also gain transverse momentum when they undergo elastic scatterings in the nucleus. This effect is known as the Cronin effect [44, 45].

1.2.3 J/ψ hadroproduction

In hadronic collisions, the J/ψ meson is produced from different sources. J/ψ mesons can be produced directly in the initial hard scattering or from the decay of higher mass charmonium states. These J/ψ are called prompt. J/ψ mesons can also be the product of weak decays of b hadrons. In this case, they are called nonprompt.

Nonprompt J/ψ production

At the LHC, bottom quarks are mainly produced via gluon fusion $gg \rightarrow \mathrm{b} + \bar{\mathrm{b}} + \mathrm{X}$, and then form b mesons and baryons. Theoretically, the cross section of a b hadron is factorized into two processes: the b quark production which is a perturbative process evaluated using Fixed Order Next-to-Leading-Logarithm (FONLL) calculations [46], and the fragmentation into the hadron which is a nonperturbative process usually extracted from $\mathrm{e}^+\mathrm{e}^-$ experimental data [47]. An example of a weak decay of b hadron that produces a nonprompt J/ψ is shown in the diagram in Fig. 1.13.

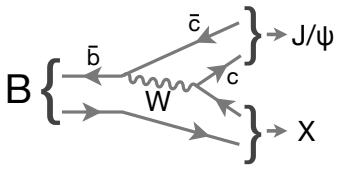

Figure 1.13: A Feynman diagram of a LO contribution to the weak decay of a B hadron into a J/ψ, adapted from the figure in Ref. [48].

The branching ratio of B $\rightarrow$ J/ψ + X, with B as the mixture of all b mesons and baryons, is measured at the LHC, LEP, Tevatron and Sp$\bar{\mathrm{p}}$S and is found to be (1.16$\pm$0.10)% [32].

Prompt J/ψ production

The production of prompt J/ψ is theoretically assumed to be factorized into two processes. The first is the perturbative process to produce charm pairs. The second is the nonperturbative process of the hadronization of the charm quarks into a bound state of J/ψ. Nearly all quarkonium production models introduce this factorization between the pair production and its binding. They mainly differ however in their treatment of the hadronization. Some may also introduce new ingredients in the description of the $c\bar{c}$ production. In the following sections, three quarkonium production models are explained: the Color Singlet Model (CSM), the Color Evaporation Model (CEM), and Nonrelativistic QCD (NRQCD).

The Color Singlet Model It was the first model to describe quarkonium production when proposed in 1975 to describe the hadroproduction of η_c mesons [49]. It assumes that the quantum state of the quark pair does not evolve between its production and

its hadronization, neither in spin nor in color. To eventually form a J/ψ, this model requires the $c\bar{c}$ pair to be produced in a color singlet state. It also considers quarkonia as non-relativistic bound states, neglecting the relative momentum of the quarks inside the hadron.
The partonic cross section for quarkonium production should be expressed as that for the production of a heavy-quark pair with zero relative velocity, v, in a color-singlet state and in the same angular-momentum and spin state as that of the to-be produced quarkonium, and the square of the Schrödinger wave function at the origin in the position space.
To get the hadronic cross section, the parton densities of the colliding hadrons need to be taken into account. NLO and NNLO contributions to the CSM are significantly larger than the LO contributions at mid and large p_{T} and they should systematically be accounted for in any study of their p_{T} spectrum [50].

The Color Evaporation Model In this model [51], the probability of forming a specific charmonium (quarkonium in general) state is assumed to be independent of the color of the $c\bar{c}$ pair. It does not specify the color or spin state of the produced $c\bar{c}$ pairs and allows the quantum states of the $c\bar{c}$ to change during its evolution. nonperturbative-gluon emissions can occur once the $c\bar{c}$ pair is produced.
All pairs with mass less than open heavy flavor threshold become quarkonium. Thus the CEM cross section is simply the $c\bar{c}$ production cross section with a cut on the pair mass. The color and spin are integrated over so that the color of the state is said to have been 'evaporated' away without changing the kinematics of the pair. The production cross section is obtained by multiplying with a factor $F_{\mathcal{C}}$, which is related to a process-independent probability that the pair eventually hadronizes into this specific state. It is calculated statistically under the assumption that one-ninth -one colour-singlet $c\bar{c}$ configuration out of 9 possible- of the pairs in the suitable kinematical region hadronizes into a quarkonium. The actual value of $F_{\mathcal{C}}$ depends on the heavy quark mass, the scale parameters, the parton densities, and the order of the calculation.

Nonrelativistic QCD The NRQCD factorization approach incorporates aspects of both the CSM and CEM and can be regarded as a unification of these two models within a consistent theoretical framework [52]. Unlike the CSM, it does not assume that the quarks are produced in their final color state. The $c\bar{c}$ can be produced in a color-singlet or color-octet state. The color-singlet diagrams dominate low p_{T}, but at large p_{T}, the production is dominated by color-octet diagrams. The nonperturbative hadronization probability of the $c\bar{c}$ into a J/ψ is calculated using long-distance matrix elements (LDMEs) that are process independent and can be constrained by fitting experimental data [53].
Examples of diagrams contributing to the production of J/ψ, via color-singlet and color-octet channels, are shown in Fig. 1.14.

J/ψ **puzzle** Despite the big progress made in the understanding of J/ψ production, the picture is not complete [54].

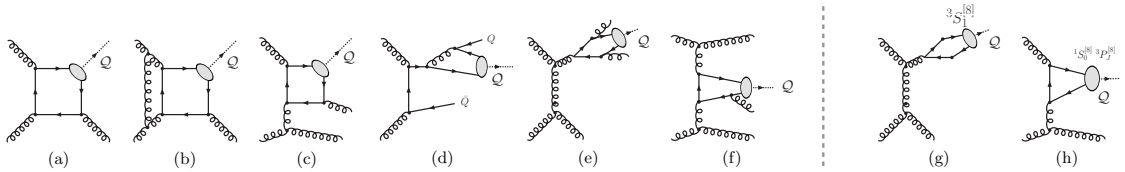

Figure 1.14: Feynman diagrams contributing to a quarkonium state (noted $\mathcal{Q}$) via color-singlet channels at LO (a), NLO (b,c,d) and NNLO (e,f), and via color-octet channels at LO (g,h) [50].

When compared to experimental data, none of the previously mentioned models manages to reproduce both the J/ψ cross section and the polarization measurements. The incompatibilities between models and data started in the mid 90's when the measured cross section of the J/ψ meson in p$\bar{\text{p}}$ collisions at 1.8 TeV by the CDF experiment was an order of magnitude larger than leading order (LO) CSM calculations [55]. CEM has a successful phenomenology but it lacks the predictions for the polarization. It also fails to describe some experimental discrepancies like the observed differences between the hadroproduction and photoproduction measurements [56]. Lastly, NRQCD is successful in describing many charmonium observables including the J/ψ production cross sections at different LHC energies [57] but it fails to describe the J/ψ polarization results [58]. In Fig. 1.15, on the left, the prompt J/ψ yields measured by the LHCb at 7 TeV [57] are compared to NLO NRQCD, NLO, and NNLO* CSM and NLO CEM predictions. The CSM cross sections are an order of magnitude smaller than data and CEM predictions diverge at large p_{T}. The NRQCD, however, manage to reproduce the experimental cross section for mid and larget p_{T} within the uncertainties. The right panel shows the comparison of the transverse polarization parameter λ_θ as a function of p_{T} of LHCb data [58] to the NRQCD and CSM predictions. NRQCD show mostly positive or zero values of λ_θ with a trend towards the transverse polarisation with increasing p_{T}, while NLO CSM predicts an increasingly longitudinal yield with p_{T}. None of these predictions correctly describes the measured polarization parameter and its p_{T} trend.

1.2.4 Fragmentation of J/ψ in jets

The classic picture of J/ψ production relies on the assumption that the J/ψ is produced directly in the parton-parton scattering. This direct-production paradigm predicts that J/ψ mesons are largely produced isolated, except for any soft gluonic radiation emitted by the $c\bar{c}$ state.
To test this prediction the LHCb collaboration studied the production of J/ψ within jets in pp collisions [66], where the fraction of the jet transverse momentum carried by the J/ψ, $z \equiv p_{\text{T}}(\text{J}/\psi)\,/\,p_{\text{T}}(jet)$, is measured for prompt and nonprompt J/ψ at 13 TeV.
The results, shown in Fig. 1.16, compare the normalized z distributions for prompt and

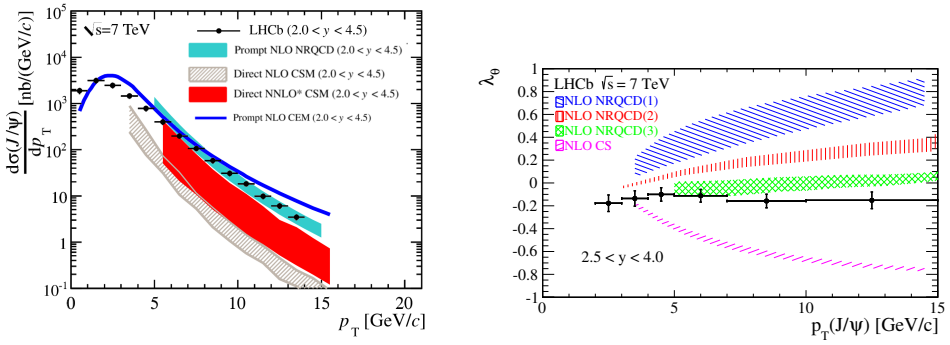

Figure 1.15: Left: Prompt J/ψ yield as measured by LHCb [57] at 7 TeV compared to different theory predictions: Prompt NLO NRQCD [59], Direct NLO CSM [60], Direct NNLO* CSM [61] and Prompt NLO CEM [62]. Right: Polarisation parameter λ_θ for prompt J/ψ from LHCb [58] compared to different model predictions: direct NLO CSM [63] and three NLO NRQCD calculations [63, 64, 65].

nonprompt J/ψ to the NRQCD predictions implemented in PYTHIA 8. The nonprompt results are consistent with the PYTHIA 8 prediction, where both data and simulation show a sizeable jet activity accompanying the J/ψ. However, for the prompt component, a discrepancy is seen between data and the LO NRQCD-based prediction implemented in PYTHIA 8, which includes both color-octet and color-singlet mechanisms. Prompt J/ψ are observed to be much less isolated in data than predicted by LO NRQCD.

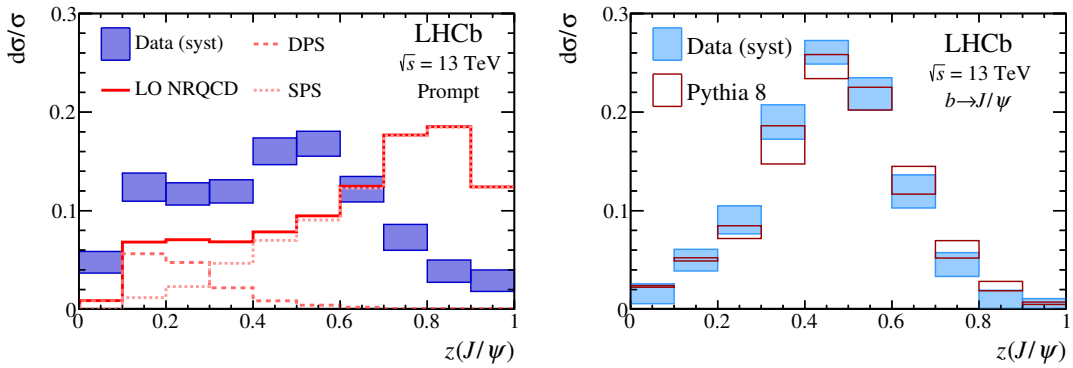

Figure 1.16: z distributions for prompt (left) and nonprompt (right) J/ψ compared to predictions obtained from PYTHIA 8. The (DPS) double and (SPS) single parton scattering contributions to the prompt prediction are also shown [66].

An alternative to the standard production approach, also based on NRQCD, is the J/ψ production within parton showers [67], or within jets. In this approach, analytical calculations were performed to next-to-leading-log-prime (NLL'). To understand NLL' cal-

culations, one can compare to leading-order calculations like the ones implemented in PYTHIA. As explained in the previous section, In LO and NLO order NRQCD models, the $c\bar{c}$ pair is a short distance perturbative process via color-singlet or color-octet channels. In the color singlet channel, no gluon radiation is emitted. On the other hand, the color-octet quark-antiquark emits soft gluon radiation.
In NLL' calculations, a hard gluon is first produced in the short-distance process with a virtuality of the order of a jet energy scale (E_J). The gluon is allowed to shower until one of the gluons in the shower reaches a virtuality comparable to two times the mass of the c quark. The gluon then hadronizes producing a J/ψ.
These calculations can be implemented in PYTHIA using two methods. The first is Gluon Fragmentation Improved PYTHIA (GFIP), where events corresponding to hard production of c are generated using MadGraph [68], then PYTHIA is used to shower the event down to a scale of $\sim 2m_c$, where jets are reclustered using jet algorithms like the anti-k_T. The second method is the Fragmentation Jet Function (FJF), where the jet fragmentation functions are combined with hard events generated at LO. It starts backward, by resumming the logarithms of $m_{J/\psi}/E_J$ from the scale of $2m_c$ to E_J. MadGraph then continues with the factorization with LO perturbation processes.

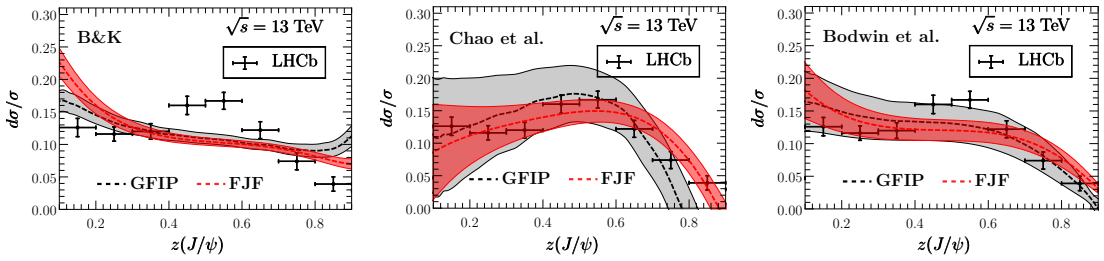

Figure 1.17: Predicted z distribution using GFIP (gray) and FJF (red) for three choices of LDME and the LHCb measurements of z [67].

The z distributions predicted by this approach, calculated using both GFIP and FJF methods are shown in Fig. 1.17 for three choices of NRQCD LDME: B&K [69, 70], Chao et al. [65], and Bodwin et al. [71]. When compared to the LHCb data for prompt J/ψ at 13 TeV, these calculations showed a better agreement with data than PYTHIA 8.
In this new approach, the J/ψ is produced at later times than what is assumed in the classic picture. This doesn't just change J/ψ production in pp collisions. It can also change our interpretation of J/ψ results in HI collisions. The interpretation of the J/ψ R_{AA} results in nucleus-nucleus collisions relies on the assumption that the c and $\bar{c}$ are produced before the formation of the QGP and are then screened when the hot medium is created which causes the suppression of the J/ψ meson.
On the left of Fig. 1.18 the R_{AA} of prompt J/ψ is shown, in orange, as a function of p_T [27]. The R_{AA} shows a rising trend at high p_T that is similar to what is seen in open charm

R_{AA}, also shown in green [25]. This rising trend was also seen for charged hadrons and was previously shown in Fig. 1.8 in section 1.1. The R_{AA} of charged hadrons along with D and J/ψ mesons is shown in the left panel of Fig. 1.18 as a function of $p_T/n\omega_c$ where n is a power-law index and ω_c is a medium characteristic that scales with the transport coefficient of the medium and its length squared. This shows a "universal" trend of R_{AA} that is also compared to an energy loss (E_{Loss}) model [72]. The compatibility of data with the model emphasizes the role E_{Loss} processes in the suppression J/ψ.

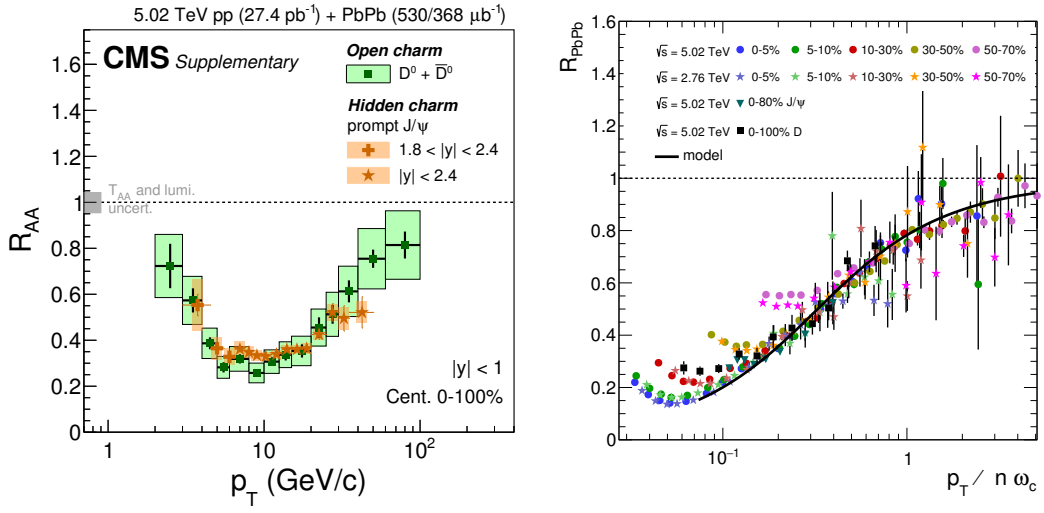

Figure 1.18: Left: R_{AA} of J/ψ [27] compared to D^0 and $\bar{D}^0$ [25]. Right: R_{AA} of $h^{\pm}$, D and J/ψ as a function of $p_T/n\omega_c$ in PbPb collisions at $\sqrt{s_{NN}} = 2.76$ TeV and $\sqrt{s_{NN}} = 5.02$ TeV in different centrality classes compared to E_{Loss} model [72].

This interpretation can also be used for the J/ψ v_2 measurements. As seen in the left panel of Fig. 1.19, a nonzero v_2 of J/ψ is measured by ATLAS [73] and CMS [74] for prompt J/ψ and ALICE [75] for inclusive J/ψ mesons, up to 30 GeV. At low p_T, v_2 comes from the collective flow of bulk particles. This is not expected to the case at high p_T. The comparison of prompt J/ψ v_2 to that of D mesons [76] and charged hadrons [77, 78] on the left of Fig. 1.19 shows a lower value for J/ψ at low p_T. At high p_T, however, all three results are similar within the uncertainties. These results hint at a flavor independence of the energy-loss path-length dependence.
The E_{Loss} interpretation of J/ψ suppression is compatible with the production of J/ψ in a parton shower, where the parton loses energy by interacting with the QGP before the J/ψ is even formed.

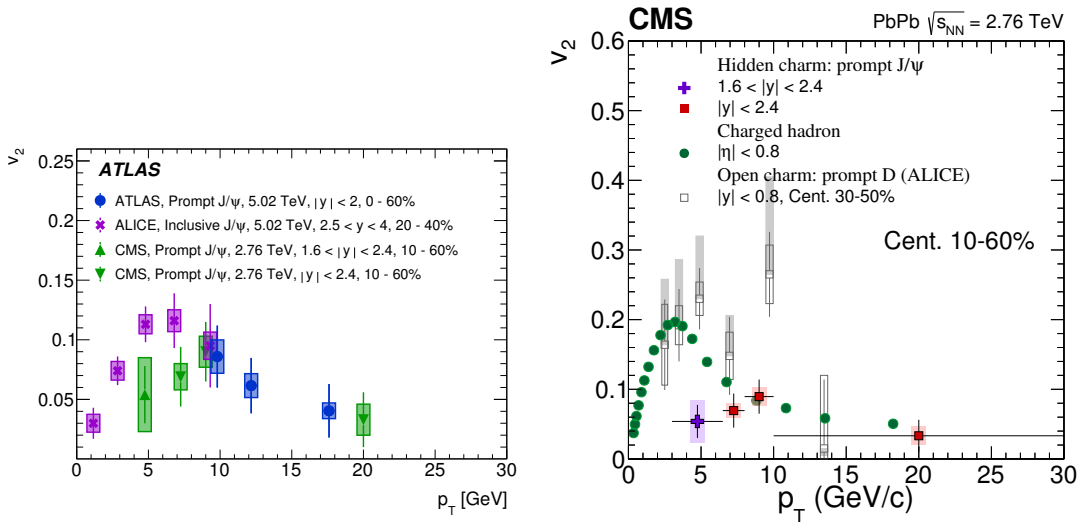

Figure 1.19: Left: Results for v_2 as a function of the transverse momentum of prompt J/ψ as measured by ATLAS [73] at 5.02 TeV and CMS [74] at 2.76 TeV compared with inclusive J/ψ measured by ALICE at 5.02 TeV [75]. Right: Prompt J/ψ [74], D [76], and charged hadron [77, 78] v_2 vs. p_T.

1.3 The plan of contribution of this thesis to J/ψ production

The goal of this thesis is to contribute to the J/ψ production puzzle by measuring the fragmentation of jets containing J/ψ mesons.
We decided to split the work into two analyses. First, we measure the fragmentation function of J/ψ-jets in pp collisions at mid rapidity, closely following the procedure by the LHCb collaboration [66] for which the results are shown in Fig. 1.16. These results are used to understand charmonia without the suppression caused by the presence of a hot medium, like in the case of PbPb.
After that, we push it to the next level, by measuring the fragmentation function in PbPb collisions and comparing it to pp, focusing on prompt J/ψ, to check for jet quenching effects caused by the QGP that can alter our interpretation of J/ψ results in heavy-ion collisions.
The results of both analyses are reported in Chapter 4. A discussion follows in the next chapter to discuss the physics interpretation of the results.

Chapter 2

Colossal machines to find minuscule particles

Particle physics takes the simplest possible approach to study the tiniest and most fundamental pieces of our universe: smashing things together and seeing what happens. In this chapter, we will take a look at the enormous machines used to accelerate particles, collide them and detect what comes out in the blast.

2.1 The Large Hadron Collider

'Large' for its circumference of 27 km, 'Hadron' for the group of particles protons and ions belong to and 'Collider' for the beams traveling in opposite directions and colliding at four points around the machine. The Large Hadron Collider (LHC) is currently the largest and highest-energy particle accelerator in the world. It was constructed by the European Organization for Nuclear Research (CERN[1]) at 175 m underground beneath the border between France and Switzerland between 1998 and 2008.

2.1.1 Accelerator complex

In the LHC, a strong magnetic field, maintained by superconducting electromagnets, guides two beams of particles in opposite directions in separate beam pipes kept at ultrahigh vacuum. The electromagnets are built from coils of special electric cable that operates in a superconducting state, efficiently conducting electricity without resistance or loss of energy. The accelerator is connected to a distribution system of liquid helium that keeps the magnets at -271.3°C, a temperature colder than outer space.
The LHC is the last element of the CERN accelerator complex which consists of a chain of machines that accelerate protons and ions. A schematic diagram of the injection chain is shown in Fig. 2.1. Each machine accelerates the beam of particles to higher energies than the previous one until the beam reaches 99.999999% of the speed of light.

[1]Conseil Européen pour la Recherche Nucléaire

Protons are extracted from a gas of hydrogen atoms in a duoplasmatron [79], a metal cylinder surrounded by an electrical field to break down the hydrogen gas into its constituent protons and electrons. The protons are accelerated by the linear accelerator LINAC2 using radiofrequency (RF) cavities. They are then sent to the Proton Synchrotron Booster (PSB) where the protons are grouped into bunches and accelerated. In the Proton Synchrotron (PS) the protons are accelerated and split into 72 bunches separated in time by 25 ns before they are injected in the Super Proton Synchrotron (SPS).
In the ion case, with each step, the particle loses more electrons. For Pb ions, the 29 outermost, weakly bound, electrons are removed electrically by evaporating Pb atoms before being accelerated with LINAC3 and sent through a thin (1 μm) carbon target to strip 25 more electrons. In the Low Energy Ion Ring (LEIR), the ions are then accumulated, cooled, and accelerated [80]. The beam is bunched and accelerated before it is extracted to the PS where a bunch-splitting occurs. The resulting bunch pair is then fully stripped in the transfer line to the SPS with a 0.8 mm thick aluminum foil.
For both proton and ion beams, the SPS accelerates the batches and then alternately injects them in the two LHC beam pipes, in opposite directions. Alongside accelerating the beams in the LHC, the size and trajectory are controlled. Dipole magnets are used to bend the trajectory of particles, and quadrupole magnets focus the beam. The beams cross in four interaction points that host the four largest CERN experiments.

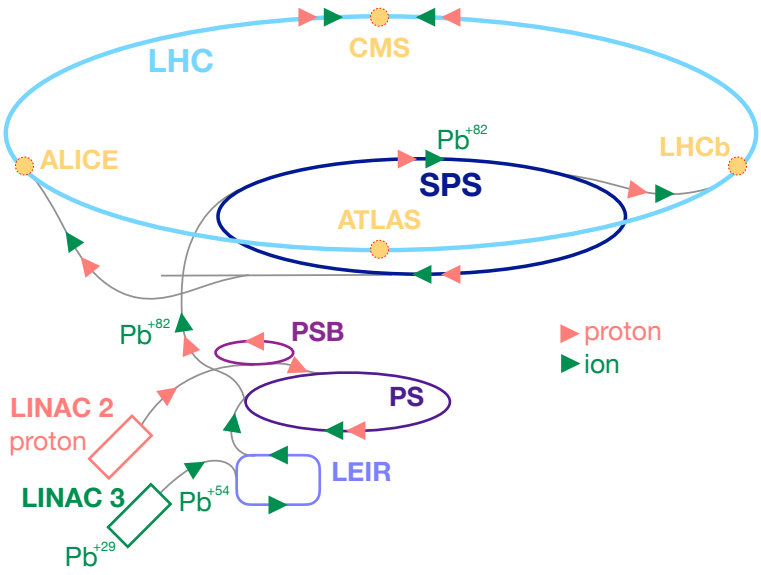

Figure 2.1: Schematic diagram of the LHC injection chain for protons and Pb ions.

2.1.2 CERN Experiments

Around the LHC ring, many experiments are installed for different purposes:

- A Large Ion Collider Experiment (ALICE) [81]: Since the main interest of the ALICE collaboration is the study of the QGP, the detector is specifically optimized to study heavy-ion reactions [82]. ALICE is made of 18 subdetectors that can be grouped in three main ensembles: the global event detectors that characterize the geometry of the collision, the central barrel at mid-rapidity optimized for the reconstruction of hadrons, electrons and photons, and the muon spectrometer to reconstruct muons at forward rapidity.

- A Toroidal LHC ApparatuS (ATLAS) [83]: The largest detector of the LHC. It is a multi-purpose detector, originally built to detect the Higgs boson and other massive particles in high luminosity pp collisions. It also participates in the heavy-ion data taking and contributes to the study of the QGP. ATLAS has the shape of a cylinder containing a toroidal magnetic system, an inner tracker, an electromagnetic and hadronic calorimeter, and a muon spectrometer.

- Compact Muon Solenoid (CMS) [84]: Similar to ATLAS, CMS is a multi-purpose detector. Since the results of this thesis use data taken by CMS, Section 2.2 is dedicated to discussing the detector and its components in detail.

- LHC beauty (LHCb) [85]: The main goal of the LHCb collaboration is investigating the slight differences between matter and antimatter by studying the b quark. The detector is a single-arm forward spectrometer designed to precisely measure the decays of B hadrons. In addition to the pp and heavy-ion runs, LHCb can operate in fixed-target mode by injecting nuclear gas (He, Ne, Ar) into the LHC beam pipe at the interaction point.

- LHC forward (LHCf) [86]: Made up of two detectors that sit along the LHC beamline around the ATLAS collision point. It uses the particles generated in the forward region of collisions to study cosmic rays.

- TOTal cross-section, Elastic scattering and diffraction dissociation Measurement at the LHC (TOTEM) [87]: With its subdetectors spread across almost half a kilometer around the CMS interaction point, it is CERN's 'longest' experiment. TOTEM's physics program is dedicated to the precise measurement of the proton-proton interaction cross-section, as well as to study the proton structure.

- MOnopole and Exotics Detector at the LHC (MOEDAL) [88]: The main goal of this experiment is to search directly for the magnetic monopole, a hypothetical particle with a magnetic charge. Deployed around the same intersection region as the LHCb detector, the detector acts as a giant camera waiting to photograph the telltale signs of new physics that could be formed in LHC collisions.

2.1.3 Luminosity

When studying rare events with a small production cross-section σ_p, the number of useful interactions is important. The instantaneous luminosity $\mathcal{L}$ is the proportionality factor between the number of produced events per unit of time, dR/dt, and the production cross-section and is measured in $\text{cm}^{-2}\text{s}^{-1}$:

$$\frac{dR}{dt} = \mathcal{L}.\sigma_p \tag{2.1}$$

The luminosity is one of the main characteristics of the LHC. It measures the ability of the particle accelerator to produce a required number of interactions.
In the case of circular accelerators the luminosity can be expressed as:

$$\mathcal{L} = \frac{k_b N_{b,1} N_{b,2} f_{\text{rev}} \gamma}{4\pi\epsilon_n \beta^*} F \tag{2.2}$$

In the numerator, k_b is the number of bunches collided, $N_{b,1}$ and $N_{b,2}$ are the number of particles per bunch in the two beams, f_{rev} is the revolution frequency which is 11245 Hz in the LHC, and γ is the Lorentz gamma factor. While in the denominator, ϵ_n is the normalized transverse beam emittance and β^* is the amplitude function at the interaction point, related to the width of the beams. F is the geometric luminosity reduction factor due to the crossing angle at the interaction point.
The integrated luminosity is derived by integrating the instantaneous luminosity over a given period of time. Fig. 2.2 shows the cumulative luminosity versus day delivered to CMS during stable beams for pp collisions at nominal center-of-mass energy. It is shown for data-taking in 2010 (green), 2011 (red), 2012 (blue), 2015 (purple), 2016 (orange), 2017 (light blue), and 2018 (navy blue).

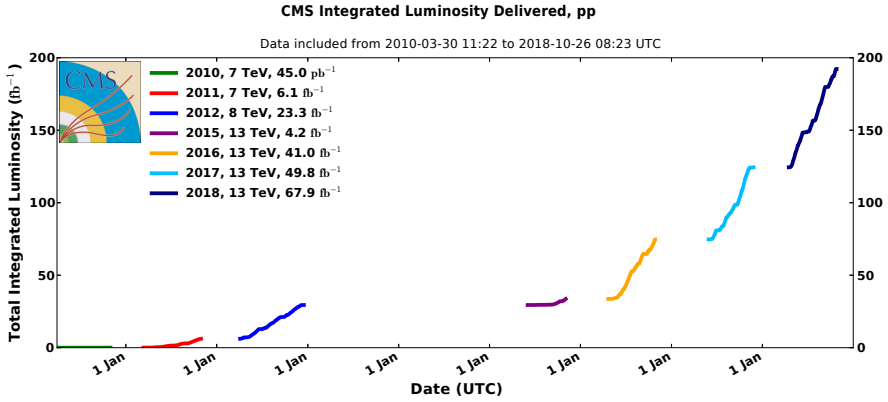

Figure 2.2: CMS delivered integrated luminosity versus time for pp data in 2010-2012 and 2015-2018.

2.2 The Compact Muon Solenoid

21 m long, 15 m in diameter, and 14,000 tonnes in weight, the CMS detector is the second-largest and heaviest detector at the LHC. The CMS detector is shaped like a cylindrical onion with several concentric layers of components. This design was chosen carefully based on the physics program of the collaboration. To investigate a wide range of physics, The subsystems of CMS were designed to meet many requirements [89] over a wide range of momenta and geometric coverage:

- Good muon identification and momentum resolution, good dimuon mass resolution, and the ability to determine the charge of the muons, requiring a very good and redundant muon system.
- Good charged particle momentum resolution and reconstruction efficiency and the capability to find any vertices (primary collision and particle decay vertices), requiring high-quality central tracking as close as possible to the collision point.
- Good electromagnetic energy resolution and good diphoton and dielectron mass resolution, requiring the best possible electromagnetic calorimeter.
- Good $E_{\mathrm{T}}^{\mathrm{miss}}$ and dijet mass resolution, requiring good hadron calorimeters with fine lateral segmentation.

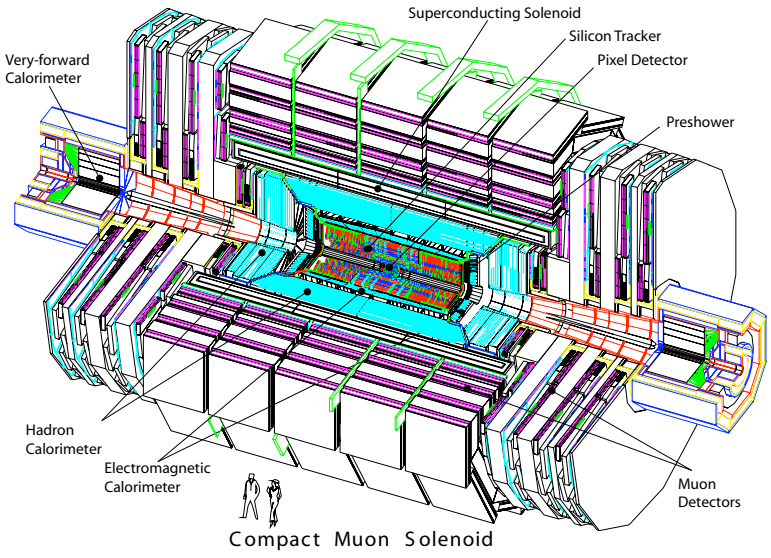

Figure 2.3: An exploded view of the CMS detector showing its different layers with two fancy people for comparison [89].

Fig. 2.3 shows the different layers of CMS. At the heart of CMS sits the most powerful superconducting solenoid ever made. The magnet coil is large enough to accommodate the inner tracker, made of a pixel detector and a silicon tracker, and the calorimetry, made of an electromagnetic and a hadronic calorimeter. The muon systems are situated around the magnet covered by its return field. Each subsystem serves a specific task to identify (nearly) all the stable particles produced in the collision and measure their momenta and energies. Information from all subdetectors is then pieced together like puzzle pieces to recreate an "image" of the collision. Details on the coordinate system used by CMS and the different components of the detector will be discussed in the following sections.

2.2.1 CMS coordinate system

The coordinate system of the CMS detector is centered at the interaction point. The x-axis is pointed radially towards the center of the LHC, the y-axis points upward perpendicular to the LHC plane and the z-axis is parallel to the beam pipe with its positive direction defined along the counter-clockwise beam direction.

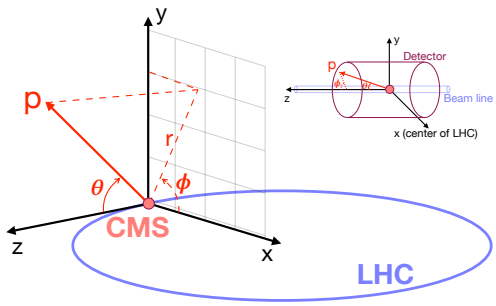

Figure 2.4: Schematic diagrams of the coordinate system used in the CMS experiment with the detector and the LHC ring as references.

The (x,y,z) axes are shown in Fig. 2.4 as well as the spherical coordinates used to measure the trajectory of particles in CMS, (r, θ, ϕ). The polar angle θ is defined as the angle between the trajectory of the particle to the z-axis while the azimuthal angle ϕ is measured from the x-axis in the x-y plane, called the transverse plane. The radial coordinate r is also measured in the transverse plane as $r = x^2 + y^2$.
The transverse momentum p_T is defined as:

$$p_T = \sqrt{p_x^2 + p_y^2} \tag{2.3}$$

This quantity is of particular importance and is heavily used in experimental particle physics.

Another quantity usually used in accelerator physics is the rapidity, noted as y and defined as:

$$y = \frac{1}{2} \ln \left(\frac{E + p_z}{E - p_z} \right) \tag{2.4}$$

The rapidity is 0 for particles in the transverse plane, referred to as mid-rapidity, and infinity for particles in the beam direction referred to as forward. Since this quantity needs both the particle energy and the momentum along z it can be hard to measure precisely. Instead, the pseudorapidity η is used, which is defined as:

$$\eta = \frac{1}{2} \ln \left(\frac{|p| + p_z}{|p| - p_z} \right) = -\ln \left(\tan \frac{\theta}{2} \right) \tag{2.5}$$

For relativistic particles $y \approx \eta$ and they match for massless particles. The three quantities, p_T, y, and η, are Lorentz invariant under longitudinal boosts.

2.2.2 Superconducting magnet

One of the main distinguishing features of CMS is a superconducting solenoid, generating a magnetic field[2] of 3.8 T and giving the detector its last name. The superconducting coil, the vacuum tank, and the magnet yoke are the three components of the CMS magnet system shown on the left of Fig. 2.5.

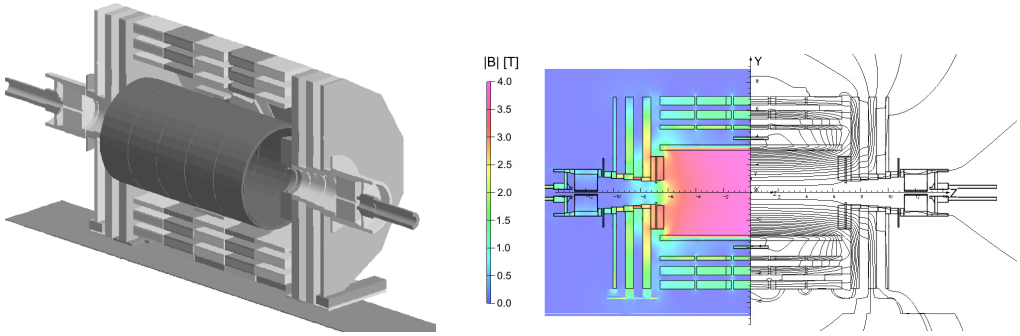

Figure 2.5: On the left: 3-D model of the CMS magnetic system with half of the return yoke [90]. On the right: Value of |B| (colored) and field lines (black and white) predicted on a longitudinal section of the CMS detector [91].

The solenoid is made of coils of wire that produce a uniform magnetic field when electricity flows through them. The coil is thermally insulated within a vacuum volume and operates in superconducting mode letting the electric currents flow without resistance. The solenoid consists of four layers each made of 16x2 of, Rutherford-type, Niobium-Titanium superconducting strands, extruded with pure aluminum and mechanically reinforced with an aluminum alloy [84].

[2] 100000 times stronger than the magnetic field of the Earth

The yoke is a 12-sided iron structure that surrounds the magnet coils and is responsible for the return of the magnetic flux. It also provides most of the experiment's structural support.
A map of the magnetic field |B| is shown on the right of Fig. 2.5. The colors show the value of |B| with a central magnetic flux density of 3.8 T close to the beam pipe. The directions of the field lines are also shown in black and white.
The CMS magnet provides the needed energy to bend the paths of particles emerging from high-energy collisions in the LHC. This helps to identify the charge of the particle since positively and negatively charged particles bend in opposite directions. It is also essential for the measurement of particle momenta, the more momentum a particle has the less its path is curved by the magnetic field. The trajectory of a charged particle is shown in Fig. 2.6 in the transverse and longitudinal planes of CMS. The change in the magnetic field inside the magnetic coil and in the yoke causes the trajectory to change its direction in the x-y plane. The trajectory is not bent in the z-direction.

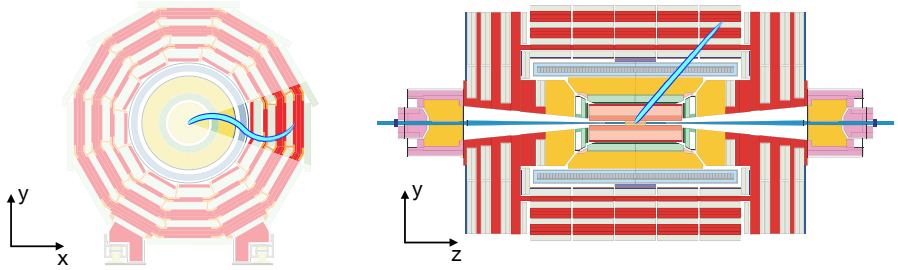

Figure 2.6: Longitudinal (left) and transverse (right) view of the CMS detector with a trajectory of a charged particle shown in blue.

2.2.3 Tracking system

Merely bending particles is not enough. CMS uses a series of subdetectors to identify the paths taken by these particles. The closest to the collision point is the tracking system, made of a pixel detector and a silicon strip tracker and covering the pseudorapidity range $|\eta| < 2.5$. The area close to the interaction vertex is where the particle flux emerging from the collisions is the highest. The tracker needs to have a high granularity to record particle paths accurately yet be thin and lightweight to disturb the particle as little as possible. The active material of the tracker is made of silicon. When a charged particle passes through the tracker, it interacts electromagnetically with the silicon atoms creating electron-hole pairs. The free electrons are then drifted by an electric current creating an electric signal that is amplified and detected registering a "hit". The track of the particle is reconstructed by joining the hits produced by the particle in the different layers.
The cross-section of the tracker is shown in Fig. 2.7. The pixel detector is made of four pixel layers in the barrel, starting at only 2.9 cm from the collisions, and three forward

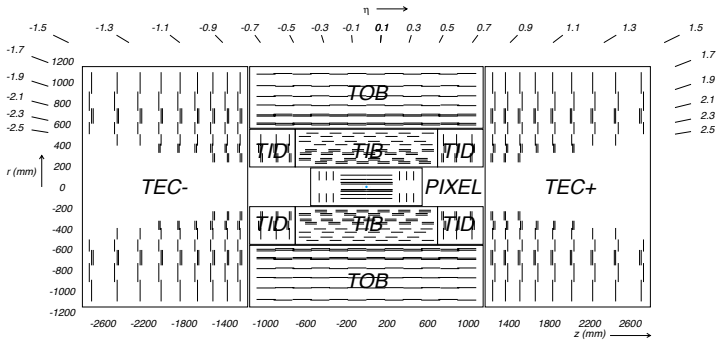

Figure 2.7: Schematic cross-section through the CMS tracker [84]. Each line represents a detector module. Double lines indicate back-to-back modules that deliver stereo hits.

pixel disks on each side of the interaction point [92]. The detection modules in the forward detector are arranged in a turbine-like structure to optimize the charge sharing between pixels and is therefore beneficial for the hit resolution. In the barrel region, the silicon-strip tracker surrounds the pixel detector with the Tracker Inner Barrel (TIB) and the Tracker Outer Barrel (TOB). The TIB is made of four cylinders with the modules placed overlapping like roof tiles to allow better area coverage. The closest two layers are made with "stereo"[3] modules that deliver two-dimensional hit positions.
The endcaps are divided into the TEC (Tracker End Cap) and TID (Tracker Inner Disks). On each side, the TID is made of three rings of modules, and the TEC is made of nine, centered on the beamline. In the TID, the first two rings have "stereo" modules while in the TEC the innermost two rings and the fifth ring have them.
During full luminosity collisions the occupancy of the pixel layers per event is of the order of 0.1%, and 1–2% in the strip layers. Even in PbPb collisions, the occupancy is at the level of 1% in the pixel detectors and less than 30% in the silicon strip layers.

2.2.4 Electromagnetic calorimeter

The Electromagnetic CALorimeter (ECAL) of CMS is designed to fully absorb and measure the energy of electrons and photons. It is made of lead-tungstate ($PbWO_4$) crystals chosen for the material's small Molière radius[4], caused by its short radiation length and high density, resulting in a fine granularity and a compact calorimeter. The metallic-yet-transparent crystals, shown in Fig. 2.8 on the right, are aligned in the barrel region and the endcaps as shown on the left side of the same figure. The barrel contains 61,200 crystals grouped in 36 supermodules while each of the endcaps contains 7324 crystals assembled in units of 5x5 crystals [94]. The ECAL covers the pseudorapidity range $|\eta| < 3$.

[3] made of two single-sided detectors mounted back to back with an inclined strip against each other.

[4] a characteristic constant of a material giving the scale of the transverse dimension of the fully contained electromagnetic showers initiated by an incident high energy electron or photon [93].

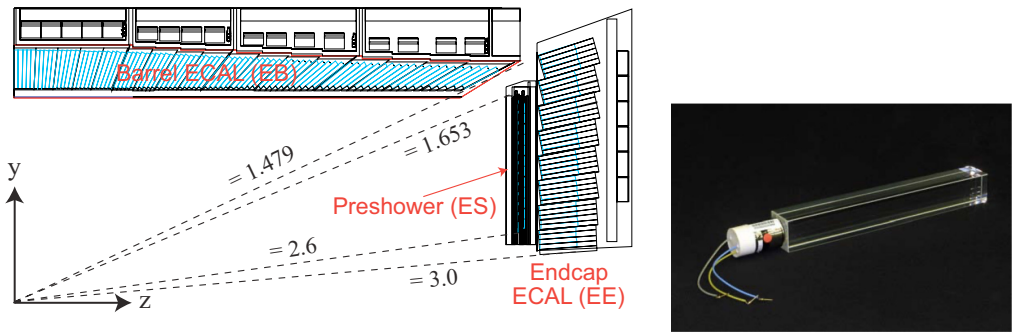

Figure 2.8: Transverse section through the ECAL, showing the geometrical configuration on the left [89] and an endcap crystal on the right [84].

When a high-energy photon or electron passes through the ECAL, it deposits energy in the crystals through bremsstrahlung and pair-production, generating a cascade of electromagnetic particles. That results in scintillation light being emitted in the crystals and then measured by photodetectors. The amount of produced light is a linear function of the particle energy. The photodetectors in the barrel are Avalanche PhotoDiodes (APD) mounted in pairs on the back of each crystal, while Vacuum PhotoTriodes (VPT) are used in the endcaps, attached to the back of each crystal.
The ECAL also contains preshower detectors installed in front of the endcaps consisting of two layers of lead each followed by a layer of silicon strip detectors. The principal aim of the preshower is to identify neutral pions in the endcaps. It also helps the identification of electrons against minimum ionizing particles and improves the position determination of electrons and photons.
Since the transparency of the crystals to scintillation light is affected by radiation, a monitoring system is installed to track the radiation-induced transparency variations using laser pulses. The crystals are also kept at a stable temperature of 18°C using a water flow cooling system because the response of the crystals and the signal amplification depend on the operating temperature.

2.2.5 Hadron calorimeter

The Hadron CALorimeter (HCAL) is the detector responsible for hadron energy measurements. The HCAL and ECAL form a complete calorimetry system for the measurement of jets and missing transverse energy.
The HCAL is a hermetic sampling calorimeter; which means it's made of scintillating active material and layers of absorber material. When a hadron hits an absorber plate, it interacts with the material creating a shower of secondary particles that passes through the scintillating layers emitting light. The light signal, measured by photodetectors, is proportional to the energy of the incident hadron.
The HCAL is divided into four sections: barrel HCAL (HB), endcap HCAL (HE), outer

HCAL, and forward HCAL (HF). Their locations with respect to the other detectors are shown in Fig. 2.9.

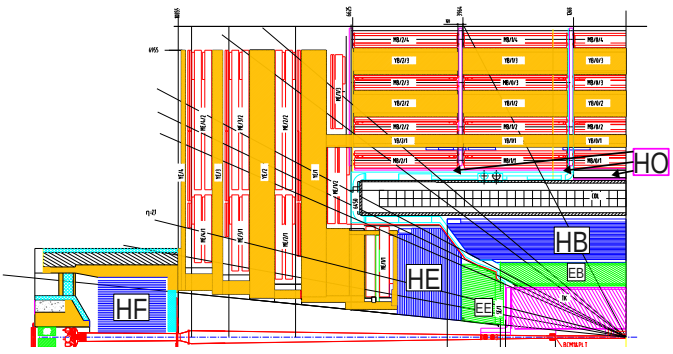

Figure 2.9: Longitudinal view of one quadrant the CMS detector showing the locations of the hadron barrel (HB), endcap (HE), outer (HO) and forward (HF) calorimeters [95].

The HB and HE use brass as the absorber and plastic scintillator as the active material. The light emitted by the plastic scintillator is measured by Hybrid PhotoDiode (HPD) transducers.
The HO acts as a *'tail catcher'* that complements the HB since the location of the HB between the outer extent of the ECAL and the inner extent of the magnet coil constrains the total amount of material that can be put in to absorb the hadronic shower. It is made of tiles of Bicron BC408 scintillator plates and uses Silicon PhotoMultipliers (SiPM) to detect photons. It also utilizes the solenoid coil as an additional absorber.
Since the HF is located at very forward rapidity, it experiences unprecedented particle fluxes and extremely high charged hadron rates. It is designed to survive this hostile environment as a large steel absorber embedded with quartz fibers. The charged shower particles, created from the interaction between the hadron and the absorber steel, generate Cherenkov light if their energy is above the Cherenkov threshold. The quartz fibers, which run longitudinally through the absorber, collect Cherenkov light primarily from the electromagnetic component of showers.

2.2.6 Muon system

The Muon system is a group of "chambers" that uses gas ionization to detect muons. It is one of the defining features of CMS as the name "Compact Muon Solenoid" suggests. The muon detectors are placed at the very edge of the experiment since muons can penetrate the dense material of the calorimeters and solenoid magnet without interacting. Three types of chambers are used: Drift Tubes (DT), Cathode Strip Chambers (CSC), and Resistive Plate Chambers (RPC). They are placed inside the magnet return yoke as shown in Fig. 2.10: DTs in the barrel, CSCs in the endcaps, and RPCs in both.
The DTs are arranged in four concentric cylindrical chambers, labeled MB[1-4] in Fig. 2.10,

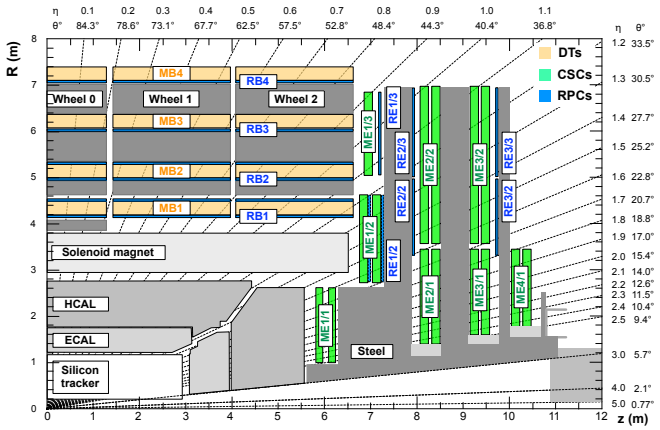

Figure 2.10: Longitudinal view of one quadrant of the CMS detector showing the locations of the drift tubes (orange), cathode strip chambers (green) and resistive plate chambers (blue) [96].

around the beamline. A schematic view of one chamber is shown in Fig. 2.11 on the left side. The station consists of eight layers of tubes measuring the position in the r-ϕ plane on the top and the bottom and four layers in the r-z plane. The different layering of the tubes in different directions allows the measurement of two coordinates: along the direction parallel to the beam and perpendicular to it.

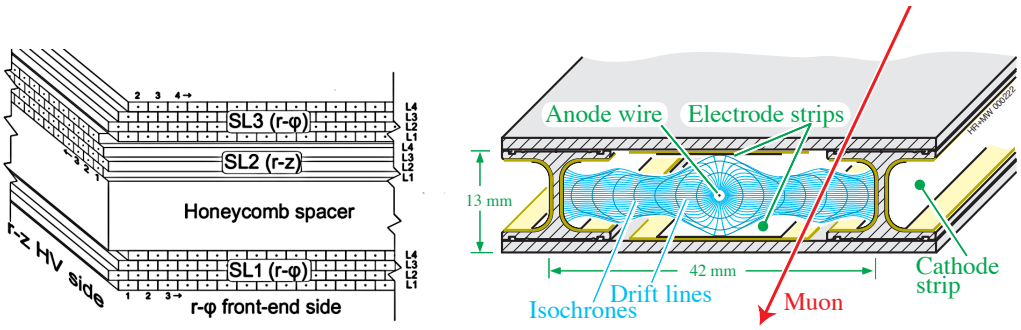

Figure 2.11: Left: Schematic view of a DT chamber. Right: Section of a drift tube cell [96]. The drift lines are the lines followed by the electrons as they drift to the anode wire while the isochrons connecting points relating to the same drift time.

A single DT is shown on the right side of Fig. 2.11. Each 4-cm-wide cell contains two electrode strips at the top and bottom of the cell, two cathode plates on the sidewalls, and a gold-plated stainless-steel anode wire at the center. The cells are filled with a gas mixture of 85% Ar + 15% CO_2.

Since muons are charged particles, when one passes through a DT cell it ionizes the gas releasing electrons. The electrons *drift* to the anode wire and are then collected as an electrical signal. The muon's position is measured by registering where along the wire electrons hit, as well as by calculating the muon's original distance away from the wire.
In the endcap region, the muon rate is high and the magnetic field is not uniform. The CSCs are installed there since they have a fast response time, they can be finely segmented, and they can tolerate the non-uniformity of the magnetic field [96]. Each endcap uses 270 CSCs. One chamber consists of seven cooper cathode strips, crossed with six anode wires, creating six gaps filled with a gas mixture of 40% Ar, 50% CO_2, and 10% CF_4. The cathode strips run radially outward providing the coordinate in the r-ϕ while the anode wires are placed azimuthally and measure the pseudorapidity of the muons.

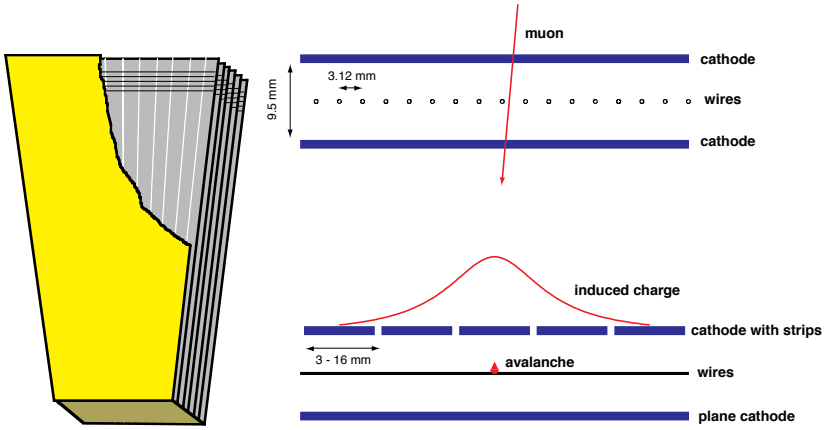

Figure 2.12: Left: Schematic layout of a CSC showing the six layers and the orientations of the wires, only a few of which are shown. Right: Cross-sectional views of the gas gap in a CSC showing the anode wires and cathode planes and the charge distribution caused by the gas ionization avalanche [96].

A CSC is shown in Fig. 2.12 on the left side. The cathode strips and the few wires are shown. When a muon passes a chamber the gas is ionized emitting electrons that create a subsequent electron avalanche. The avalanche produces a fast, coarse resolution, charge signal on the anode wire and an induced, more precise, charge signal on a group of cathode strips, as shown on the right side of Fig. 2.12.
The barrel and endcaps are complemented with an RPC system, consisting of four stations in the barrel and 3 stations in each endcap, as a dedicated triggering system with excellent time resolution. An RPC, shown in Fig. 2.13, is a gaseous parallel-plate double-gap module with each gap consisting of two bakelite plates with the outer surface coated with a thin conductive graphite layer. One of the plates is a positively charged anode and the other is a negatively charged cathode. The gas is a mixture of 95.2% Freon ($C_2H_2F_4$, known as R134a), 4.5% isobutane (i-C_4H_{10}) and 0.3% sulfur hexafluoride (SF_6), with water vapor added at the end to obtain a relative humidity of 40%–50%

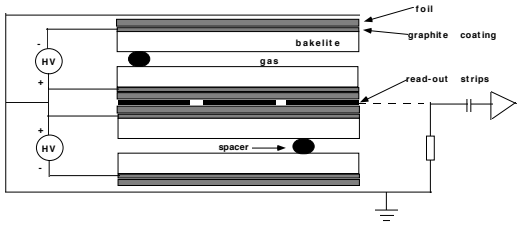

Figure 2.13: Cross-section view of a double gap RPC [97].

When a muon passes through the RPC it ionizes the gas in both gaps emitting electrons that generate more electrons creating an avalanche that crosses the electrodes without interacting and is then picked by the readout strips installed between the two gaps.

2.2.7 Trigger systems

For the nominal LHC design luminosity of 10^{34} cm^{-2}s^{-1} for pp collisions, the beams cross every 25 ns at a crossing frequency of 40 MHz with approximately 20 events occurring at every crossing. Only a small fraction of events are of interest to the CMS physics program, and only a small fraction can be stored for later offline analysis. Therefore a trigger system is needed to select the interesting events for offline storage [98]. The CMS trigger system reduces the event rate in two steps: the Level-1 (L1) Trigger and the High-Level Trigger (HLT).

Level-1 trigger

The L1 trigger is an extremely fast, entirely hardware-based, system that uses information from the calorimeters and the muon system to decide if an event is kept or rejected, within 4 μs of the collision. The L1 trigger is divided into calorimeter and muon triggers that run in parallel, checking for candidate objects in the event like energy clusters consistent with an electron or ionization deposits consistent with a muon. The L1 trigger output rate is restricted to 100 kHz, so the trigger thresholds are adjusted during the data taking based on the value of the LHC instantaneous luminosity.
The L1 conditions are organized in a menu made of different algorithms, programmed by the users, and hard-coded in the firmware of a Field-Programmable Gate Array (FPGA). The Trigger Primitive (TP) is the unit of the input data from each subdetector. For the calorimeter, a TP is derived from Trigger Towers (TT), each corresponding to a module of 5x5 crystals in the ECAL, while for the muon system a TP corresponds to a segment in the DT, CSC, and RPC systems. The TPs are processed in many steps then combined in the Global Trigger (GT) that makes the final decision if the event is kept or not.
A schematic view of the L1 trigger system is depicted in Fig. 2.14. The L1 calorimeter trigger [101] is divided into two separate processing layers with data split into bunch-crossing intervals instead of detector regions. The first layer collects data from the calorime-

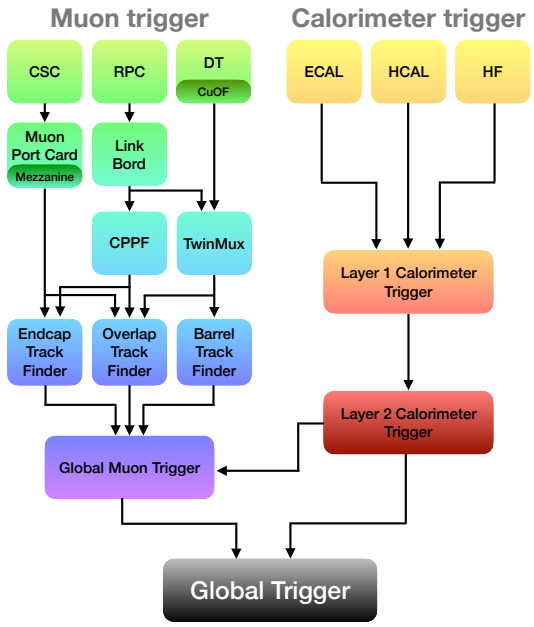

Figure 2.14: Block diagrams of the L1 trigger system, based on the diagrams in Ref. [99, 100].

ter TTs and then distributes it to the FPGAs of the second layer, which uses the data to reconstruct object candidates: e/γ, jets, and taus. The global energy quantities are also measured.
The L1 muon trigger [102] follows a regional approach (endcap, overlap, and barrel), and receives information from the DTs, CSCs, and RPCs. Hits from the CSCs are sent to the endcap and overlap track finders (EMTF and OMTF) via a mezzanine on the muon port card. RPC hits are sent to the EMTF via the link board to the concentrator preprocessor and fan-out (CPPF) card and to the barrel track finder (BMTF) via a TwinMux concentrator card, which also provides DT hits to the BMTF and OMTF. The best muons from the regional track finders are selected in the global muon trigger and sent, together with information from the calorimeter about the muon isolation, to the global trigger.

High level trigger

The HLT trigger [103] reduces the 100 kHz input from the L1 trigger down to 1 kHz which is the limit of the data transfer rate required by the CERN main computing farm. The HLT hardware consists of an array of multi-core computers running Scientific Linux. The data processing of the HLT is structured around the concept of an HLT path, which is a set of algorithmic processing steps run in a predefined order. The event selection is performed in a similar way to that used in the offline processing and is done by three units: readout, builder, and filter units. When an event passes the L1 trigger, the readout

unit extracts all information from the CMS subdetectors. The builder then builds detector segments, hits, and clusters, using the raw data provided by the readout unit, to form complete events. Lastly, the filter unit performs the reconstruction of physics objects and selects events for data analysis. The conditions for each HLT path are defined by users like requiring a certain number of electrons in the event or the presence of muons with p_{T} larger than a given threshold.
The analyses for this thesis analyze data triggered with HLT triggers requiring the presence of muons. Some require the presence of two L1 muons without further reconstruction. Others require additional HLT reconstruction which is done in two levels: Level-2 (L2) and Level-3 (L3) reconstructions.

HLT L2 muon reconstruction The L2 muon reconstruction uses information for the muon detectors, starting by locally reconstructing hits in each muon chamber. The hits measured in the DT or CSC are then combined to form "track segments". Only segments that are close to an L1 candidate are kept. The Kalman Filter (KF) technique [104] is used to build the tracks by recursively fitting the segments with a fit constrained by the position of the interaction point to improve the p_{T} resolution. Duplicate tracks are then filtered.

HLT L3 muon reconstruction The L3 reconstruction uses both the muon system and the tracker. The use of tracks significantly improves the resolution of the muon candidates. A regional tracking is performed by only reconstructing tracker tracks close to the L2 muon candidates, using three different seeding algorithms:

- The seeds are defined by extrapolating the position and p_{T} of the L2 muon tracks to the outer surface of the inner tracker.
- The seeds are defined by the L2 track parameters extrapolated to the outer surface of the tracker and updated with information from the outermost layers of the silicon strip detector.
- The seeds are defined by pairs of hits on adjacent layers of the silicon-pixel subdetector found in a narrow $\eta - \phi$ region around each L2 muon track.

The three algorithms are run from faster to slower, which are only used of the faster algorithms fail. The tracks are reconstructed with a KF fit starting from the initial seeds. The reconstructed tracker and L2 muon tracks are propagated to a common surface and then matched by comparing their separation, directions, or χ^2. If an L2 track and a tracker track match are found, a final refit of all the tracker and muon system measurements is performed to form the L3 muon track.

Chapter 3

Measuring the fragmentation functions

3.1 The road map

Beams are colliding, detectors are catching flying particles, and information is being recorded. But we don't have physics results yet. A lot of work still needs to be done to reconstruct and analyze data. The first thing is to identify the systems and datasets depending on the physics studied. When the machine is running the triggers select the events of interest using objects reconstructed on the fly. The objects are also reconstructed offline using more information that takes more processing time than the online reconstruction. The analyzers then apply selection cuts on the events and objects depending on the specifics of each analysis. The analysis procedures are usually composed of many steps using different statistical tools. The obtained results are then documented and published. This road map is illustrated in Fig. 3.1.

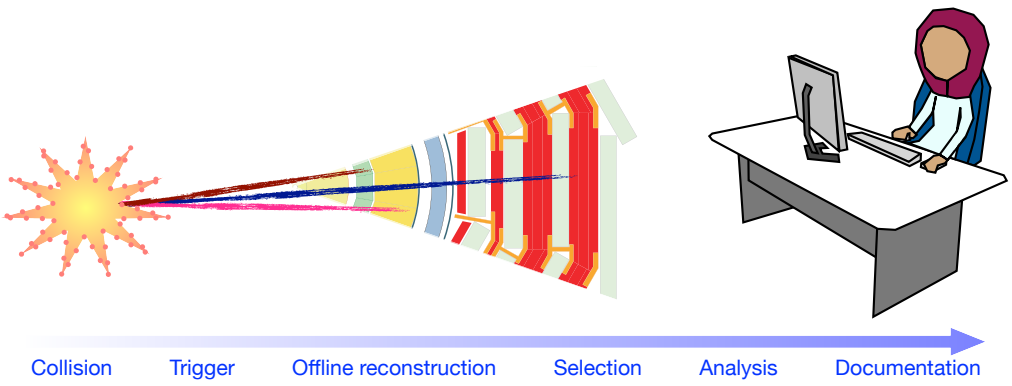

Figure 3.1: The different steps to get physics results.

The goal of this thesis is to study J/ψ in jets in two systems: pp and PbPb. The J/ψ meson can decay in many modes. The dimuon channel was chosen for this analysis for its clean signal using the CMS detector. Depending on the system and dataset a trigger is chosen that collects the events of interest for the analysis and deposits them in a data sample. An offline selection is then applied to the different components of the analysis: the event, the J/ψ/muons, and the jet. The analysis has two major segments: The J/ψ signal extraction and the jet reconstruction and p_{T} determination.
Following the plan explained in Sec. 1.3, two analyses were done: The first using the 2015 pp collisions and including both prompt and nonprompt J/ψ in jets results, and the second using 2017 pp and 2018 PbPb runs and only focusing on the prompt results. The procedure used for both analyses is essentially the same, therefore the following sections, going through the details of each step, will focus on the second analysis that includes PbPb. For the sake of going from global to specific details, the offline event selection will be discussed before the object reconstruction, right after discussing the trigger.

3.2 Data samples and trigger selection

J/ψ in jets are studied in pp and PbPb collisions using data recorded by the CMS detector at $\sqrt{s_{NN}} = 5.02$ TeV. The datasets are composed of events selected by HLT triggers. In the pp case, the trigger requires at least two L1 muon candidates, without any p_T requirement, whereas for PbPb, the trigger is a bit more complicated. It requires at least two L2 muon candidates out of which at least one is an L3 muon matching a track with 10 hits in the silicon tracker. The trigger also has an invariant mass filter requiring the dimuon mass to be within the range of 1 to 5 GeV. Fig. 3.2 shows the invariant mass spectra of dimuons reconstructed with three different HLT triggers. The coral pink peak corresponding to the J/ψ meson is reconstructed with the HLT trigger used in this thesis for PbPb collisions.

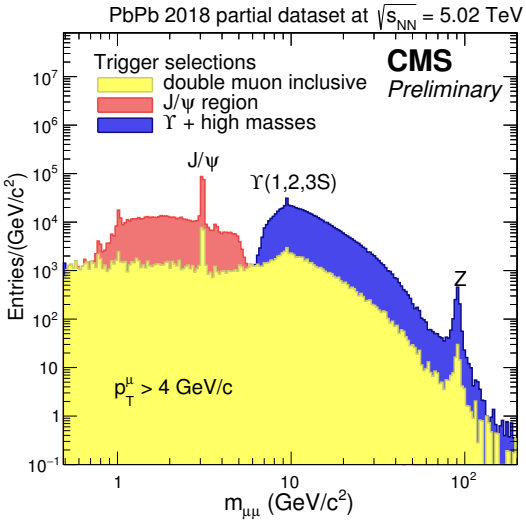

Figure 3.2: Dimuon invariant mass spectra reconstructed with HLT triggers for a partial dataset of the 2018 PbPb run. The different colors indicate different HLT triggers.

The CMS Collaboration monitors the data quality during and after the data-taking period running various checks and filtering out events for which the subdetectors were not operating in proper conditions. The integrated luminosities corresponding to the data samples used in this thesis are given in Table 3.1.

Year	System	Luminosity
2015	pp	27.39 pb^{-1}
2017	pp	311 pb^{-1}
2018	PbPb	1.64 nb^{-1}

Table 3.1: The integrated luminosity of the datasets used in this analysis.

Monte Carlo simulations

In addition to the data samples, simulated Monte Carlo (MC) samples are also used in different steps of the analysis.
For a given process, the simulation is done in three steps. The first is to generate the primary particle and its decay to a given final state using an event generator, PYTHIA 8.212 [105] in this case. The second is to pass the decay products through a transport code that simulates the passage of particles through the detector, like GEANT4 [106] that was used in this analysis. It characterizes the geometry of the detector and records the hits the particles produce by interacting with the active detection elements. The third step is to reconstruct the final state particles using the information from the created hits.
For PbPb events, simulated signal events are embedded in the underlying environment simulated by a heavy ion generator like HYDJET [107], and then reconstructed like normal events. This step is needed because the detector response is affected by its occupancy making the detector less efficient for higher multiplicity events as is the case in central collisions.
Prompt and nonprompt J/ψ samples were produced for both pp and PbPb. The prompt samples were generated following the NRQCD models for charmonium production, while the nonprompt samples were produced by the decay of the b hadrons (B^+,B^0 and B_s^0 mesons, as well as their charge conjugates and excited states) with the EVTGEN package [108] interfaced to PYTHIA.
A $\hat{p}_T$ bias was used to sample events more evenly out to large p_T, with $\hat{p}_T$ being the p_T of the simulated hard scattering process. The bias is then corrected with a weight factor. Since the PbPb sample was produced using minimum bias HYDJET events, equally distributed in centrality, the centrality distributions of the J/ψ samples are flat. The J/ψ production in data is biased towards more central collisions. In order to match the simulation distributions to data, each event is weighted by the N_{coll} corresponding to the centrality of the collision, given by the Glauber model calculations explained in Section 1.1.3.

3.3 Event selection and centrality determination

There are several background sources to the inelastic hadronic collisions such as beam-gas collisions, beam scraping events, and electromagnetic interactions (ultra-peripheral collisions). To remove the background, an offline selection is applied on each event.
For pp collisions, the event selection consists of a primary vertex filter, that requires a primary vertex reconstructed from at least two tracks, and a beam-scraping filter that requires at least 25% of tracks in the event to be high-quality tracks.
In the case of PbPb collisions, the primary vertex filter is also used, in addition to an HF coincidence filter that requires at least two towers on each side of the interaction point in the HF with an energy deposit of at least 4 GeV per tower, and a cluster compatibility filter requiring that the shape of the silicon pixel clusters are compatible with tracks originating from the primary vertex.

Centrality determination

In PbPb collisions, the events are divided into centrality classes expressed in percentage of the total hadronic inelastic cross-section.
The centrality relates directly to the occupancy of the detector, hence is determined using event-level variables: the sum of HF transverse energy, the total number of reconstructed tracks, the number of pixel clusters, etc.
For the 2018 PbPb run, the sum of transverse energy in the HF calorimeters is chosen as the centrality variable. The events are divided into 200 centrality bins corresponding to centrality classes of 0.5% of the total inelastic hadronic cross-section. The bin boundaries are a simple list of HF E_{T} that is determined by sorting the sum of HF E_{T} of events that pass default trigger and event selection and then divide them into 200 parts. The events are taken from a minimum bias sample i.e. only requiring a bunch crossing and a coincidence between signals from the -z and +z sides of the HF calorimeters.
The distribution of the sum of HF E_{T} for a large sample of minimum bias collisions is shown in Fig. 3.3 separated in centrality classes.
A data+MC calibration was developed to take into account the event selection efficiency + contamination that affects peripheral events. Below a certain threshold, the HF E_{T} distribution was taken from HYDJET events. On the left of Fig. 3.4, the data and MC HF E_{T} distributions used for the calibration are shown. The event selection is only applied to data. In addition to the y-normalization, the HYDJET HF E_{T} distribution is scaled along the x-axis by what is called "MC X scale" on the plot. Different scales were tested by fitting the HYDJET distribution and computing the χ^2 of the fit to the data distribution in the "plateau" region, i.e. excluding the most central and most peripheral events. The X scale = 0.86, had the best χ^2 and was used for the calibration. The HF E_{T} threshold was also determined in the same way with the best χ^2. The data/MC ratio is interpreted as efficiency + contamination and found to be $(97 \pm 1.5)\%$. The uncertainty is computed by changing the data/MC threshold.
Fig. 3.4 also shows the centrality bin distributions of 2018 data using three HF E_{T} thresholds. 100 GeV is taken as the nominal value and the other two are used as systematic vari-

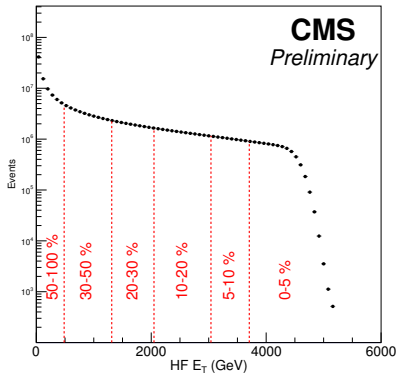

Figure 3.3: Distribution of the sum of transverse energy deposited in the HF calorimeters for minimum bias events. The centrality classes are shown in red.

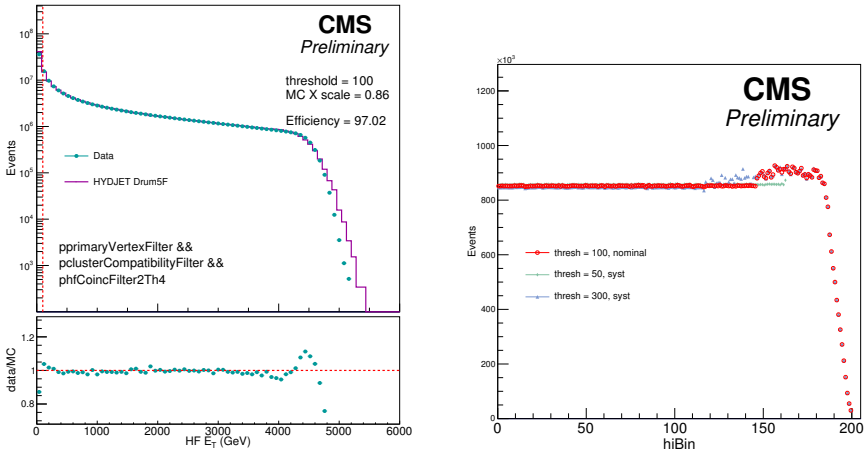

Figure 3.4: Left: Distribution of the sum of HF E_T in data and MC. Right: Distribution of the centrality bin for a minimum bias sample of the 2018 PbPb data.

ations. The excess of events in the peripheral region indicates remaining electromagnetic contamination after event selection. The systematic variation for centrality calibration is negligible in the case of J/ψ events so it is not taken into account in this analysis.
In the case of MC simulations, the centrality bin boundaries are determined from the whole minimum bias sample (without any selection) and simply divided into 200 equal bins.

3.4 Object reconstruction

Particles passing through CMS leave hits, segments, and clusters in the subdetectors depending on the type of particle. As shown in Fig. 3.5:

- A muon, shown in blue, creates hits in the tracker and the muon chambers.
- An electron, shown in red, traverses the silicon tracker layers radiating bremsstrahlung photons until it reaches the electromagnetic calorimeter producing a "supercluster".
- A photon, shown with a dashed navy line, passes through the tracker without interaction and showers in the electromagnetic calorimeter.
- A charged hadron, shown with a solid green line, creates hits in the tracker and showers in the hadron calorimeter.
- A neutral hadron, shown with a dashed green line, passes through the tracker without interaction and showers in the hadron calorimeter.

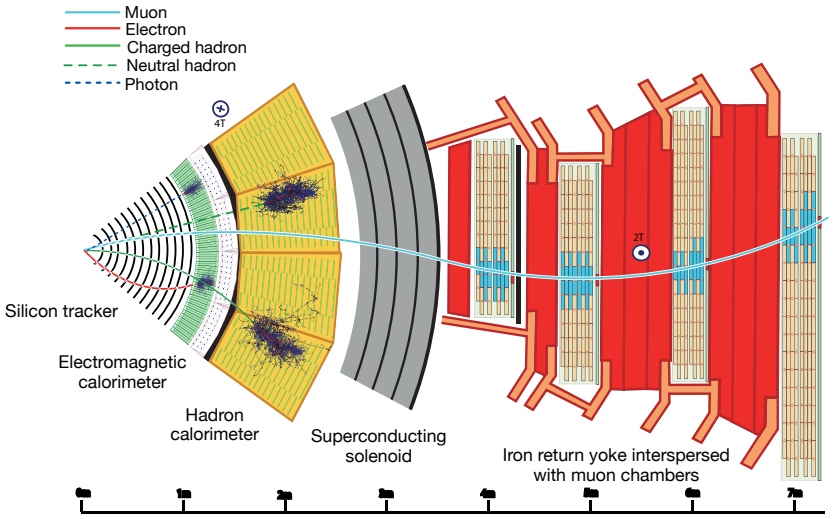

Figure 3.5: Transverse slice through the CMS detector showing how particles interact with the subdetectors.

The object reconstruction is to collect the footprints left in each of the CMS subdetectors to form the physics objects that left them. The experimental signatures of quarks and gluons, i.e. jets, are also reconstructed.
The following sections will discuss, in detail, the reconstruction of muons and jets, the main objects used in this thesis.

3.4.1 Muon reconstruction

In CMS muon reconstruction is done using information from the silicon tracker and the muon chambers. The muons reconstructed in the muon system are called standalone muons. Those reconstructed in the inner tracker and matched to a hit in the muon system are called tracker muons. Global muons are the muons that are reconstructed by matching a track in the inner tracker with a standalone-muon track in the muon chambers. Fig. 3.6 shows the different types of muons with respect to the CMS detector.

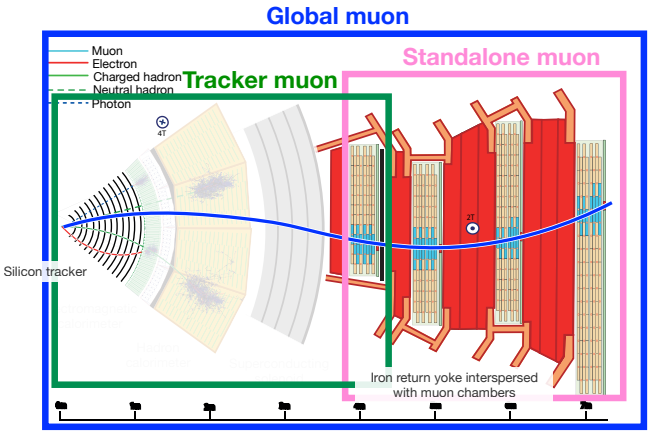

Figure 3.6: Transverse slice through the CMS detector highlighting the subdetectors that play a role in muon reconstruction. The boxes indicate different types of muons.

Standalone muons

The reconstruction of standalone muons starts with *locally* reconstructing hits in the muon system and combining them within each chamber [109]. The linear interpolation of the position of hits measured in the DT or CSC layers provides a "track segment". The Kalman Filter technique [104] is used to build the tracks by fitting the track segments starting from the innermost station and progressing towards the outer stations. In each step, the χ^2 between the track and the detector is computed, excluding hits with large χ^2 values from the KF fit. After the trajectory is built in the forward direction, backward pattern recognition is performed from the outermost to the innermost muon chambers. Finally, the trajectory is propagated to the interaction point.

Tracker muons

In the tracker, a sequence of tracking algorithms, each with slightly different logic, is used to reconstruct tracks from hits [110]. The hits that are associated with a track are removed from the input of the following step. For the track to become a tracker muon, the track is propagated to the muon system with loose matching and loose selection, $p_{\mathrm{T}} > 0.5$ GeV

and $p > 2.5$ GeV, to the innermost muon station. If at least one muon segment matches the extrapolated track along the transverse plane, the tracker track qualifies as a tracker-muon track.

Global muons

Global-muon tracks are built by matching standalone-muon tracks with tracker tracks. A region of interest is defined in the tracker using the standalone muon kinematics. It holds information about desired track position at the vertex and its kinematics. The tracker tracks are built from the hits in the inner tracker with an iterative KF combinatorial track finder. The tracker tracks are then compared with the standalone tracks. In the case of matching, the hits from both tracks are refitted to derive the ultimate global-muon candidate.
Due to the high efficiency of the tracker track and muon segment reconstruction, about 99% of the muons produced within the geometrical acceptance of the muon system are reconstructed either as a global muon or as a tracker muon, and very often as both [110].

3.4.2 Jet reconstruction and clustering algorithms

Quarks and gluons cannot be directly observed in nature due to color confinement. Instead, they hadronize to form collimated sprays of hadrons called jets. Jets are reconstructed using their signatures in the different subdetectors like tracks in the tracker or clusters in the calorimeters.
CMS uses three different methods to reconstruct jets: a calorimeter-based approach, the "Jet-Plus-Track" approach, which uses the calorimeter and the tracks, and the "Particle Flow" (PF) approach [111], which uses information from all subdetectors to individually reconstruct each particle in the event. PF is now used by most CMS analyses since it significantly improves the jet energy resolution compared to other approaches, especially at low p_{T}.
Particle flow reconstruction is done in two main steps: identifying PF elements and then linking those elements to reconstruct particles. Charged hadrons are identified by linking a track to an HCAL cluster while neutral hadrons are identified by HCAL clusters without track links. Similarly, electrons are identified with a track and an ECAL cluster with no link to an HCAL cluster, while electrons are identified with an ECAL cluster with no tracking link. Muons are identified by a track in the inner tracker connected to a track in the muon detectors.
Fig. 3.7 shows a 65 GeV simulated jet in the CMS detector, made of only five particles for illustrative purposes: two charged hadrons (π^+ and π^-), two photons (from the decay of a π^0) and a neutral hadron ($\mathrm{K}^0_{\mathrm{L}}$). The two photons, the π^- and the $\mathrm{K}^0_{\mathrm{L}}$ produce clusters in the ECAL, denoted as $\mathrm{E}_{1,2,3,4}$. The two charged pions are reconstructed as two bent tracks, $\mathrm{T}_{1,2}$, pointing towards two HCAL clusters, $\mathrm{H}_{1,2}$.
After identifying the particles, PF jets are reconstructed using jet clustering algorithms. Recombinational algorithms define a distance between pairs of particles, perform successive recombinations of the pair of closest particles, and stops when all resulting objects

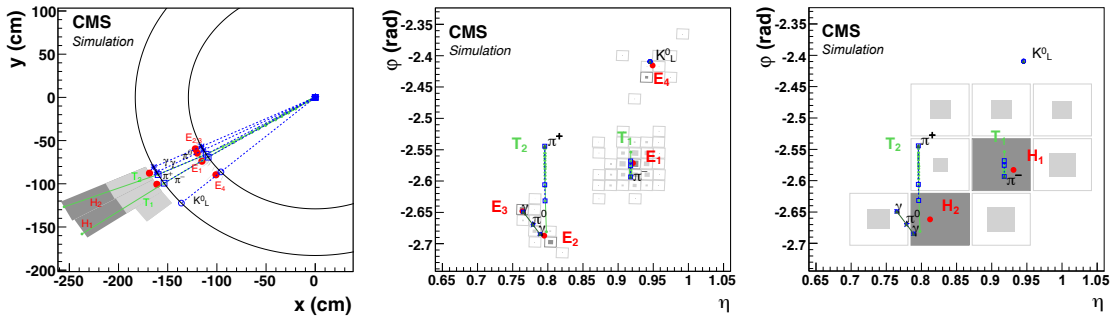

Figure 3.7: Event display of an illustrative jet made of five particles only in the (x, y) view (left), ECAL (η, ϕ) view (middle) and HCAL (η, ϕ) view (right) [111]. The cluster positions are represented by dots, the simulated particles by dashed lines, and the positions of their impacts on the calorimeter surfaces by various open markers.

are too far apart [112]. The distance between two particles i and j is defined as:

$$d_{i,j} = \min(k_{t,i}^{2p}, k_{t,j}^{2p}) \frac{\Delta y_{i,j}^2 + \Delta \phi_{i,j}^2}{R^2} \tag{3.1}$$

and the distance between any particle i and the beam as:

$$d_{iB} = k_{t,i}^{2p} \tag{3.2}$$

$k_{t,i}$ and $k_{t,j}$ are transverse momenta, R is the radius parameter that determines the final size of the jet, and p is the parameter that governs the relative power of the energy versus geometrical scales. $p = 1$ for the k_t algorithm, $p = 0$ for the Cambridge/Aachen algorithm and $p = -1$ for the anti-k_t algorithm [113].
In an event with a few well-separated hard particles with transverse momenta k_{t1}, k_{t2}... and many soft particles, the anti-k_t algorithm starts by computing all distances $d_{i,j}$ and d_{iB} and find the smallest. If the smallest is a $d_{i,j}$ the two particles i and j are combined. Soft particles cluster with hard ones long before they cluster among themselves since $d_{i,j}$ between a hard and a soft particle is exclusively determined by the k_t of the hard particle. If the smallest distance is a d_{iB} the particle i is removed and called a jet. This process is repeated until all particles are clustered into jets [114].
The intense environment created in central PbPb collisions is one of the major challenges in jet reconstruction. The uncorrelated background within the selected jet cone may worsen the jet energy resolution. A local subtraction of the Underlying Event (UE) is performed at the level of individual jet constituents, called Constituent Subtraction (CS) [115]. The first step is to determine the UE energy density, expressed in the transverse momentum density ρ and mass density ρ_m, by grouping all the particles in the event into patches using the k_t jet clustering algorithm. Each patch has a $p_{\mathrm{T,patch}} = \sum_i p_{\mathrm{T,i}}$ and mass $m_{\delta\mathrm{patch}} = \sum_i \left(\sqrt{m_i^2 + p_{\mathrm{T,i}}^2} - p_{\mathrm{T,i}} \right)$, determined by summing over all the particles (i)

in the batch, and covers a certain area A_{patch} in the (η,ϕ) plane.
ρ and ρ_m are then estimated as [116]:

$$\rho = \text{median}_{\text{patches}}\{p_{T,\text{patch}} / A_{\text{patch}}\} \tag{3.3}$$

$$\rho_m = \text{median}_{\text{patches}}\{m_{\delta\text{patch}} / A_{\text{patch}}\} \tag{3.4}$$

The next step is to subtract a specified amount of those densities using soft massless particles, called "ghosts", uniformly covering the (η,ϕ) plane with high density.
The jet clustering is run again over the original and ghost particles. Each ghost particle covers an area A_g and has p_T^g and m_δ^g that can be expressed as:

$$p_T^g = A_g.\rho \tag{3.5}$$

$$m_\delta^g = A_g.\rho_m \tag{3.6}$$

The UE removal proceeds iteratively over all particle-ghost pairs starting from the closest pair. With each iteration, the particle and ghost p_T and mass are changed. If the p_T of the particle is greater or equal to the p_T of the ghost, the p_T of the ghost is subtracted from the p_T of the particle and then set to 0. Otherwise, the p_T of the particle is subtracted from the p_T of the ghost and then set to 0. The same is done to the mass. The process is terminated when the end of the list is reached. The momenta of jets are recomputed with the subtracted constituent momenta.
Specifically for this analysis, the jets are originally reconstructed by running the anti-k_t algorithm, with R=0.3 to minimize the effects of the heavy-ion background fluctuations, using the stable particles provided by particle flow. Particularly at lower values of J/ψ p_T, however, the two decay muons tend to have an opening angle with is comparable to the size of the jet. As a consequence, the J/ψ may be reconstructed in more than one jet. To rectify this the jets are reclustered, replacing the decay muons with the J/ψ candidate, after applying the full J/ψ selection. The analogous procedure is applied at generator level to recluster generator-level jets in the simulation. The underlying event in PbPb is subtracted using the CS method but no energy is subtracted from the J/ψ itself, which is defined as coming from the primary hard-scattering. Rather the subtracted energy is distributed amongst the other particles in the jet, which may originate from other nucleon-nucleon scatterings.

3.5 Selection

3.5.1 Single muon kinematic cuts

The single muon acceptance cuts are optimized in p_{T}-η bins using a prompt J/ψ MC sample by requiring the number of muons passing the trigger, reconstruction, and identification algorithms to be more than 10% of the total number of generated muons. The distribution of this ratio is shown in Fig. 3.8 and the acceptance cuts shown in green on the plots are elaborated in Eq. 3.7.

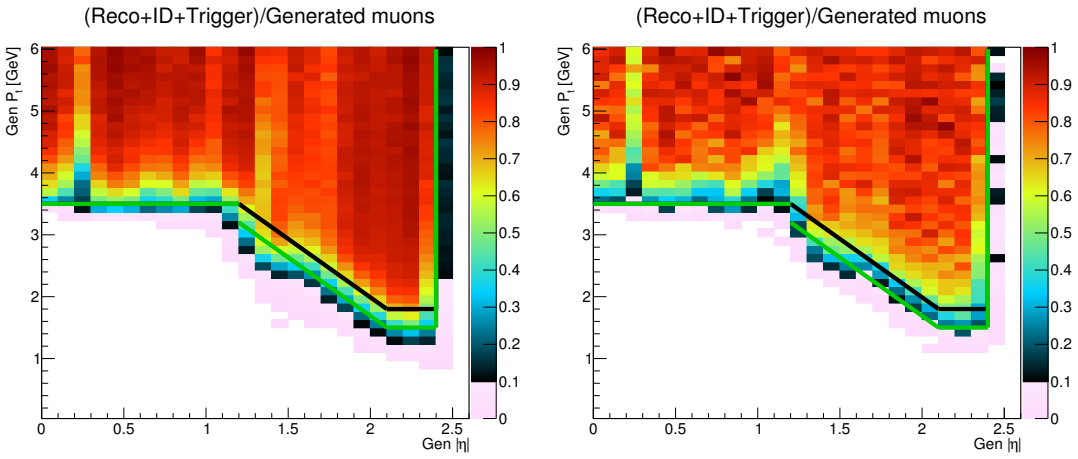

Figure 3.8: The number of muons passing the trigger, reconstruction and identification cuts over the total number of generated muons for pp (left) and PbPb (right). The acceptance cuts used for the 2018 PbPb and 2017 pp data are shown in green compared to the previous cuts used for the 2015 data shown in black.

$$\begin{aligned} p_{\mathrm{T}}^{\mu} &> 3.5\mathrm{GeV}/c && \text{for } |\eta^{\mu}| < 1.2 \\ p_{\mathrm{T}}^{\mu} &> (5.47 - 1.89 \times |\eta^{\mu}|)\mathrm{GeV}/c && \text{for } 1.2 \leq |\eta^{\mu}| < 2.1 \\ p_{\mathrm{T}}^{\mu} &> 1.5\mathrm{GeV}/c && \text{for } 2.1 \leq |\eta^{\mu}| < 2.4 \end{aligned} \tag{3.7}$$

3.5.2 Muon identification

The muons are required to pass a *soft* identification selection, optimized for low p_{T} muons:

- The muon needs to be a tracker muon and a global muon.
- The muon left hits in at least one pixel layer to suppress muons from decays in flight.
- The muon track created hits in at least six layers in the inner tracker, to ensure good p_{T} measurement.

- The absolute distance from the muon to the primary vertex is less than 0.3 cm in the transverse plane and less than 20 cm in the longitudinal plane, to reduce the cosmic-ray background.

3.5.3 J/ψ selection

The J/ψ selection requires the two muons to pass the single muon ID cuts explained in the previous section. It also requires the muons to have opposite charges and to have a χ^2 probability larger than 1% to be derived from a common vertex.
In order to ensure that the muons are associated with the online muons that fired the dimuon triggers explained in Section 3.2, a matching procedure is done by defining ΔR:

$$\Delta R = \sqrt{(\eta_{\text{reco}} - \eta_{\text{online}})^2 + (\phi_{\text{reco}} - \phi_{\text{online}})^2} \tag{3.8}$$

In pp collisions, the two muons need to be matched to L1 muons, whereas in PbPb collisions the two muons need to be matched to an L2 muon and at least one needs to be matched to an L3 muon. The threshold is $\Delta R < 0.3$ for L1 and L2 muons and $\Delta R < 0.1$ for L3 muons since the (η,ϕ) position resolution is better for the L3 muons because they are reconstructed using the muon system and tracker information.
The J/ψ candidates have $p_{\text{T}} > 6.5$ GeV and have an invariant mass within the $2.6 < m_{\mu^+\mu^-} < 3.5$ GeV range.

3.5.4 Jet selection

The reconstructed jets are required to be in the range $\eta < 2$, in order to be fully contained in the tracker region. The jet measurement is performed for the range $30 < p_{\text{T}} < 40$ GeV. In order to capture bin migration effects, we measure jets in a large range of $6.5 < p_{\text{T}} < 60$ GeV, as input to an unfolding procedure. The wider p_{T} selection is found to be around 99% efficient for jets in the nominal p_{T} range in simulation, for both the prompt and nonprompt J/ψ samples.

3.6 The analysis strategy to measure z distributions

z, the observable of interest in this thesis, is the fraction of the jet p_T taken by the J/ψ:

$$z = p_{T,J/\psi} / p_{T,jet} \tag{3.9}$$

To get the z distributions of prompt (and nonprompt) J/ψ mesons in pp and PbPb, the analysis procedure was derived in two main sections: to extract the J/ψ signal in z bins and to unfold the bin migration effects.
The analysis workflow is summarised in the schema in Fig. 3.9.

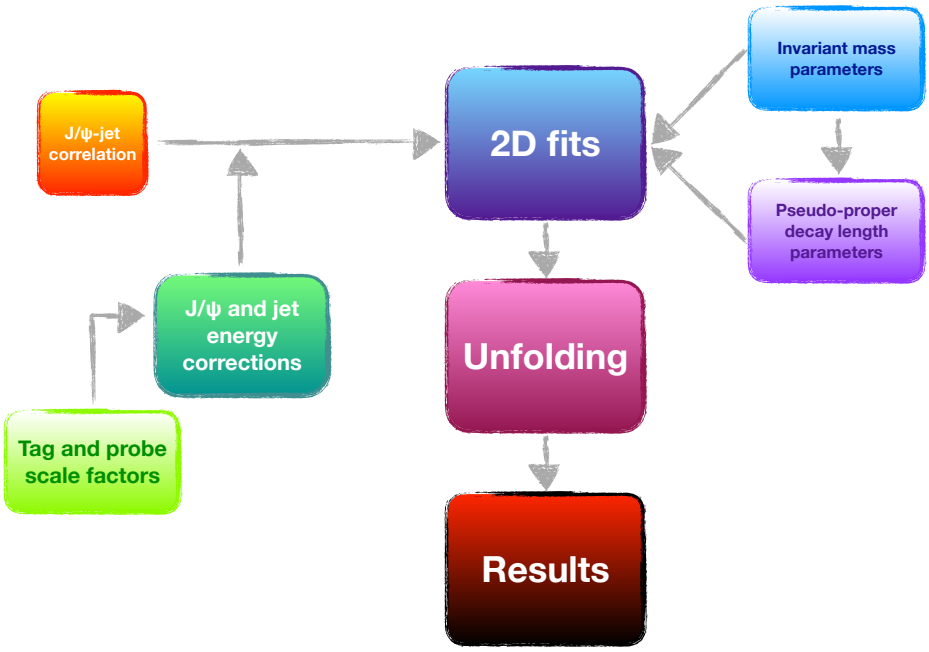

Figure 3.9: The different steps of the analysis.

After reconstructing the J/ψ candidates and the jets. z is measured for each J/ψ-jet pair. For each pair that passes the selections in Section 3.5, J/ψ acceptance and efficiency corrections and Jet Energy Corrections (JEC) are applied. The J/ψ corrections are described in Section 3.7 and the JEC described in Section 3.8.
The next step is to use two-dimensional fitting of the dimuon ($\mu^+\mu^-$) invariant mass and pseudo-proper decay length distributions to get the yields of prompt and nonprompt J/ψ. The fitting is done in multiple steps. First, we fit the invariant mass distributions in MC simulations then we use the results to fix certain parameters when fitting in data. Then comes the pseudo-proper decay length part, where we have four contributions: the $\ell_{J/\psi}$ error distributions, the lifetime resolution, the b hadron decay length, and

the $\ell_{J/\psi}$ distributions of the background dimuons. The 2D fits are the final step on the prompt/nonprompt yield extraction. We use as input the parametrization of the invariant mass and pseudo-proper decay length distributions obtained in the previous steps. This is described in section on signal extraction (Section 3.9).
Before obtaining the final results we apply an unfolding procedure to correct for bin migration, due to the finite jet p_T resolution. This procedure is carried out in two dimensions, jet p_T and z, and is described in Section 3.13.

3.7 J/ψ corrections

Due to the detector's acceptance and efficiency, some J/ψ mesons are not reconstructed or get rejected by the selection mentioned in Section 3.5. The acceptance and efficiency need to be estimated in order to correct the J/ψ yields. The J/ψ acceptance and efficiency corrections are determined in simulation in finely binned maps of J/ψ p_{T}, η, and (in the case of PbPb efficiency) collision centrality. The correction is applied as a weight factor to each J/ψ prior to the signal extraction. The bin size is discussed after the acceptance and efficiency sections.

3.7.1 Acceptance

The detector acceptance depends on the p_{T} and rapidity spectra of the J/ψ. It is defined as the fraction of the generated dimuons that has both muons passing the acceptance cuts listed in Eq. (3.7) in Section 3.5. The acceptance is therefore computed with the following definition:

$$\mathrm{Acc} = \frac{N(\text{generated dimuons, both muons pass acceptance cuts})}{N(\text{all generated dimuons})} \tag{3.10}$$

The acceptance map, estimated using pp MC simulation, is shown in Fig. 3.10 as a function of the dimuon y and p_{T} for J/ψ with $p_{\mathrm{T}} > 6.5$ GeV. The acceptance is governed by the CMS muon kinematic coverage. High p_{T} or forward rapidity J/ψ mesons are more likely to decay to muons that can reach the muon stations than mid-rapidity or low p_{T} J/ψ.

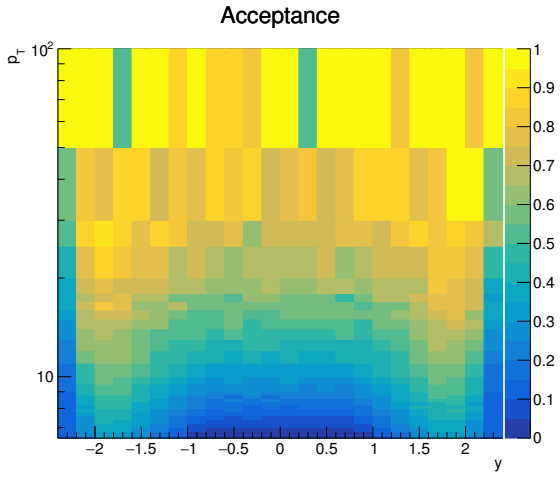

Figure 3.10: Acceptance of prompt J/ψ as a function of p_{T} and rapidity in pp MC events.

3.7.2 Efficiency

The reconstruction, identification, and trigger efficiencies were computed as one total efficiency. The efficiency depends on the J/ψ kinematics and, in PbPb, the centrality of the collision. It is defined as the number of reconstructed dimuons passing the analysis selection over the number of the generated dimuons in the acceptance, and expressed as:

$$\text{Eff} = \frac{N(\text{reconstructed dimuons, passing analysis cuts})}{N(\text{generated dimuons, both muons passing acceptance cuts})} \tag{3.11}$$

The analysis selection explained in Section 3.5 includes the dimuon selection, the muon acceptance and identification criteria, and the trigger selection. The reconstructed muons are also required to be matched to generated muons. The efficiency is derived from pp and PbPb MC samples as 2D maps of J/ψ y and p_{T}. Multiple maps were used in the PbPb case, each corresponding to a collision centrality range.
All single muons are corrected with tag-and-probe scale factors that will be discussed in Section 3.7.3

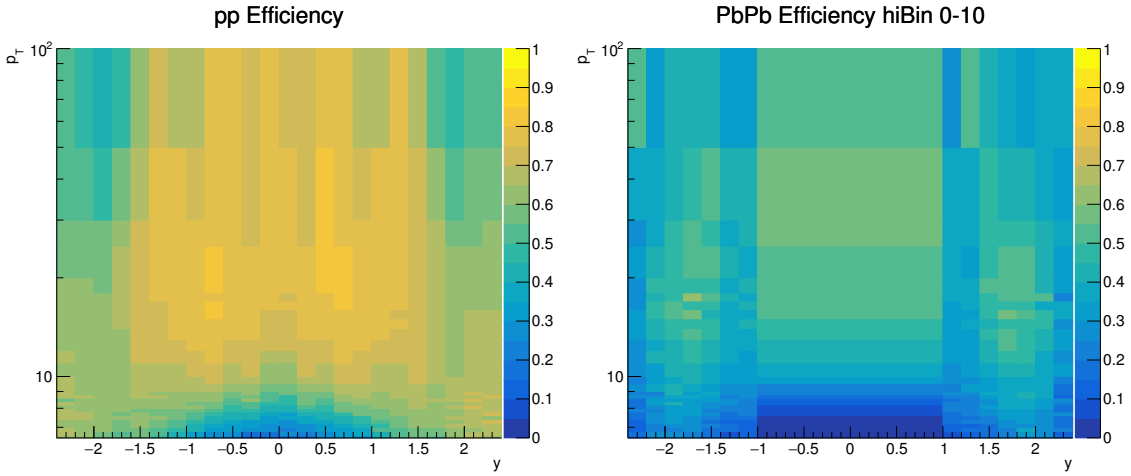

Figure 3.11: The efficiency of prompt J/ψ as a function of p_{T} and rapidity in pp (left) and the most 5% most central PbPb (right) MC events.

The efficiency corrections, for prompt J/ψ in pp and PbPb collisions are presented in Fig. 3.11, as a function of p_{T} and rapidity. In the case of PbPb, the 0–5% centrality selection is shown.

Acceptance and efficiency bins

The binning of the corrections had to be carefully chosen to minimize the sensitivity of the corrections to the underlying shape of the distributions in MC, but within the statistical constraints of the large, but still finite MC samples. This is particularly true in PbPb, where three binning dimensions are needed.

To test the statistical precision of the Acc×Eff maps, a closure test was performed by splitting the MC into two statistically independent samples. One was used to compute the corrections which are then applied to the second. The corrected reconstructed distributions should match the generated distributions. To the extent that this is not the case, it indicates that the bins are too small and the corrections are fluctuating because of the statistics. Looking at the dependence of the efficiency on the three variables, the number of bins was increased until a nonclosure is seen. Fig. 3.12 shows the results of the closure test in pp (left), where the correction is done in 2D (p_{T} and y), and in PbPb (right), where the correction is done in 3D (p_{T} and y and centrality). A deviation of around 2% starts to be visible at the lowest value of J/ψ used in this analysis. This level of nonclosure is small compared to the other sources of systematic uncertainty and is hence acceptable. It does indicate, however, that we are approaching the limit of how finely we can bin. It should be noted that the true level of nonclosure should be a factor of $\sqrt{2}$ smaller, as this test reduces by half the number of events used for the map. Several other choices were also explored, by rebinning one axis and binning more finely another, but the observed difference in the closure test was negligible.

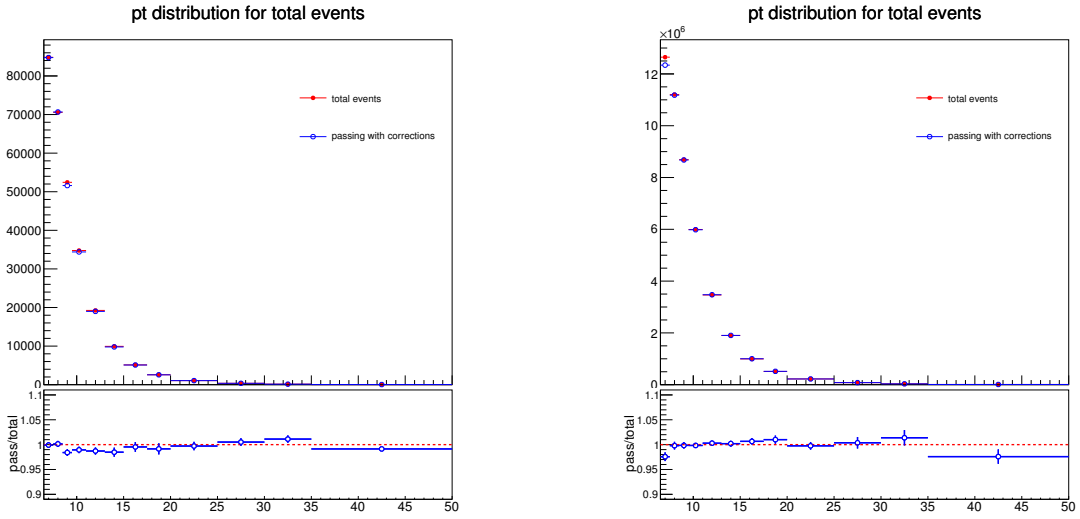

Figure 3.12: Closure tests for the 2D efficiency correction map used in pp (left) and 3D map used in PbPb (right).

Once the choice of fine binning was settled, a check was needed to verify that finite bin size effects were under control. To do this, the shape of the spectrum in MC was varied, taking advantage of two weight factors that are applied. The MC simulations are done with a flattened $\hat{p}_{\mathrm{T}}$ distribution to populate large values of J/ψ p_{T}. A per-event weight factor then applied, such that the natural shape of the $\hat{p}_{\mathrm{T}}$ distribution is restored. The PbPb MC is also produced by embedding into a minimum-bias (i.e., without any centrality selection/bias) background sample. The second weight factor applied is to weight events by N_{coll}, to simulate the effect of the hard scattering centrality bias. The finite bin

size effects are tested by removing both of these weight factors. In order to avoid possible variations from the fitting procedure, we simply applied a tight restriction on the dimuon invariant mass. Fig. 3.13 shows the ratio of the inclusive (i.e., without any jet requirement) J/ψ p_{T} distribution, as well as the z distribution with the nominal jet selection. The bias on the results is within 1%. It should be noted that the difference in the spectral shape induced by removing these weights is far larger than the possible data/MC difference. Hence we assume that the finite bin size bias is negligible. The baseline corrections are chosen to be the ones without the weights applied, as this simplifies the evaluation of the statistical uncertainty on the Acc$\times$Eff from the MC, as evaluated in Section 3.10.4.

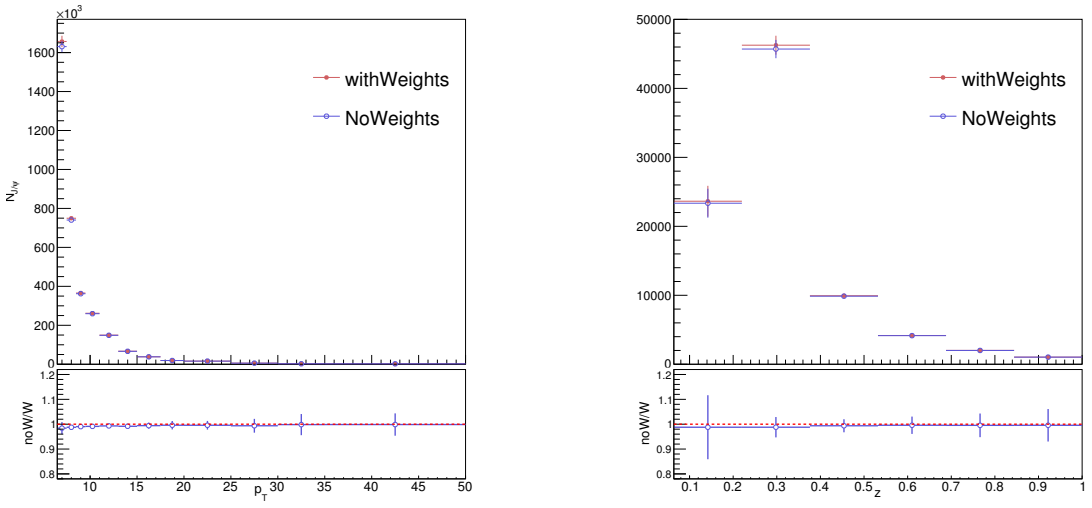

Figure 3.13: p_{T} and z distributions using corrections derived with and without MC weights.

3.7.3 Tag-and-probe scale factors

The estimation of the efficiency from MC is based on the assumption of the perfect description of the detector response in the simulation, which is not possible.
In order to take into account possible discrepancies between the efficiencies in simulation and those in data, a data-driven method, the J/ψ efficiencies are corrected with a set of scale factors derived with the tag-and-probe (T&P) method [96].
T&P is a data-driven method that uses a known decay of mass resonance (e.g. J/ψ, Y, Z) to estimate the efficiency of a selection criterion, by defining a "tag" which is an object, e.g. muon, that passes a tight selection, and paring it with another object that passes very loose selection called "probe" for which the probability to pass the selection in question is checked. The fake rate of the tag selection should be very small ($<<$ 1%), and the invariant mass of the tag and probe combination should be consistent with the mass resonance. For the J/ψ efficiencies, the J/ψ resonance is used and the tag and the probe are muons.

The probes are categorized into three groups: "All probes", "Failed probes", and "Passing probes", referring to the selection criteria. The invariant mass distribution of the tag-probe pair is fitted for the three cases and the yields are extracted. The efficiency is then calculated by dividing the obtained yields of the passing pairs by the obtained yields of all pairs. An example of the mass fits of the T&P pairs for the three probe classes in data is shown in Fig. 3.14.

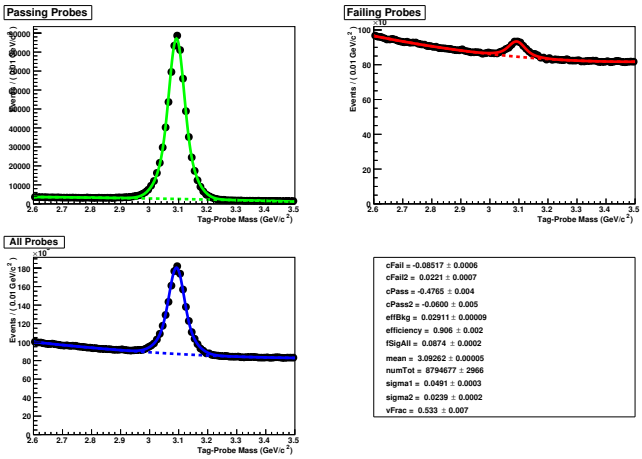

Figure 3.14: Fits to the tag-and-probe invariant mass distribution for passing (top left), failing (top right), and all (bottom left) probes [117].

One of the advantages of the T&P method is that it can be used for data and simulation providing a direct comparison between the two.
The efficiencies are calculated in data and MC for various kinematic ranges of the probe and event centrality bins. The data/MC ratios are then used when computing the J/ψ efficiency in MC. The decay products of the J/ψ, the offline muons, are weighed J/ψ-by-J/ψ using the T&P corrections while filling the numerator of the efficiency. These scale factors are computed centrally by a T&P team for all dimuon analyses and documented in the internal analysis note AN-18-316 [117]. I was part of the team and was responsible for providing the scale factors for the low p_T muons in the 2018 PbPb data.

Scale factors for 2017 pp data

Two efficiencies we derived for the 2017 pp data with the T&P method: the "global" efficiency, which is the efficiency of the global reconstruction, and the "trigger+ID" efficiency, that checks the efficiency of the trigger and the muon identification cuts.
The tags for both efficiencies are selected using the same criteria: a high-quality muon passing the acceptance and quality identification cuts, matched to a single muon trigger. The "global" reconstruction efficiency starts from general tracks in the inner tracker and checks if they are reconstructed as global-muon tracks. The global efficiency was found to be η and p_T dependent. Therefore, the scale factors are derived as a function of p_T in $|\eta|$ bins. The efficiencies for data and MC are shown in Fig. 3.15 with the scale factors

shown in the lower panels.

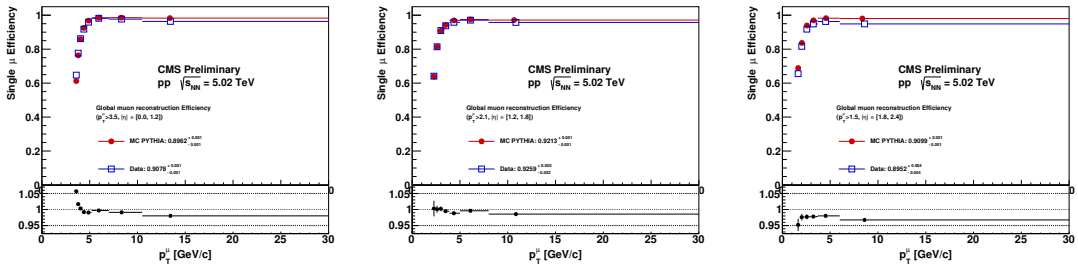

Figure 3.15: The efficiency of global reconstruction in pp data (blue) and MC (red) as a function of the probe p_T in three $|\eta|$ bins. The lower panels show the scale factors [117].

The "trigger+ID" efficiency is calculated as the fraction of global muons that pass the trigger and identification selection. This efficiency is also p_T and η dependant.
The p_T dependance is shown in Fig. 3.16 separately for the four $|\eta|$ bins: [0, 1.2], [1.2, 1.8], [1.8, 2.1], and [2.1, 2.4]. The lower panels of the plots show the scale factors.

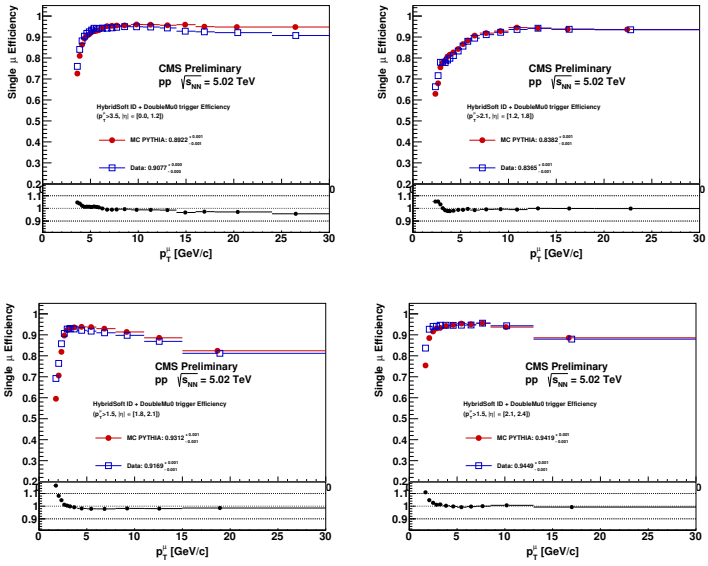

Figure 3.16: The efficiency of muon identification and trigger selection in pp data (blue) and MC (red) as a function of the probe p_T in three η bins. The lower panels show the scale factors [117].

Scale factors for 2018 PbPb data

For the 2018 PbPb data, three scale factors are derived: the tracking, the muon identification, and the trigger. The tag is defined as a high-quality muon passing the acceptance and quality identification cuts, matched to a single muon trigger.
The tracking efficiency is defined as the fraction of standalone muons that are reconstructed as global muons. It is found to only depend on η. The η dependence is shown in Fig. 3.17.

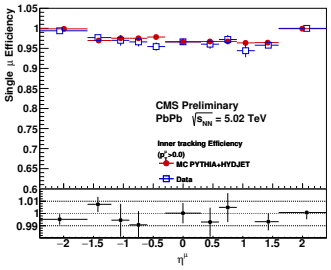

Figure 3.17: The tracking efficiency of muons in PbPb data (blue) and MC (red) as a function of η. The lower panels show the scale factors [117].

The muon identification efficiency is computed starting from global-muon probes and checking if they pass the muon identification cuts. The p_{T} dependence in η bins is shown in Fig. 3.18.

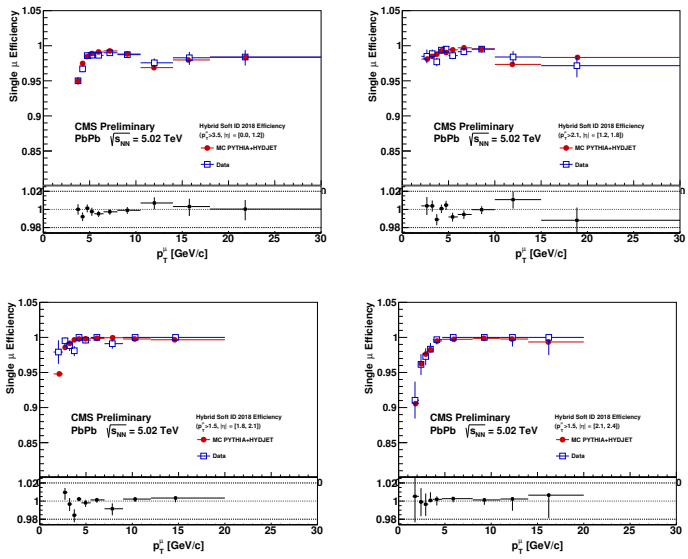

Figure 3.18: The efficiency of muon identification in PbPb data (blue) and MC (red) as a function of the probe p_{T} in three η bins. The lower panels show the scale factors [117].

As explained in Section 3.2, the PbPb trigger is made of three filters: an L2 muon filter, an L3 muon filter, and a dimuon mass filter. The mass cut is wide enough for the effect of the last filter on the efficiency to be negligible.
The efficiencies were computed separately for the L2 and L3 filter providing separate scale factors. The definition of the probes, however, is the same, starting from muons that pass the muon identification cuts. Passing muons need to be matched to the corresponding filter. The scale factors in both cases are derived as a function of p_{T} in $|\eta|$ bins. The efficiency of the L3 filter was found to be centrality dependant but the scale factors did not depend on centrality so only the p_{T} dependence in $|\eta|$ is used.
The efficiencies are shown in Fig. 3.19 for the L2 filter on top and the L3 filter at the bottom in four $|\eta|$ ranges: [0, 1.2], [1.2, 1.8], [1.8, 2.1], and [2.1, 2.4].

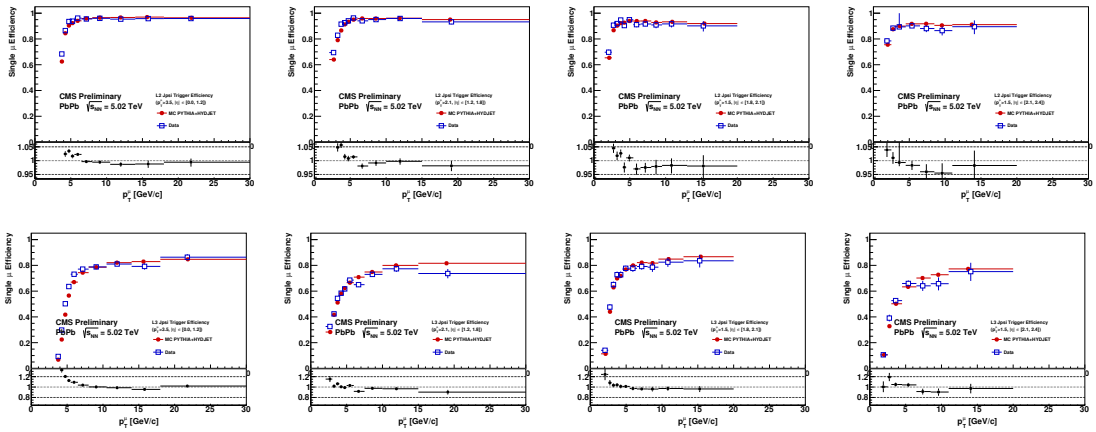

Figure 3.19: The efficiency of the trigger filters in PbPb data (blue) and MC (red) as a function of the probe p_{T} in three η bins. The top plots correspond to the L2 filter and the bottom plots correspond to the L3 filter. The lower panel of each plot shows the scale factors [117].

3.8 Jet energy corrections

Jets are reconstructed using the PF algorithm, as described in Section. 3.4, which uses information from all subdetectors to individually reconstruct each particle in the event. The jet response is the ratio of reconstructed jet p_T over the generator-level p_T.
The momentum determination of the charged component of jets is driven by the tracking, so the response requires very little additional calibration. On the other hand, the neutral components, especially the neutral hadrons, tend to be under-corrected for lower values of p_T. The Jet Energy Corrections (JEC) [118] are necessary due to the non-linear response of calorimeters.
Two types of corrections are applied: simulated jet response corrections and residual corrections for the differences between data and simulation.
The simulated jet response corrections are taken from MC simulation where the evolution of the electromagnetic and hadronic showers, as well as their interactions with the detector material, is well described. MC simulates the fragmentation of the initial quarks and gluons and contains a detailed model of the detector geometry, calibrations, and readout electronics, providing an accurate description of the jet response and, subsequently, energy corrections [118].
The simulated response R for a particular reconstructed p_T and η is computed in generated-level p_T, noted as $p_{T,gen}$, and η bins. In a QCD dijet sample, the generated-level jets are matched to the closest reconstructed jet within a radial distance of less than half the cone size of the jet. The ratio of the arithmetic means of the transverse momenta of the matched reconstructed and generated jets is then taken as the simulated response R:

$$R[\langle p_T \rangle, \eta] = \frac{\langle p_T \rangle}{\langle p_{T,gen} \rangle}[\langle p_{T,gen} \rangle, \eta] \tag{3.12}$$

The JEC is then obtained by simply inverting the true response. Figure 3.20 shows the applied JECs for pp (red) and PbPb (black) data as a function of η at a jet p_T value of 30 GeV.
In analogy to the T&P scale factors for J/ψ corrections, residual data/simulation scale factors are needed to cover the discrepancies in the jet response between data and simulation. The scale factors are also derived from a QCD dijet sample. In the case of PbPb collisions, only events of 50-100% centrality are used to avoid jet quenching effects. The jet response is studied using two methods: the p_T balance and MPF (missing transverse momentum projection fraction) which considers the response of the whole hadronic activity in the event. The residual corrections are derived in two steps: a "relative" correction which flattens the detector response as a function of η in narrow ranges of p_T, followed by an "absolute" correction, which corrects the energy scale as a function of p_T. The η-dependant corrections are obtained in dijet event by defining a "tag" jet with $\eta < 1.3$ and a "probe" jet without a pseudorapidity constraint. Since the barrel jet has poor resolution, the residual JECs are binned in bins of average jet p_T where $p_{T,ave} = 1/2(p_{T,tag} + p_{T,probe})$. The relative response for the p_T-balance and MPF is then defined

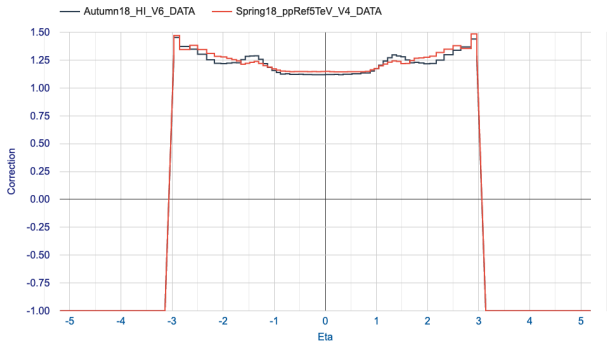

Figure 3.20: The jet energy corrections applied to real data as a function of η at a jet p_{T} value of 30 GeV.

using $p_{\mathrm{T,ave}}$:

$$R_{\mathrm{rel}}^{p_{\mathrm{T}}} = \frac{1+\langle\mathcal{A}\rangle}{1-\langle\mathcal{A}\rangle}, \text{ where } \langle\mathcal{A}\rangle = \frac{p_{\mathrm{T,tag}} - p_{\mathrm{T,probe}}}{2p_{\mathrm{T,ave}}} \tag{3.13}$$

$$R_{\mathrm{rel}}^{\mathrm{MPF}} = \frac{1+\langle\mathcal{B}\rangle}{1-\langle\mathcal{B}\rangle}, \text{ where } \langle\mathcal{B}\rangle = \frac{\vec{p}_{\mathrm{T}}^{\,\mathrm{miss}}.(\vec{p}_{\mathrm{T,tag}}/p_{\mathrm{T,tag}})}{2p_{\mathrm{T,ave}}} \tag{3.14}$$

The response is found to be flat in the barrel region, with no difference between the p_{T}-balance and MPF methods. In the endcaps, however, the response has a small p_{T}-dependance and some difference between the two methods, which will be taken into account in the systematic uncertainties. The Data /MC response ratio is shown in Fig. 3.21 as a function of p_{T} for different η bins, for both the p_{T}-balance and the MPF methods. To take the p_{T}-dependance into account, the η-dependent corrections are parameterized with a log-linear p_{T}-dependence, according to the formula $p_0 + p_1.\log(p_{\mathrm{T}})$. The correction factors are obtained from a p_{T}-dependent fit of the corrections.

The absolute Jet Energy Scale (JES) is determined using γ-jet events with jets of $|\eta| < 1.3$ from a p_{T} of 30 GeV to 500 GeV. In the case of PbPb collisions, only peripheral events are used to avoid jet quenching effects. The basic idea is to exploit the transverse momentum balance between the jet to be calibrated and the recoiling photon. The p_{T}-balance and MPF methods are both used with the following response definitions:

$$R_{\mathrm{jet}}^{p_{\mathrm{T}}} = \frac{p_{\mathrm{T,jet}}}{p_{\mathrm{T,fl}}} \tag{3.15}$$

$$R_{\mathrm{jet}}^{\mathrm{MPF}} = 1 + \frac{\vec{p}_{\mathrm{T}}^{\,\mathrm{miss}}.\vec{p}_{\mathrm{T,fl}}}{(p_{\mathrm{T,fl}})^2} \tag{3.16}$$

Ref. [118] provides more details about how the corrections take into account the biases from initial- and final-state radiation, underlying event, and out-of-cone showering.
All the JECs explained this far are used by jet analyses in the CMS heavy-ion group.

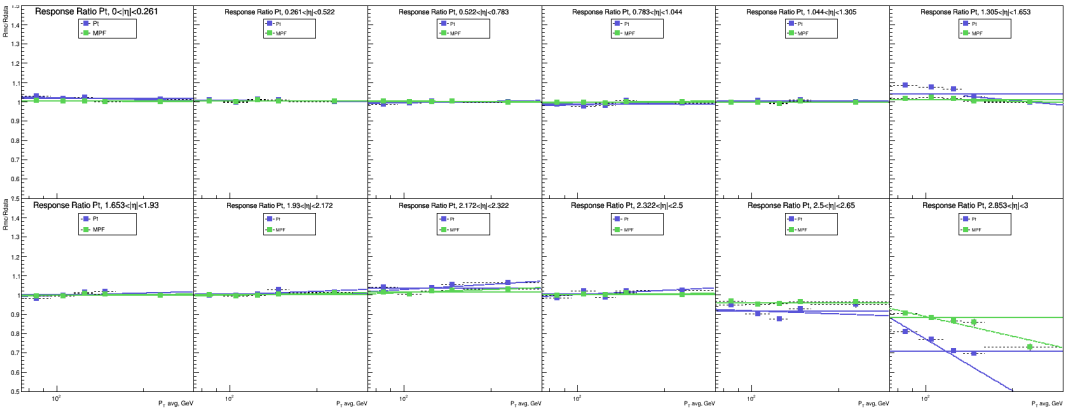

Figure 3.21: Data/MC response ratio versus p_{T} for various η bins, for both p_{T}-balance and MPF methods. Two functions are used to fit the ratios: a uniform and a log-linear function.

They documented in the internal analysis note AN-19-017 [119]. The following procedure, however, is specific for this analysis.

Since the JECs are derived from an ensemble of inclusive jets, they average over all jet fragmentation patterns. In this analysis, however, the yield of jets is measured as a function of the jet fragmentation variable z. The response of jets as a function of the generator-level z is shown in Fig. 3.22 in pp (left) and PbPb (right) collisions. The open symbols show the response with the standard JECs, for both prompt and nonprompt J/ψ-jets. For pp collisions, as the value of z gets small, the response approaches unity, indicating that the standard JECs are appropriate. As z approaches one, however, the response is too large.
In the limit of $z = 1$, the jet consists of a single J/ψ. Since the momentum of the decay muons is measured very precisely by the tracker, the jet kinematics are already close to the truth value *before* the application of the JECs. The size of the overcorrection at large z corresponds to the value of the JEC at that value of p_{T} (averaged over η).
To flatten the response vs. η, a rather simple procedure was developed specifically for J/ψ-jets. Rather than applying the full JEC to the jet, it is only applied to the non-J/ψ component of the jet. The new p_{T} of the jet after this procedure is obtained by combining the value with the standard correction $p_{\mathrm{T,rec}}$ with the raw value without any correction $p_{\mathrm{T,raw}}$, using the measured value of z, as follows.

$$p_{\mathrm{T,new}} = (1 - z)\, p_{\mathrm{T,rec}} + z\, p_{\mathrm{T,raw}} \tag{3.17}$$

The response after this z-dependent correction is also shown in Fig. 3.22, in closed symbols. In pp collisions (left panel) one observes a much-reduced dependence on z after this residual correction. At large z the response is very close to unity, as expected. At

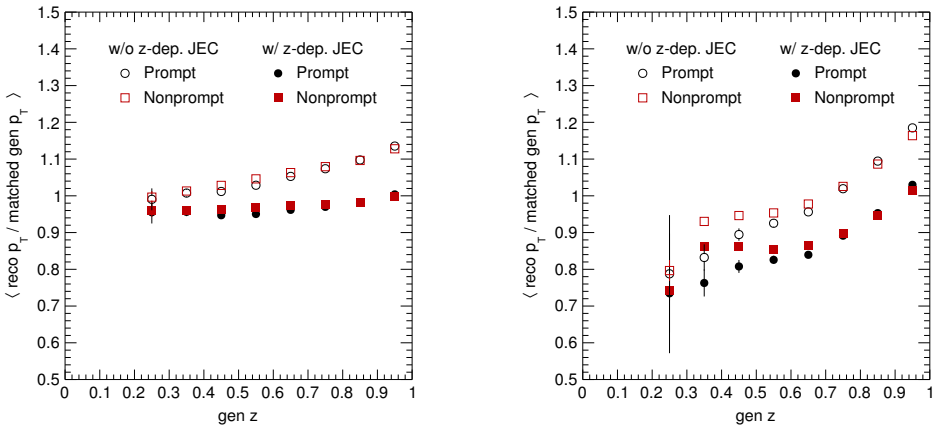

Figure 3.22: The response of J/ψ-jets vs. z, before (open symbols) and after (closed symbols) z-dependent corrections in pp (left) and PbPb (right) collisions. Prompt and nonprompt J/ψ are shown separately, as indicated in the legend.

low z the response is a few percent lower than unity, showing that the procedure works well, but is not exact. In PbPb collisions (right panel) one again observes that the high z response is (un)corrected to unity. However, the overall dependence of the response on z is not much different than before the application of the z-dependent corrections. This is due to the fact that the measured z value used in Eq. 3.17 has a poor correspondence with that of the generator-level one. An isolated J/ψ, for example, will often be reconstructed at a low value of z in PbPb, due to a downward local fluctuation of the underlying event. The residual z-dependence of the JES is left to be corrected for by the unfolding procedure, as described in Section 3.13, which is performed both as a function of jet p_{T}, and as a function of z. Nevertheless, the JECs play limiting the non-uniformity of the response in other variables that are not taken into account explicitly in the unfolding, in particular in η, over which the detector response to jets varies significantly.
Figures 3.23 and 3.24 show the response as a function of jet η in pp collisions for prompt and nonprompt J/ψ, respectively. Figures 3.25 and 3.26 show the same for PbPb. Again, the response is shown before the z-dependent corrections in open symbols and afterward in closed symbols. Different slices in z are shown as indicated in the legend. In all cases, the high z jets show a bow-shaped response with the standard corrections, which is effectively flattened by the z-dependent procedure. In pp collisions, the z-dependence is generally quite flat after the residual z corrections. The same small residual z-dependence is evident, as was shown in Fig. 3.22. In PbPb collisions, the larger remaining z-dependence is also again apparent. For each z bin the η-dependence of the response is fairly flat. A small remaining bow shape in the η-dependence of the response at low z (more visible in the nonprompt sample, due to its better statistics at low z) is within the size of the systematic uncertainty on the JES that will be discussed in Section. 3.14.

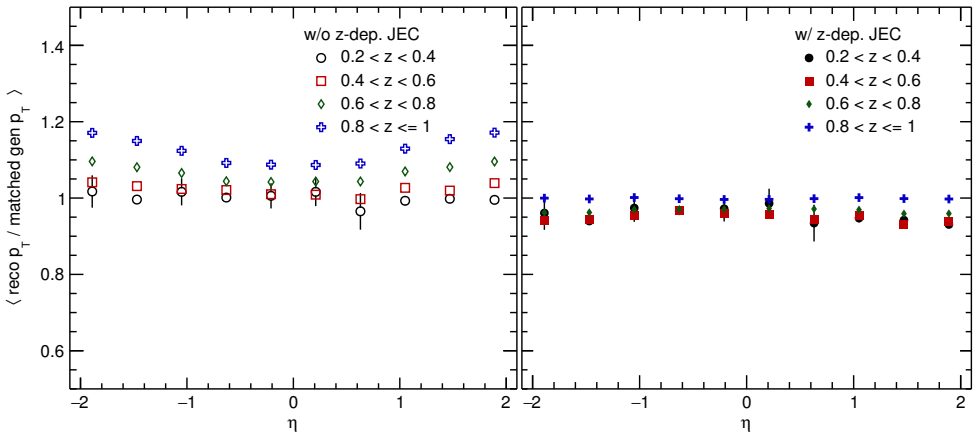

Figure 3.23: The response of prompt J/ψ-jets vs. η, before (left) and after (right) z-dependent corrections in pp collisions. Different slices in z are shown, as indicated in the legend.

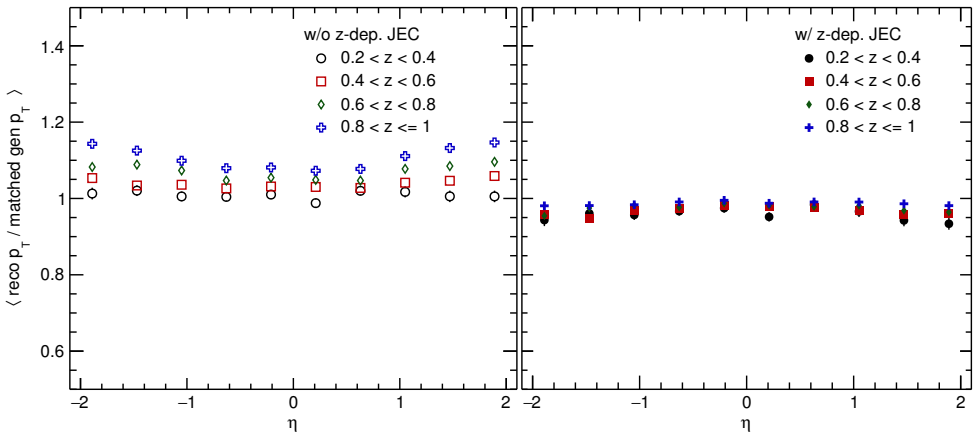

Figure 3.24: The response of nonprompt J/ψ-jets vs. η, before (left) and after (right) z-dependent corrections in pp collisions. Different slices in z are shown, as indicated in the legend.

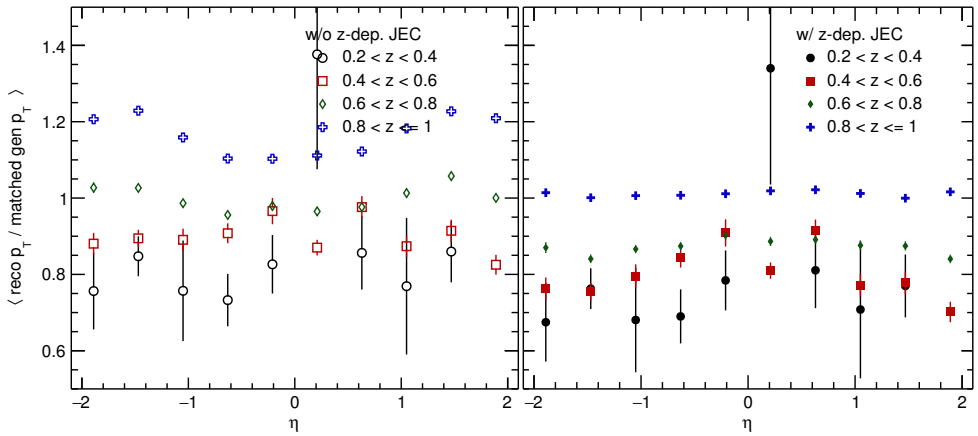

Figure 3.25: The response of prompt J/ψ-jets vs. η, before (left) and after (right) z-dependent corrections in PbPb collisions. Different slices in z are shown, as indicated in the legend.

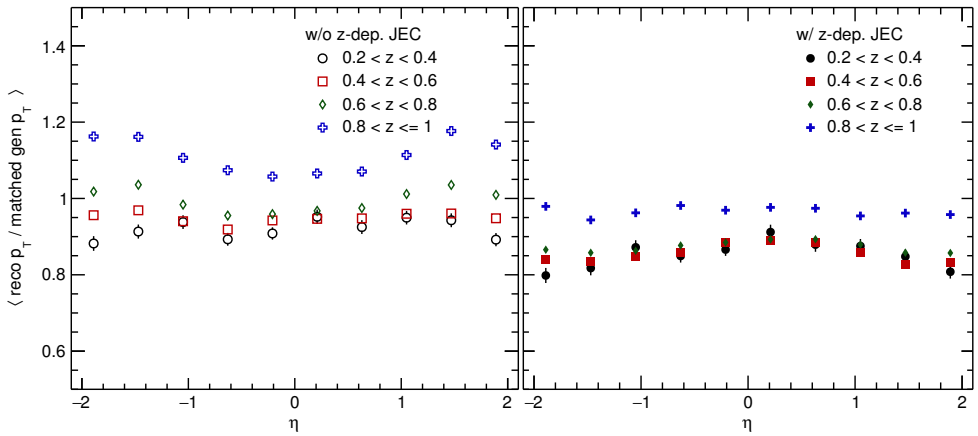

Figure 3.26: The response of nonprompt J/ψ-jets vs. η, before (left) and after (right) z-dependent corrections in PbPb collisions. Different slices in z are shown, as indicated in the legend.

3.9 J/ψ signal extraction

At this point in the analysis, z is calculated for each J/ψ-jet pair, using the corrected p_{T} for jets and assigning a weight factor using the J/ψ kinematic (and collision centrality for PbPb) to correct for the acceptance and efficiency of the detector. The next step is to separate prompt and nonprompt J/ψ mesons and extract their yields in the different z bins.

The nonprompt J/ψ component comes from the decay of b hadrons that have a large lifetime of $\tau_B \sim 1.5$ ps. The nonprompt mesons are identified by the measurement of a secondary $\mu^+\mu^-$ vertex displaced from the primary collision vertex. The most probable transverse b hadron decay length in the laboratory frame is calculated as:

$$L_{xyz} = \frac{\hat{u}^T S^{-1} \vec{r}}{\hat{u}^T S^{-1} \hat{u}} \tag{3.18}$$

where $\hat{u}$ is the unit vector in the direction of the J/ψ meson momentum p, $\vec{r}$ is the displacement vector between the $\mu^+\mu^-$ vertex and the primary vertex and S^{-1} is the inverse of the sum of the primary and secondary vertex covariance matrices.

From this, the pseudo-proper decay length is computed as an estimate of the b hadron decay length and defined as:

$$\ell_{\mathrm{J}/\psi} = L_{xyz} m_{\mathrm{J}/\psi} / p_{\mu\mu} \tag{3.19}$$

using the measured momentum $p_{\mu\mu}$ of the dimuon and the Particle Data Group [32] world average value of the J/ψ meson mass. The primary collision vertex is reconstructed by fitting the position of all tracks within a radius of 5 cm from the interaction region. The secondary vertex is determined by extrapolating the position of the closest approach between the two muon tracks.

The separation of the prompt and nonprompt J/ψ components is done using two methods in charmonia analyses. One is using a cut on the $\ell_{\mathrm{J}/\psi}$, where the dimuons with a $\ell_{\mathrm{J}/\psi}$ smaller than a certain threshold are considered as prompt and the ones above the threshold are considered nonprompt. The cut is usually a function of p_{T} and is rapidity-dependant. Since some prompt J/ψ can end up in the nonprompt sample (and vice versa) this procedure requires efficiency and contamination corrections. This method was used in Ref. [120] to extract the J/ψ and ψ(2S) yields in pp and PbPb to get the relative modification factor.

In the second method, which is used in this analysis, the signal extraction is based on a two-dimensional extended unbinned maximum likelihood fitting (2D fits) of the dimuon ($\mu^+\mu^-$) invariant mass and pseudo-proper decay length distributions for each analysis bin. In these fits the fraction of nonprompt J/ψ mesons (the so-called *b fraction*) is a free fit parameter. The fits need to take into account the signal and background in the two dimensions, so the expression for the total Probability Density Function (PDF) $F(\ell_{\mathrm{J}/\psi}, m_{\mu\mu})$, the functional form used for the 2D fit, is given by:

$$F(\ell_{\mathrm{J}/\psi}, m_{\mu\mu}) = N_{Sig} \cdot F_{Sig}(\ell_{\mathrm{J}/\psi}) \cdot M_{Sig}(m_{\mu\mu}) + N_{Bkg} \cdot F_{Bkg}(\ell_{\mathrm{J}/\psi}) \cdot M_{Bkg}(m_{\mu\mu}) \tag{3.20}$$

where:

- N_{Sig} is the number of signal dimuons (prompt and nonprompt J/ψ)
- N_{Bkg} is the number of background dimuons
- $F_{\rm Sig}(\ell_{\rm J/\psi})$ and $M_{\rm Sig}(m_{\mu\mu})$ are the functional forms that describe the signal $\ell_{\rm J/\psi}$ and mass shapes respectively
- $F_{\rm Bkg}(\ell_{\rm J/\psi})$ and $M_{\rm Bkg}(m_{\mu\mu})$ are the functional forms that describe the background $\ell_{\rm J/\psi}$ and mass shapes respectively

Due to the resolution of $\ell_{\rm J/\psi}$, the measured $\ell_{\rm J/\psi}$ is different from the *true* pseudo-proper decay length, noted $\ell'_{\rm J/\psi}$ in the following. The $\ell_{\rm J/\psi}$ signal and background shapes, $F_{\rm Sig,Bkg}(\ell_{\rm J/\psi})$, are therefore given by:

$$F_{\rm Sig,Bkg}(\ell_{{\rm J/\psi},i}) = F^{true}_{\rm Sig,Bkg}(\ell'_{{\rm J/\psi},i}) \otimes R(\ell_{{\rm J/\psi},i} - \ell'_{{\rm J/\psi},i}|\mu, s\cdot\sigma_{\ell,i}) \tag{3.21}$$

for a given dimuon i. The different terms in eq. 3.21 are:

1. $R(\ell_{{\rm J/\psi},i} - \ell'_{{\rm J/\psi},i}|\mu, s\cdot\sigma_{\ell,i})$ is the resolution function with mean μ and width $s\cdot\sigma_{\ell,i}$ (the resolution depends on $p_{\rm T}$ and y thus is different for each dimuon). $\sigma_{\ell,i}$ is the error on $\ell_{\rm J/\psi}$ estimated by the reconstruction algorithms, and s is a scale factor (close to 1) correcting this estimation[1]. For prompt J/ψ, we have $\ell'_{{\rm J/\psi},i} = 0$, so the resolution function can be determined with the prompt J/ψ MC sample, or from data as explained in Sec. 3.9.2. This function is convolved with $F^{\rm true}_{\rm Sig}(\ell'_{{\rm J/\psi},i})$ and $F^{\rm true}_{\rm Bkg}(\ell'_{{\rm J/\psi},i})$ to obtain the measured $F_{\rm Sig,Bkg}(\ell_{{\rm J/\psi},i})$ distributions that include detector resolution effects.

2. $F^{\rm true}_{\rm Sig}(\ell'_{\rm J/\psi})$ is given by the sum of prompt and nonprompt components:

$$F^{\rm true}_{\rm Sig}(\ell'_{\rm J/\psi}) = bF^{\rm true}_{\rm Nonprompt}(\ell'_{\rm J/\psi}) + (1-b)F^{\rm true}_{\rm Prompt}(\ell'_{\rm J/\psi}) \quad , \tag{3.22}$$

   where b is the fraction of J/ψ from b hadron decays. By definition, $F^{\rm true}_{\rm Prompt}(\ell'_{\rm J/\psi})$ is simply the Dirac distribution $\delta(0)$, while $F^{\rm true}_{\rm Nonprompt}(\ell'_{\rm J/\psi})$ is an exponential decay.

3. $F^{\rm true}_{\rm Bkg}(\ell'_{\rm J/\psi})$ is determined from fits on the data background $\ell_{\rm J/\psi}$ distributions. The background and signal distributions are unfolded as explained in Sec. 3.9.2.

More information about the parametrisation of the $\ell^{\rm 3D}_{\rm J/\psi}$ distribution is given in Section 3.9.2.
When **per-event-uncertainties are included**, we need to add so-called Punzi-terms [121] to account for distribution of the error on the lifetime, $\sigma_{\ell,i}$:

$$F^{\mathcal{P}}_{\rm Sig,Bkg}(\ell_{{\rm J/\psi},i}, \sigma_{\ell,i}) = F_{\rm Sig,Bkg}(\ell_{{\rm J/\psi},i}) \cdot \mathcal{P}_{\rm Sig,Bkg}(\sigma_{\ell,i}) \tag{3.23}$$

where $\mathcal{P}_{\rm Sig,Bkg}(\sigma_{\ell,i})$ is the probability distribution of $\sigma_{\ell,i}$ in signal or background.
The procedure to obtain the inputs needed for the 2D fits can be divided in two main parts, the invariant mass and pseudo-proper decay length parameterisations. These procedures are detailed in Sections 3.9.1 and 3.9.2 respectively. The final settings for the 2D fits and the results are given in Section 3.9.3

[1] If the estimated $\ell_{\rm J/\psi}$ errors are correct, the distribution of $(\ell_{\rm J/\psi}\text{-}\ \ell'_{\rm J/\psi})/\sigma_\ell$ would have width $s = 1$.

3.9.1 Invariant mass parameterisation

In this section, the procedure to obtain the $M_{Sig}(m_{\mu\mu})$ and $M_{Bkg}(m_{\mu\mu})$ invariant mass parameterisations in eq. 3.20 is explained in details.
The inclusive J/ψ yield, i.e. combined prompt and nonprompt, is extracted separately by 1D-fitting the invariant $\mu^+\mu^-$ mass spectra. The invariant mass fits are done in the region $2.6 < m_{\mu^+\mu^-} < 3.5$ GeV/c^2. These fits are unbinned maximum extended likelihood fits, performed using the RooFit [122] package. The J/ψ decay to muon pairs produces a narrow peak in the dimuon mass spectrum around $m_{\mu\mu} \approx 3.09$ GeV/c^2. Pairs of uncorrelated muons form a continuous $m_{\mu\mu}$ distribution called the combinatorial background. These pairs are the products of leptonic decays of kaons and pions, and semi-leptonic decays of heavy-flavor hadrons.

Invariant mass signal shape and parameters The best model describing the signal has been determined based on MC simulations. Many shapes were tested and the shape that gives the best χ^2 value for most of the bins was chosen as the nominal shape. The J/ψ nominal signal shape is defined by the weighted sum of two Crystal Ball functions $g_{2\mathrm{CB}}(m_{\mu^+\mu^-})$ $(f \cdot g_{\mathrm{CB}_1}(m_{\mu^+\mu^-}) + (1-f) \cdot g_{\mathrm{CB}_2}(m_{\mu^+\mu^-})$), with common mean m_0 and tail parameters α and n. The Crystal Ball shape, g_{CB}, is defined in eq. 3.24. The Crystal Ball function $g_{\mathrm{CB}}(m)$ combines a Gaussian core and a power-law tail with an exponent n to account for energy loss due to final-state photon radiation, and a parameter α which defines the transition between the Gaussian and the power-law functions,

$$g_{\mathrm{CB}}(m) = \begin{cases} \frac{N}{\sqrt{2\pi}\,\sigma_{\mathrm{CB}}} \exp\left(-\frac{(m-m_0)^2}{2\,\sigma_{\mathrm{CB}}^2}\right), & \text{for } \frac{m-m_0}{\sigma_{\mathrm{CB}}} > -\alpha; \\ \frac{N}{\sqrt{2\pi}\,\sigma_{\mathrm{CB}}} \left(\frac{n}{|\alpha|}\right)^n \exp\left(-\frac{|\alpha|^2}{2}\right) \left(\frac{n}{|\alpha|} - |\alpha| - \frac{m-m_0}{\sigma_{\mathrm{CB}}}\right)^{-n}, & \text{for } \frac{m-m_0}{\sigma_{\mathrm{CB}}} \leq -\alpha. \end{cases} \tag{3.24}$$

To have stable fits, some signal parameters are fixed to values extracted from the background-free simulation. The fits are performed using the MC samples in the same bins as data, and the signal parameters, mainly the tail parameters (and the ratio of sigmas in PbPb), are extracted. Fig. 3.27 shows the dependence of α and n on z in pp and PbPb.
Since α (and σ_2/σ_1 in PbPb) is shown to be independent of z in Fig. 3.27, its value is fixed to the z-integrated fit in data and is also used to extract the values of n from MC. n still shows a dependence on z as can be seen in Fig. 3.28 so the values in data are fixed to the corresponding bin in MC.
Since it was shown in previous charmonia anlyses [123] that n and α do not depend on p_{T}, the increase of n could be caused by the clustering of the photon emitted by the muons in the jet, which means that at high z, where the J/ψ mesons are more isolated, the probability of having an extra photon would be low.
During the fitting procedure in data the following parameters are left free: f (the weight of the components of the double CB), m_0 (the J/ψ mass), σ_{CB}, $\sigma_{\mathrm{CB}_2}/\sigma_{\mathrm{CB}_1}$ (in pp) and $N_{\mathrm{J}/\psi}$ (the J/ψ yield). All other parameters are constrained or fixed to values from the simulation, as explained above. Alternative fitting procedures have been tried for the systematic uncertainty computation (see Sec. 3.10.1).

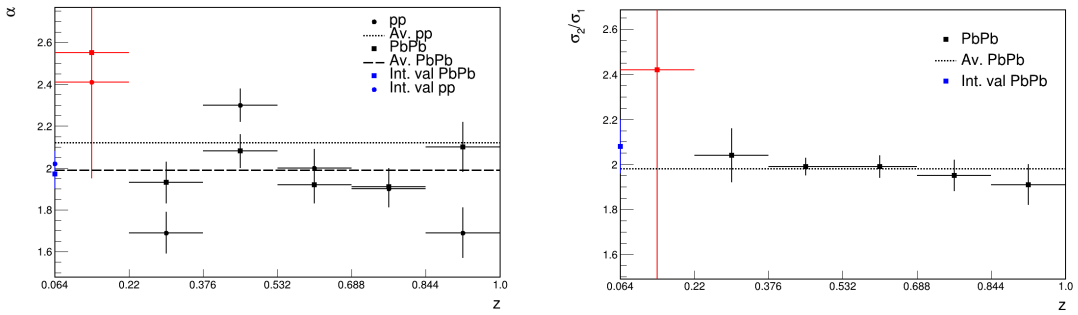

Figure 3.27: Evolution of α (left), the ratio of sigmas (right) as a function of z in the rapidity range $|y| < 2.4$, obtained from J/ψ fits in MC. The values obtained in the z-average (dashed lines) over the different bins and z-integrated (blue points) values are also reported.

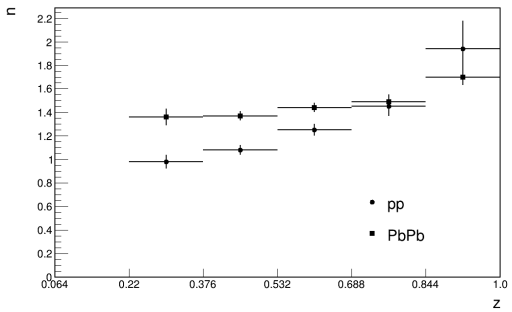

Figure 3.28: Evolution of n as a function of z in the rapidity range $|y| < 2.4$, obtained from J/ψ fits in MC with α (and σ_2/σ_1 in PbPb) fixed to the z-integrated fit values.

Invariant mass background shape The background is described by a Chebychev function [124] of order N, defined as:

$$M_{Bkg}(m_{\mu\mu}) = \sum_{i=0}^{N} c_i T_i(m_{\mu\mu}) \tag{3.25}$$

where T_i is a Chebyshev polynomial of order i and c_i is the corresponding fit parameter. The parameters c_i are uncorrelated with each other and the polynomials are determined using the following recurrence relation [125]:

$$T_{n+1}(m) = 2xT_n(m) - T_{n-1}(m), \text{ with : } T_0(m) = 1 \text{ and } T_1(m) = m \tag{3.26}$$

The order N is determined by performing a log-likelihood ratio (LLR) test separately for each analysis bin. This test compares the resulting minimized negative log-likelihood (NLL) of a fit with order N to the NLL with orders $N+1$ and $N+2$. The second one is necessary to account for the change between odd and even parity as the order is increased.
In particular, 2 times the differences between the NLL values from the fits with polynomials of orders N and $M > N$ follow a χ^2 distribution with $M - N$ degrees of freedom. The variables

$$\begin{aligned} \chi^2_{N\to N+1} &:= 2(NLL_N - NLL_{N+1}) \\ \chi^2_{N\to N+2} &:= 2(NLL_N - NLL_{N+2}) \end{aligned} \tag{3.27}$$

can thus be used to decide whether or not the increase of order allows for the function to fit the data *significantly* better, where significantly better is defined to be the case as long as the p-values $p(\chi^2 \geq \chi^2_{N\to N+1})$ and $p(\chi^2 \geq \chi^2_{N\to N+2})$ are less than 5%. An example of the results of the LLR tests in PbPb data for $0.688 < z < 0.844$ and $30< p_{\mathrm{T,jet}} <40$ GeV. The first order was chose for this bin since $p(\chi^2 \geq \chi^2_{1\to 2})$ and $p(\chi^2 \geq \chi^2_{1\to 3})$, shown in bold, are less than 5%.

M	NLL	p(N = 0)	p(N = 1)	p(N = 2)	p(N = 3)	p(N = 4)
0	-14080.36					
1	-14111.72	0.0%				
2	-14111.72	0.0%	**99.2**%			
3	-14111.74	0.0%	**100.0**%	98.1%		
4	-14111.95	0.0%	99.8%	97.8%	81.2%	
5	-14115.01	0.0%	58.2%	36.3%	16.3%	4.7%
6	-14115.04	0.0%	75.9%	57.8%	36.1%	18.7%

Table 3.2: Negative log-likelihoods for fits with Chebychev polynomials of orders 0-6 of PbPb data for $0.688 < z < 0.844$ and $30< p_{\mathrm{T,jet}} <40$ GeV. In addition the p-values of the LLR-test are listed. Tests with χ^2 probability for consecutive orders (M = N + 1 and M = N + 2) are higher than 5% are highlighted in bold.

The order of the best polynomial to describe the background in all z bins with $30< p_{\mathrm{T,jet}} <40$ GeV is shown in Fig. 3.29. The order of the polynomial does not exceed 2

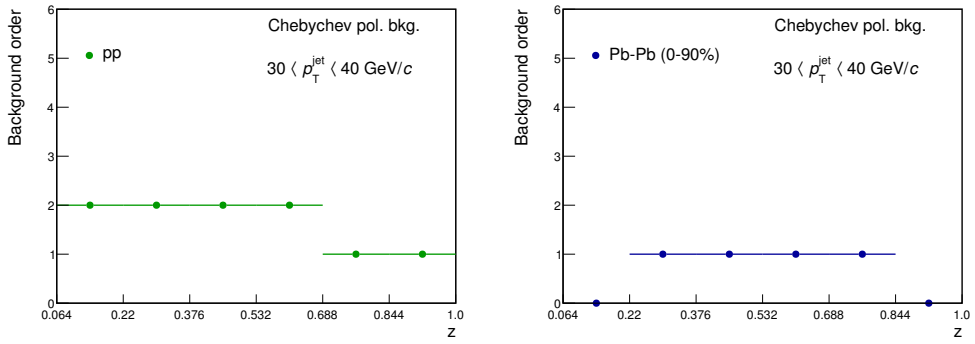

Figure 3.29: Results of the order chosen for the nominal (p-value $<$ 5 %) fits using the log-likelihood ratio test performed in each of the analysis bins as a function of z in pp (left) and PbPb in 0-90% centrality (right) for J/ψ in jets with $30 < p_T < 40$ GeV.

for all z bins in this jet p_T selection.
In Figure 3.30 an example of invariant mass fits in data, performed in two different analysis bins following the above procedure is given as an illustration.

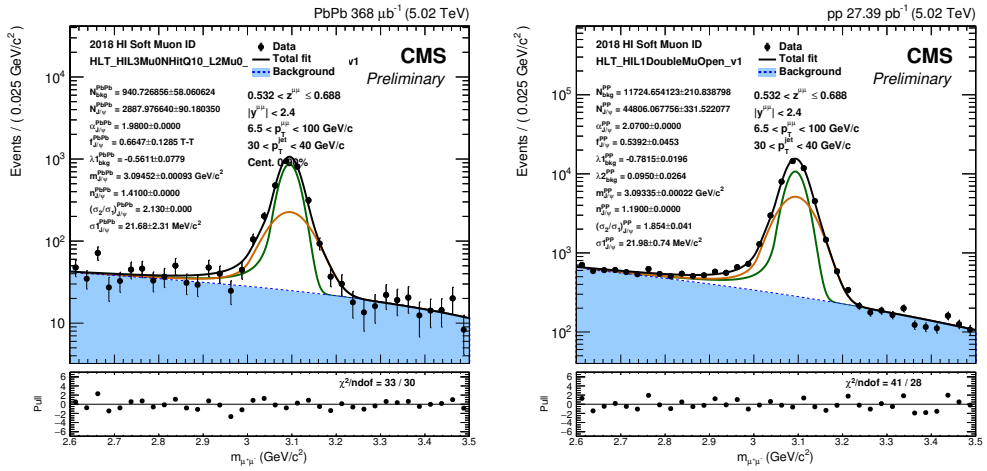

Figure 3.30: An example of nominal invariant mass fits for PbPb(left) and pp(right). The orange and green curves represent the two components of the double Crystal Ball function used for the fit.

3.9.2 Pseudo-proper decay length parameterisation

While the invariant mass doesn't distinguish between prompt and nonprompt J/ψ, the $\ell_{J/\psi}$ distribution does, making the parameterization of the pseudo-proper decay length more complicated than that of the invariant mass.
$F_{Sig}(\ell_{J/\psi})$ and $F_{Bkg}(\ell_{J/\psi})$ in eq. 3.20 are determined in four steps:

- Parameterization of $\ell_{J/\psi}$ error distribution.
- Parameterization of lifetime resolution.
- Parameterization of b hadron decay length.
- Parameterization of $\ell_{J/\psi}$ distribution of background dimuons.

The nominal procedure followed for each step is described in the corresponding sections below. The studies made to estimate systematic uncertainties for each step are detailed in Sec. 3.10.2.

Parameterization of $\ell_{J/\psi}$ error distribution

The uncertainty on to the $\ell_{J/\psi}$ distribution is computed as:

$$\sigma_\ell = \sqrt{m_{J/\psi}.\frac{\vec{p}_{\mu\mu}.S.\vec{p}_{\mu\mu}}{(p_{\mu\mu})^2}} \tag{3.28}$$

where S is the sum of the covariance matrices associated with the primary collision and dimuon vertex. The σ_ℓ distribution is described using a template histogram determined from data. Since the distributions for signal and background are different, they need to be disentangled from the total distribution when using the per-event error technique. Also, the σ_ℓ distributions are needed as input to obtain the parameterizations of the lifetime resolution and the $\ell_{J/\psi}$ distribution of background dimuons, in order to use the data σ_ℓ distribution both in data and MC fits. To separate the signal and background contributions we use the so-called ${}_s\mathcal{P}lot$ technique [126]. This is fully integrated in the *RooStats* [127] package.
This technique applies for a data sample of events described by a multidimensional space of discriminating variables, where there are several sources of events (i.e. signal and background, prompt and nonprompt particles...). The basic concept of the ${}_s\mathcal{P}lot$ technique consist of constructing the so-called ${}_s\mathcal{W}eights$ of the different categories of events, using the fit information on a discriminating variable. Then, the data sample can be weighted according to a given category of events, and plot the dataset for another variable.
In our specific case, we want to separate signal and background in the σ_ℓ distribution, so the discriminating variable is $m_{\mu\mu}$. The ${}_s\mathcal{W}eights$ of signal and background can be con-

structed from the mass PDFs obtained in Sec. 3.9.1 in the following way:

$$
\begin{aligned}
{}_s\mathcal{W}_{sig}(m_{\mu\mu}) &= \frac{V_{sig,bkg}\cdot M_{bkg}(m_{\mu\mu}) + V_{sig,sig}\cdot M_{sig}(m_{\mu\mu})}{N_{bkg}\cdot M_{bkg}(m_{\mu\mu}) + N_{sig}\cdot M_{sig}(m_{\mu\mu})} \\
{}_s\mathcal{W}_{bkg}(m_{\mu\mu}) &= \frac{V_{bkg,bkg}\cdot M_{bkg}(m_{\mu\mu}) + V_{bkg,sig}\cdot M_{sig}(m_{\mu\mu})}{N_{bkg}\cdot M_{bkg}(m_{\mu\mu}) + N_{sig}\cdot M_{sig}(m_{\mu\mu})}
\end{aligned}
\tag{3.29}
$$

where $M_{sig,bkg}(m_{\mu\mu})$ are the signal and background PDFs, $N_{sig,bkg}$ are the yields of each component and $V_{i,j}$ is the covariance matrix of the i^{th} and j^{th} sources of events (i,j = signal and background).
Each weight is applied to the dataset and then it is projected on the σ_ℓ to obtain the signal and background σ_ℓ distributions. Finally, the resulting distributions are converted into *RooHistPdf* to be used as Punzi-terms. In order to avoid zeros on the pdf in the low statistics high σ_ℓ region, a limit is imposed in the σ_ℓ value, which is propagated to the rest of the analysis. This limit is obtained from the σ_ℓ histogram and set at the value where the two following consecutive bins are empty. An example of such distributions for two analysis bins in pp is presented in Fig.3.31. The number of events lost due to the limitation in σ_ℓ is written in the legend, and it is always smaller than 0.6%.

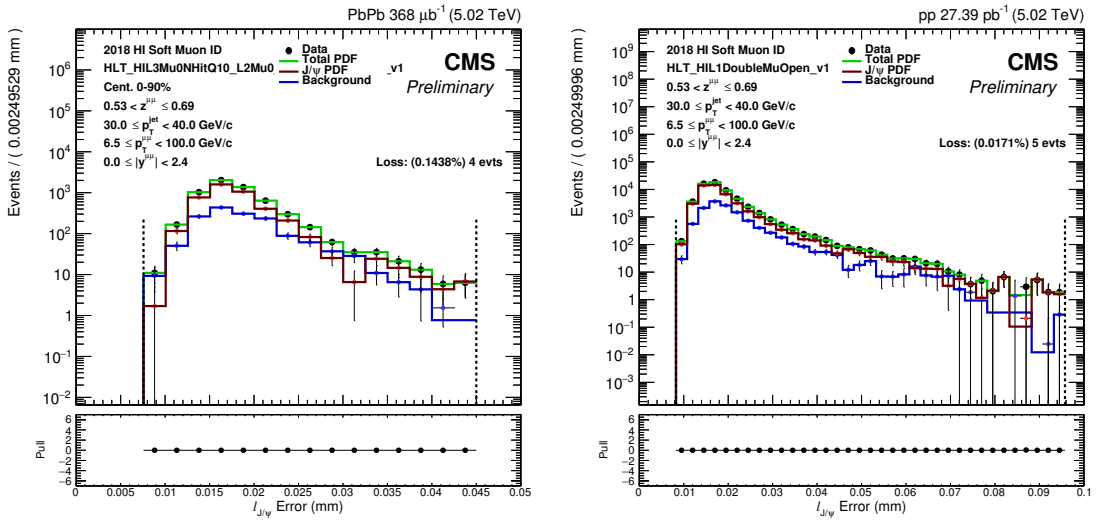

Figure 3.31: Two examples of σ_ℓ distributions for J/ψ and background and their corresponding PDFs in PbPb(left) and pp (right). The dashed lines represent the limits in the error distribution range, which is propagated to the rest of the analysis.

Parameterization of lifetime resolution

This section describes the procedure to obtain the parameterization of the lifetime resolution, $R_i(\ell_{J/\psi}|\mu, s_i\sigma_\ell)$ in eq.3.21. The prompt J/ψ $\ell_{J/\psi}$ distribution can be considered as the lifetime resolution. To obtain this distribution from data, the negative tail in the $\ell_{J/\psi}$ distribution is assumed to be mostly due to prompt J/ψ affected by resolution. The events from this negative tail are, therefore, used to determine the resolution. Among those events, some dimuons can be background dimuons, so the signal and background components are separated using the ${}_s\mathcal{P}lot$ technique, as in Sec. 3.9.2. The resulting distribution can be described by the weighted sum of several Gaussian functions. One of them describes most of the core ('narrow') region, while the other Gaussians take the tail ('wide') components. Studies performed in Ref. [123] show that the shape better describing the $\ell_{J/\psi}$ resolution is the weighted sum of three Gaussian functions, as in eq.3.30.

$$\begin{aligned} R_i(\ell_{J/\psi}|\mu, s\cdot\sigma_\ell) = &\left[f_{res}\cdot Gauss(\ell_{J/\psi}|\mu_1, s_1\cdot\sigma_\ell) + \right. \\ &\left.(1-f_{res})\cdot\left[f2_{res}\cdot Gauss(\ell_{J/\psi}|\mu_2, s_2\cdot\sigma_\ell) + (1-f2_{res})\cdot Gauss(\ell_{J/\psi}|\mu_3, s_3\cdot\sigma_\ell)\right]\right] \end{aligned} \tag{3.30}$$

where the f_{res} and $f2_{res}$ are the relative weights of the individual Gaussian functions on the total resolution pdf. The Gaussian components have separated sigmas. It has been checked that the mean of each component is always consistent with zero, and therefore they are fixed to zero in the fits. The Punzi-terms used in the resolution PDFs are templates of the σ_ℓ distributions obtained from real data in Sec. 3.9.2.
Examples for PbPb and pp resolution fits in data are given in Fig. 3.32. The dashed lines represent only the fitting range, and no restriction is imposed in the resolution values in the following steps of the analysis.

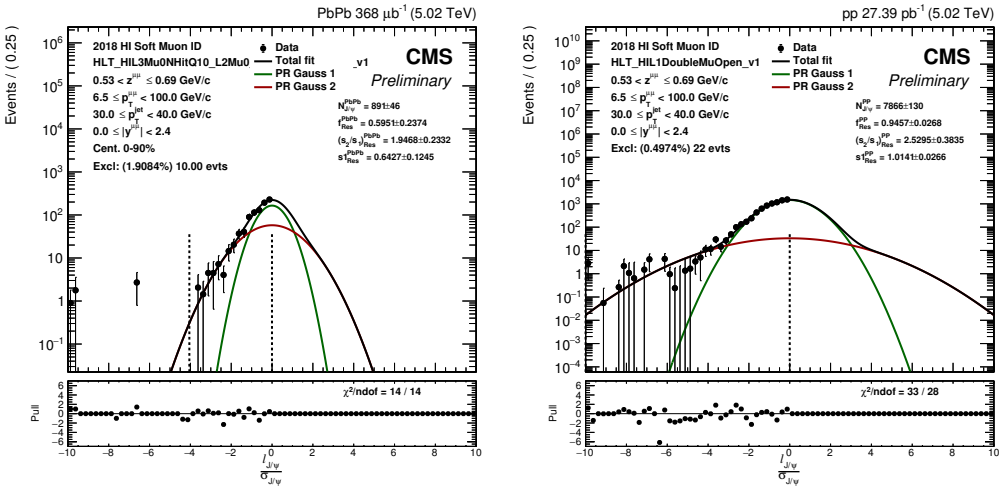

Figure 3.32: $\ell_{J/\psi}$ resolution distributions for J/ψ in data. The distributions are fitted with a weighted sum of two Gaussians. The dashed lines represent only the fitting range.

Parameterization of b hadron decay length

The b hadron decay length, or the true $\ell_{J/\psi}$, is a δ function in the case of prompt J/ψ. To parameterize the $F^{true}_{Sig}(\ell'_{J/\psi})$ in eq.3.22, the nonprompt component ($F^{true}_{Nonprompt}(\ell'_{J/\psi})$) is obtained form generated-level MC for nonprompt J/ψ. The distribution has an exponential behavior.

$$F^{true}_{NonPrompt}(\ell'_{J/\psi}) = e^{-|\lambda_{DSS}|\cdot\ell'_{J/\psi}} \tag{3.31}$$

where λ_{DSS} stands for the average decay length of b hadrons (Single Sided Decay). Examples of $F^{true}_{NonPrompt}(\ell'_{J/\psi})$ fits are shown in Fig.3.33 for pp and PbPb events.
The decay parameter results obtained from these fits, are used to initialise the parameter of the average lifetime of nonprompt J/ψ PDF in the 2D fits on data.

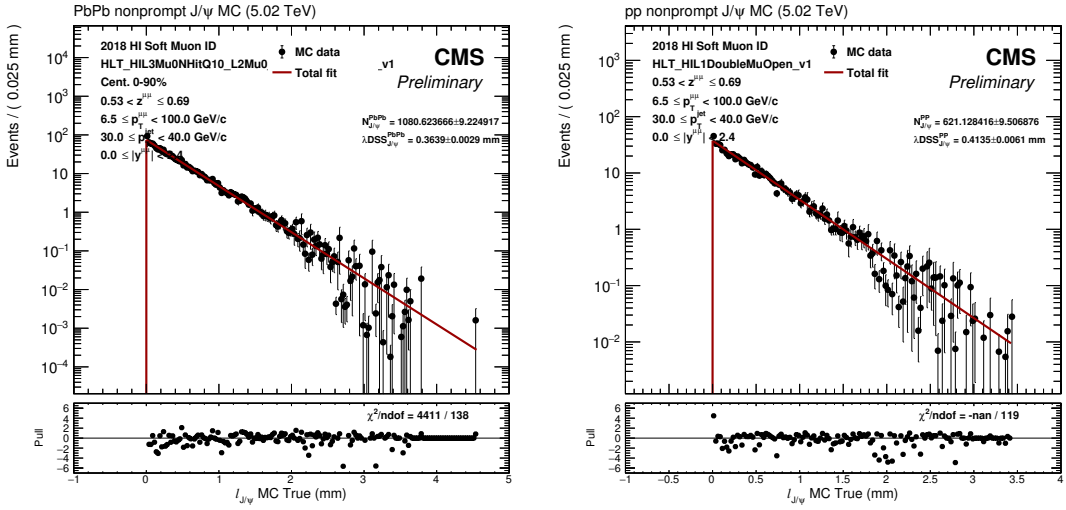

Figure 3.33: $F_{NonPrompt}(\ell'_{J/\psi})$ distributions in PbPb (left) and pp (right) events.

Parameterization of $\ell_{J/\psi}$ distribution of background dimuons

The last step before the 2D-fitting is to obtain the parameterization of the decay length distributions of background dimuons, $F^{true}_{Bkg}(\ell'_{J/\psi})$ in eq.3.21. In order to use the full background statistics for the parameterization we use the ${}_s\mathcal{P}lot$ technique in Sec. 3.9.2 to obtain a background dataset. The same limit on the maximum and minimum σ_ℓ used for the σ_ℓ parameterization is imposed here. The "nonprompt" (there is no actual physical notion of prompt and nonprompt for background) component of $F^{true}_{Bkg}(\ell'_{J/\psi})$ is described by a combination of a single-sided decay, a flipped single-sided decay, and a double-sided decay functions, while the "prompt" component is described by a Dirac delta function:

$$\begin{aligned} F^{true}_{Bkg}(\ell'_{J/\psi}) \;=\; & b_{bkg}\cdot[\, f_{DLIV}\cdot(\, f_{DFSS}\cdot e^{-|\lambda_{DSS}|\cdot\ell'_{J/\psi}} \\ & +(1-f_{DFSS})\cdot e^{|\lambda_{DF}|\cdot\ell'_{J/\psi}}\,) + (1-f_{DLIV})\cdot e^{-|\lambda_{DDS}\cdot\ell'_{J/\psi}|}\,] \\ & +(1-b_{bkg})\cdot\delta(\ell'_{J/\psi}) \end{aligned} \tag{3.32}$$

where b_{bkg} represents the background "nonprompt fraction". This function is convolved with the resolution functions obtained in Sec. 3.9.2 to fit the background reconstructed $\ell_{J/\psi}$ distributions in data. All the resolution parameters are fixed to those obtained in data fits in Sec. 3.9.2. Examples of these background $\ell_{J/\psi}$ fits can be seen in Fig. 3.34 for pp and PbPb data.

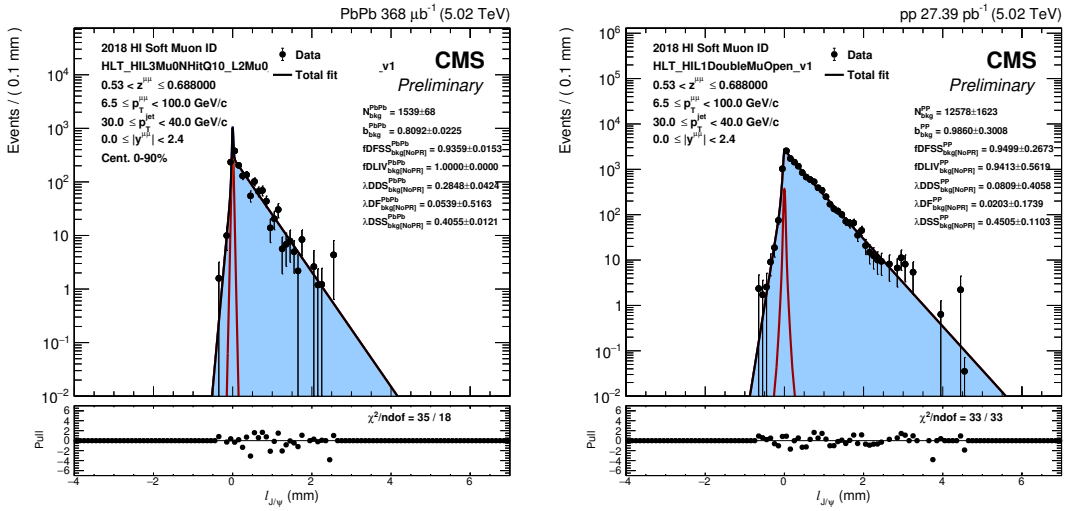

Figure 3.34: $F_{Bkg}(\ell_{J/\psi})$ distribution for PbPb (left) and pp (right).

3.9.3 Bidimensional fitting of invariant mass and pseudo-proper decay length

All the components are now ready for the bidimensional fitting procedure of the invariant mass and pseudo-proper decay length. The different pieces are plugged in the 2D fits as follows:

- From the invariant mass parameterizations in Sec. 3.9.1 all the signal and background parameters are fixed, except the number of inclusive J/ψ mesons, $N_{J/\psi}$, and the number of background dimuons, N_{bkg}, which are left as free, but constrained, parameters in the fits.
- All the parameters of the resolution function obtained are Sec. 3.9.2, are fixed from fits on the data sample.
- The parameters of the $\ell_{J/\psi}$ background fits obtained in Sec. 3.9.2 are all fixed in the 2D fits.
- The exponential decay parameters of the b hadron decay obtained from fits of the nonprompt MC sample in Sec. 3.9.2 are used as initial parameters in the fit, and they are left free.
- The b fraction ($b_{J/\psi}$ in the plots) is a free parameter in the 2D fits.

An example of the invariant mass and $\ell_{J/\psi}$ projections of 2D-fits in pp and PbPb can be seen in Fig. 3.35. The corresponding 2D PDFs are presented in Fig. 3.36.
Finally, the number of prompt and nonprompt J/ψ mesons used for the results are simply computed as:

$$\begin{aligned} N^{J/\psi}_{\text{prompt}} &= (1 - f_b) \cdot N^{J/\psi} \quad , \\ N^{J/\psi}_{\text{nonprompt}} &= f_b \cdot N^{J/\psi} \end{aligned} \tag{3.33}$$

To compute the statistical uncertainties of the prompt and nonprompt results, the correlation of the nonprompt fraction and the number of extracted inclusive J/ψ is taken into account.

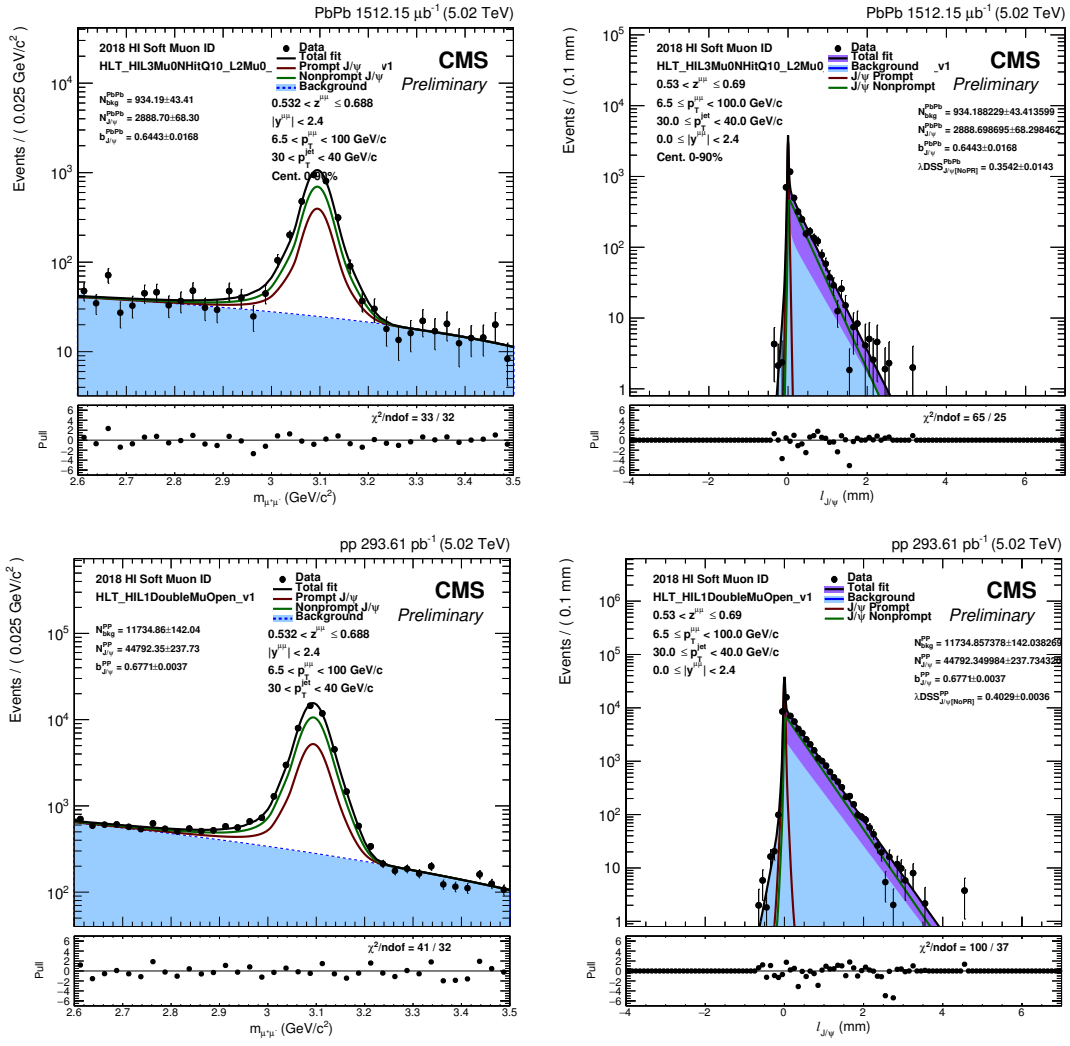

Figure 3.35: Invariant mass and $\ell_{J/\psi}$ projections of bidimensional fit of $\ell_{J/\psi}$ and invariant mass distributions for two given analysis bins.

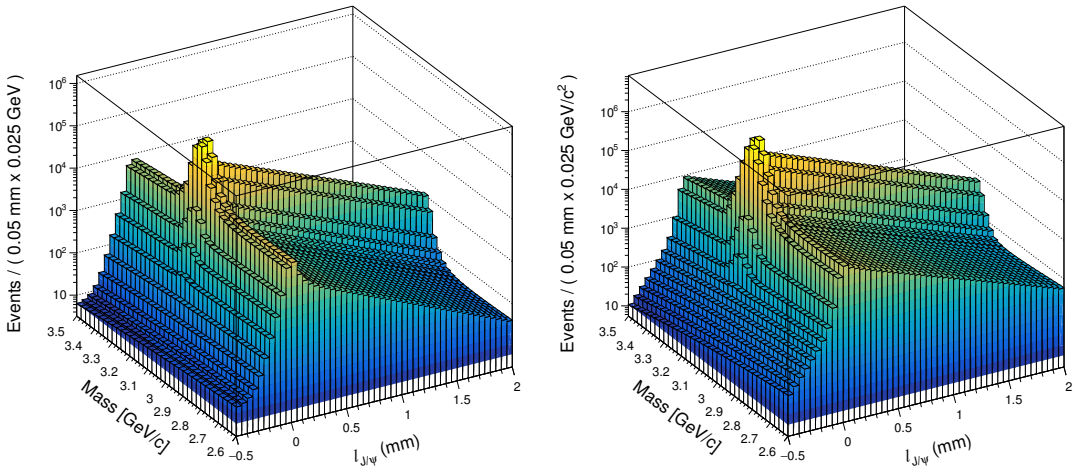

Figure 3.36: A bidimensional PDF of $\ell_{J/\psi}$ and invariant mass for a z bin in PbPb.

3.10 J/ψ signal extraction systematic uncertainties

This section describes the sources of systematic uncertainty related to the bidimensional fitting procedure to extract the prompt and nonprompt J/ψ yields. The uncertainties arise from the parametrization of the invariant mass and the pseudo-proper decay length.

3.10.1 Invariant mass parameterisation uncertainty

The variations to determine the systematic uncertainties on the different ingredients of the invariant mass parameterization are the following:
On the signal side:

- Variation of signal parameters for the nominal shape (double Crystal Ball): fits on data are performed by leaving free the parameters that were fixed from MC in the nominal fits one by one. See details in Sec. 3.10.1.
- Variation of the signal shape: use a Crystal Ball plus a Gaussian function as signal shape instead of the double Crystal Ball function.

On the background side:

- Variation of the fitting range. Use 2.6-3.4 instead of 2.6-3.5.
- Use an exponential of Chebychev polynomials instead of the Chebychev polynomials for the background parameterization.

In the cases where several variations are made for the same item listed above, the maximum deviation from the nominal value of the prompt and nonprompt J/ψ yields obtained with these variations is taken as systematic uncertainty for each source. Finally, the uncertainties from the different sources are added in quadrature.
The different tests performed for the determination of the systematic uncertainties are discussed in detail in the following subsections.

Variation of signal parameters

The CB tail parameters are fixed to the MC valued in the nominal data fits. This is also the case for the ratio of the two CB widths in PbPb. In order to estimate the uncertainty of the signal parameters from MC, the invariant mass distributions are refitted in data leaving the fixed parameters free one by one, with the rest fixed like the nominal case. Figure 3.37 shows an example of the invariant mass fits with the double Crystal Ball function in data, performed in two different analysis bins with α fixed for both pp (right) and PbPb (left) and σ_2/σ_1 fixed only in PbPb. n is left free in these fits.

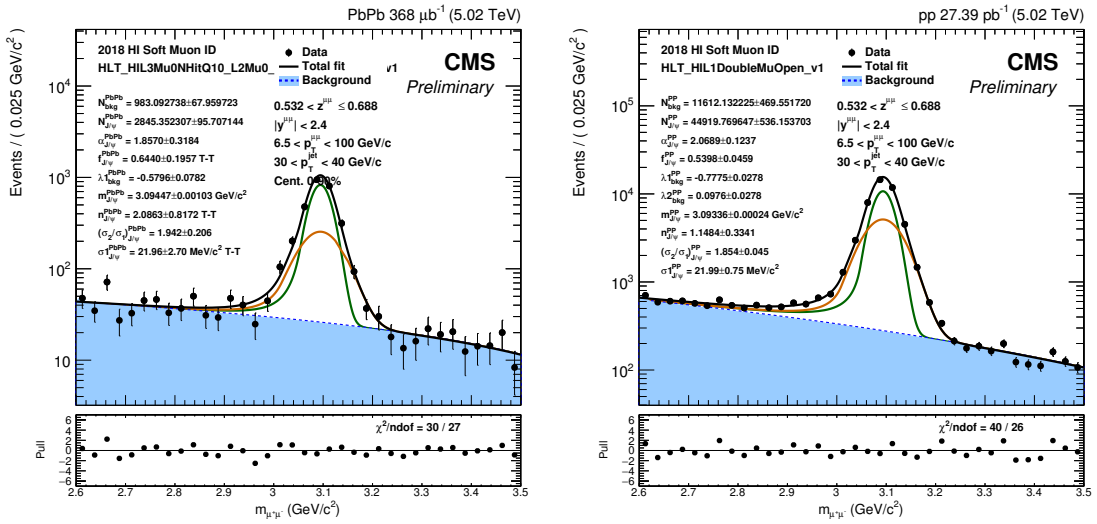

Figure 3.37: Examples of invariant mass constrained fits for in pp and PbPb data.

Variation of signal shape

For this variation, a Crystal Ball plus a Gaussian function are used instead of the double Crystal Ball function:

$$g_{\mathrm{CBG}}(m_{\mu^+\mu^-})(f \cdot g_{\mathrm{CB}}(m_{\mu^+\mu^-}) + (1-f) \cdot g_{\mathrm{G}}(m_{\mu^+\mu^-}) \tag{3.34}$$

where g_{CB} is the Crystal Ball shape defined in Eq. 3.24 and g_{G} is just a Gaussian shape. The signal parameters of the Crystal Ball plus Gaussian shape are determined from MC fits in the same way as for the double Crystal Ball shape.
In this case, the tail parameters α and n are fixed to the values found in MC, in addition to the ratio of sigmas in PbPb. The same nominal background functions obtained with the double Crystal Ball function are used, but the background parameters are left free.
Figure 3.38 shows an example of the invariant mass fits with the Crystal Ball plus Gaussian function in data, performed in two different analysis bins.
By using a new signal shape, a new set of α, n, and σ_2/σ_1 had to be derived following exactly the same way the nominal values were obtained.

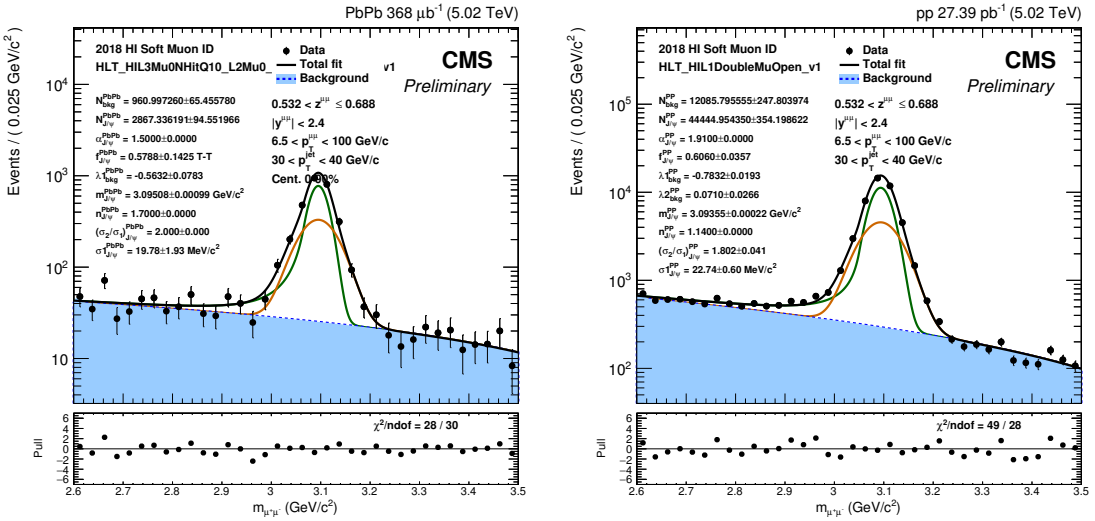

Figure 3.38: Example of invariant mass fits with the Crystal Ball plus Gaussian function in pp and PbPb data.

Variation of invariant mass fitting range

In order to estimate how the background parameterization (and hence the extracted number of J/ψ) is affected by the choice of the invariant mass range, the fitting range is varied from 2.6-3.5 GeV/c^2 to 2.6-3.4 GeV/c^2. The order of the Chebychev polynomial function used to parametrize the background is the same as the one used for the nominal fits.
In Figure 3.39 an example of the invariant mass fits with the reduced invariant mass range in data, performed in two different analysis bins, is given.

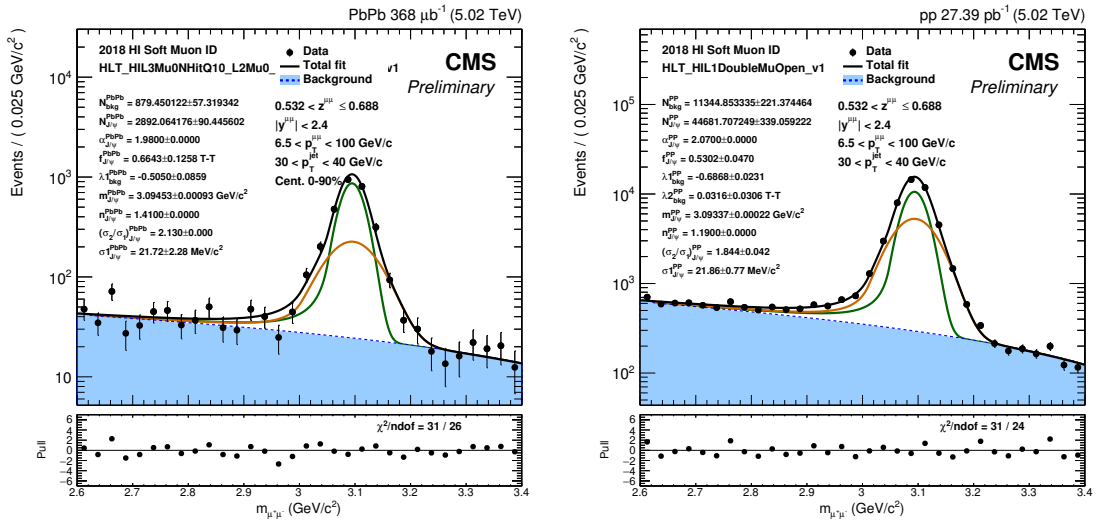

Figure 3.39: Example of invariant mass fits with reduced mass range in pp and PbPb data.

Variation of background shape

The second systematic variation for the background parameterization is on the choice of the background shape itself. In this case, the functional form of the background shape is changed from a Chebychev polynomial to an exponential of a Chebychev polynomial given as:

$$M_{Bkg}(m_{\mu\mu}) = \exp\left[\sum_{i=0}^{N} c_i T_i(m_{\mu\mu})\right] \tag{3.35}$$

where T_i is a Chebyshev polynomial of order i and c_i is the corresponding fit parameter. The polynomials follow the same recurrence relation [125] as the nominal case:

$$T_{n+1}(m) = 2xT_n(m) - T_{n-1}(m), \text{ with : } T_0(m) = 1 \text{ and } T_1(m) = m \tag{3.36}$$

The fits are also performed using orders 0-6 for the polynomial in the exponential, and the LLR test is applied with 5% as p-value in order to determine the best order for each analysis bin.
In Figure 3.40 an example of the invariant mass fits using the exponential of Chebychev polynomials for the background, performed in two different analysis bins is shown.

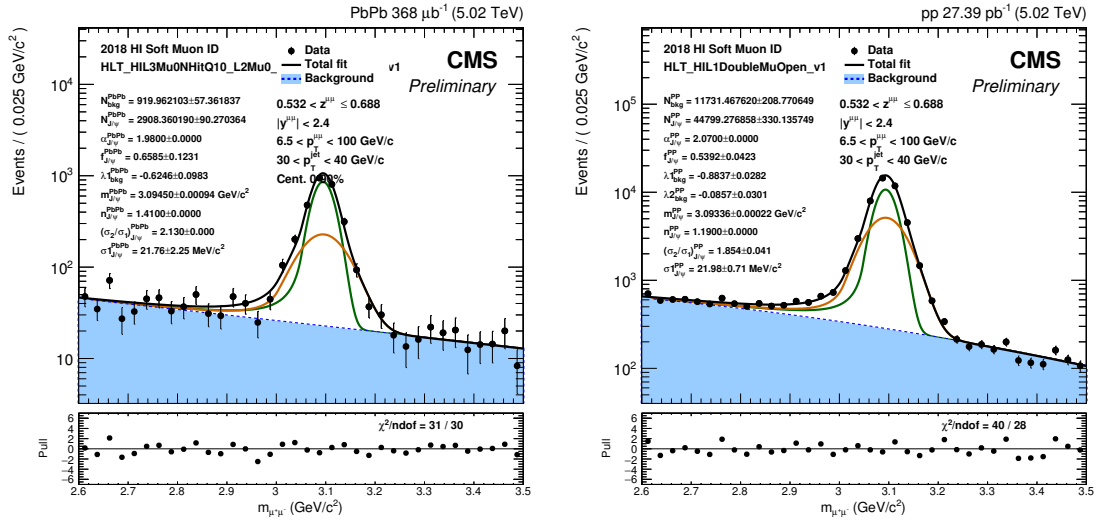

Figure 3.40: Example of invariant mass fits using the exponential of Chebychev polynomials for the background in pp and PbPb data.

3.10.2 Pseudo-proper decay length parameterisation uncertainty

The systematic uncertainties on the pseudo-proper decay length parameterization come from the four different steps as follows:

- On the error distributions side: Replace the nominal signal and background σ_ℓ templates in the 2D fits with the template of the total σ_ℓ distribution.
- On the resolution side: Use the $\ell_{J/\psi}$ resolution from prompt MC instead of data
- On the b hadron decay length side: Make a template of the nonprompt MC reconstructed $\ell_{J/\psi}$ distribution instead of the one side decay function convolved with the resolution function.
- On the background distributions side: Make a template of the distribution instead of the fit.

The σ_ℓ variation (first bullet) is simply taking the total distribution for the $\ell_{J/\psi}$ error (shown in green in Fig. 3.31 in Section 3.9.2) instead of the signal (red) and background (blue) distributions disentangled using the ${}_s\mathcal{P}lot$. The rest of the variations for the systematic uncertainties are discussed in details the following subsections.

Systematics on $\ell_{J/\psi}$ resolution

In order to estimate the systematic uncertainty due to the parameterization of the $\ell_{J/\psi}$ resolution, we obtain the resolution from prompt J/ψ MC (It was shown in [123] that the nonprompt MC samples were not appropriated for this). The $\ell_{J/\psi}$ resolution can be directly determined by fitting the prompt J/ψ MC sample since the true $\ell_{J/\psi}$ value is zero. The resulting distributions are then fitted with the weighted sum of two Gaussian functions as for the case of the nominal resolution fits in data. The Punzi-terms used in the resolution PDFs are templates of the σ_ℓ distributions obtained from real data in Sec. 3.9.2. In Fig. 3.41 we give two examples of the $\ell_{J/\psi}$ resolution parameterisation for pp MC events.

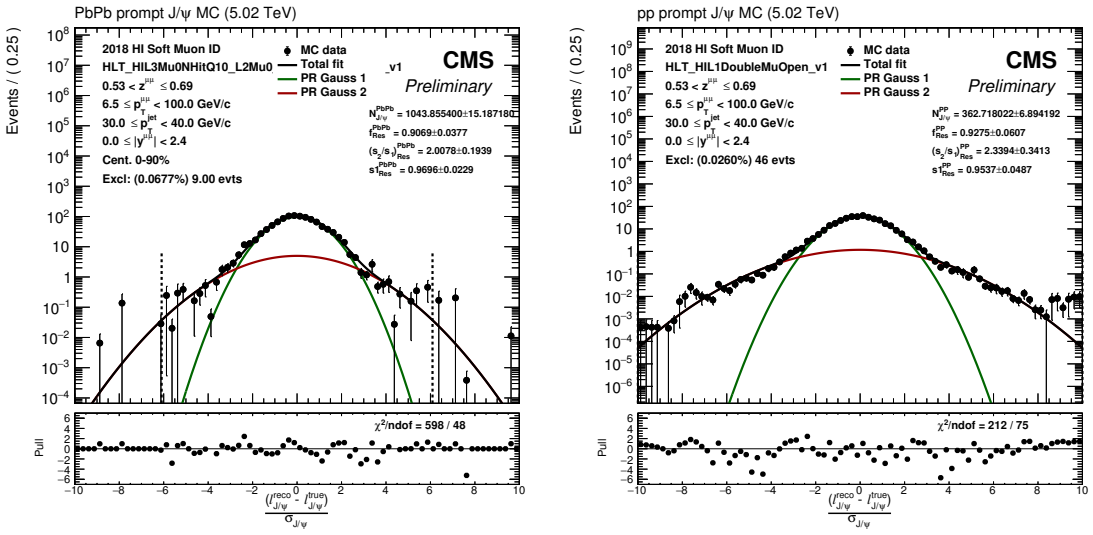

Figure 3.41: $\ell_{J/\psi}$ resolution distributions for prompt J/ψ MC sample. The distributions are fitted with a weighted sum of two Gaussians. The dashed lines represent only the fitting range.

Systematics on b hadron decay parameterisation

In this case instead of using the convolution of the resolution function with the exponential decay function initialized with the nonprompt J/ψ MC value of the b decay length, a template of the reconstructed $\ell_{J/\psi}$ distribution in nonprompt J/ψ MC is used in the 2D fitting procedure. The templates are made using RooKeysPdf [128]. These PDF templates have to be multiplied by the corresponding data $\ell_{J/\psi}$ error distribution (Punzi terms) in the 2D fits. Examples of these templates are given in Fig. 3.42.

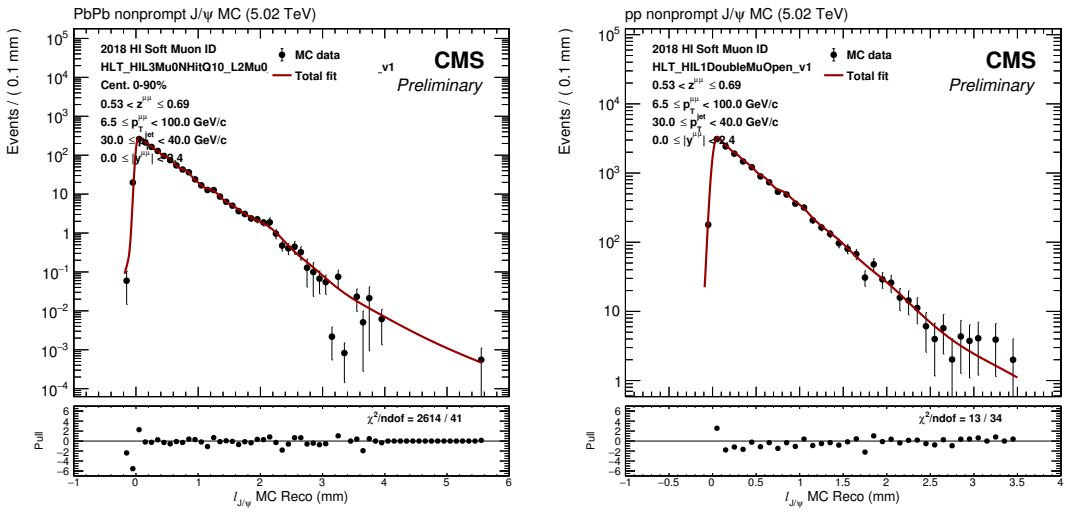

Figure 3.42: Templates of $F_{NonPrompt}(\ell_{J/\psi})$ distributions in pp and PbPb MC.

Systematics on $\ell_{J/\psi}$ background distribution

To take into account miss-modeling of the $\ell_{J/\psi}$ background distribution in Sec. 3.9.2 due to the choice of the fitting function, templates of the background distribution are created and used in the 2D fits instead of the PDFs. The $_s\mathcal{P}lot$ technique is used to unfold the signal and background $\ell_{J/\psi}$ distributions, which allows using all the background events. The smoothen templates are created with RooKeysPdf [128] technique. In Fig. 3.43 examples of these templates in pp and PbPb data are shown.

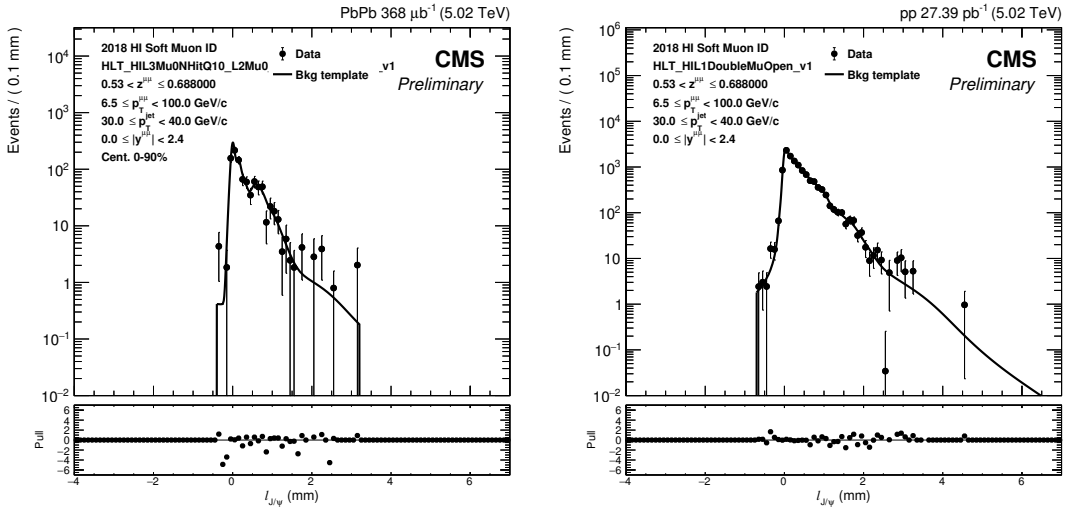

Figure 3.43: Templates of the $\ell_{J/\psi}$ background distributions in pp and PbPb data.

3.10.3 Summary plots of systematic uncertainties on bidimensional fits

The systematic uncertainty of a given bin, corresponding to a given source or piece of the 2D fits, is computed as the maximum difference between the nominal result and the systematic variations for that source. The individual sources are the invariant mass background, invariant mass signal, $\ell_{J/\psi}$ error, $\ell_{J/\psi}$ resolution, $\ell_{J/\psi}$ background, and the pseudo proper decay length. The total uncertainty for each bin is computed as the quadratic sum of the uncertainties of the different sources.
In Fig. 3.44, the systematic uncertainties on the number of extracted prompt J/ψ mesons due to the bidimensional fitting procedure for the different z bins for jets with $30 < p_T < 40$ GeV, the values of the uncertainties are given relative to the nominal value in the nominal z bins.

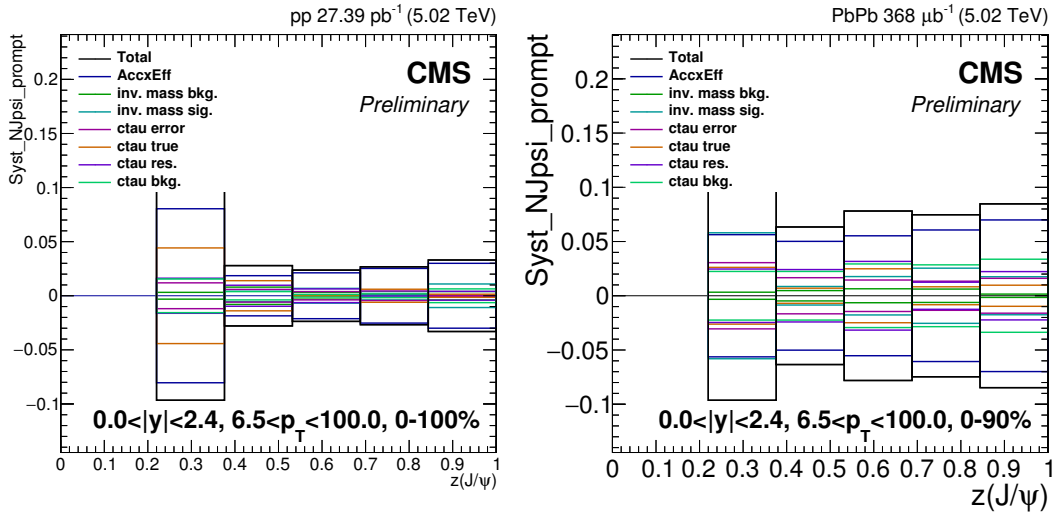

Figure 3.44: Systematic uncertainties of the 2D fits for the number of extracted prompt J/ψ mesons in pp (left) and PbPb (right) collisions as a function of z for jets with $30 < p_T < 40$ GeV. The values of the uncertainties are given relative to the nominal value.

Fig. 3.44 shows also the total uncertainty of the J/ψ corrections, labeled as "Acc$\times$Eff" in the plots. The following section will explain the individual components of this uncertainty.

3.10.4 J/ψ correction uncertainties

The impact of the acceptance and efficiency variations on the signal extraction in data is estimated using the MC samples. The procedure consists of applying the nominal 2D acceptance and efficiency correction to the reconstructed MC samples, in the same way as it is done on data, and simply counting the number of J/ψ in each analysis bin, $N_{J/\psi}^{\text{nominal}}$. Then the variations of the corrections are applied one-by-one to obtain different acceptance and efficiency corrections. These corrections are applied to the reconstructed MC, and the number of J/ψ in each analysis bin is counted, $N_{J/\psi}^{\text{variation}}$. The uncertainty is then estimated from the difference $N_{J/\psi}^{\text{nominal}} - N_{J/\psi}^{\text{variation}}$.
The statistical uncertainty on the efficiency (due to limited MC statistics) is taken into account by performing 100 toy Monte Carlo on both corrections. The efficiency value in each (p_T,y) bin in the acceptance corrections is randomly re-generated using a binomial function where $(\varepsilon)^{new} = \frac{binomial(N_{tot},(\varepsilon))}{N_{tot}}$. The value of the uncertainty is the RMS of the results obtained from the 100 toy MC (std dev. ($N_{J/\psi}^{\text{nominal}} - N_{J/\psi}^{\text{toy};i}$; $i = 1..100$)). The same procedure is done for the acceptance.
Since this binomial function takes the number of events in the denominator of the efficiency as input, it does not handle well-weighted corrections. This is why it's better to refrain from using big weights e.g. N_{coll} weights. Otherwise, this uncertainty would be artificially negligible. As mentioned in Section. 3.7, unweighted corrections are used for the nominal results and the weighted efficiencies are used as systematic uncertainties for the mismodeling of the corrections.
The statistical and systematic uncertainties of the T&P scale factors are taken into account in the estimation of J/ψ acceptance$\times$efficiency uncertainties. The T&P efficiencies explained in Section. 3.7.3 are the global reconstruction and trigger+ID efficiencies in pp, and the tracking, muon identification, and trigger efficiencies for PbPb. For each source of efficiency, an uncertainty is assigned due to the data and MC statistics and labeled, another is assigned to the signal and background shapes and the mass range of the T&P fits, labeled "systematic" in the following. In the case of PbPb, an additional uncertainty was assigned by changing the trigger used for tag selection.
The total systematic uncertainty related to the T&P scale factors is the quadratic sum of the statistical and systematic components described above.
Finally, the total systematic uncertainty on the acceptance$\times$efficiency is the quadratic sum of the uncertainty related to the T&P scale factors, the statistical uncertainty on the acceptance$\times$efficiency, and the uncertainty from the mismodelling of the kinematic distributions in MC. In Fig.3.45 a summary plot of the different sources of uncertainties and the total systematic uncertainty on the acceptance$\times$efficiency is presented for pp and PbPb in the nominal z bins.

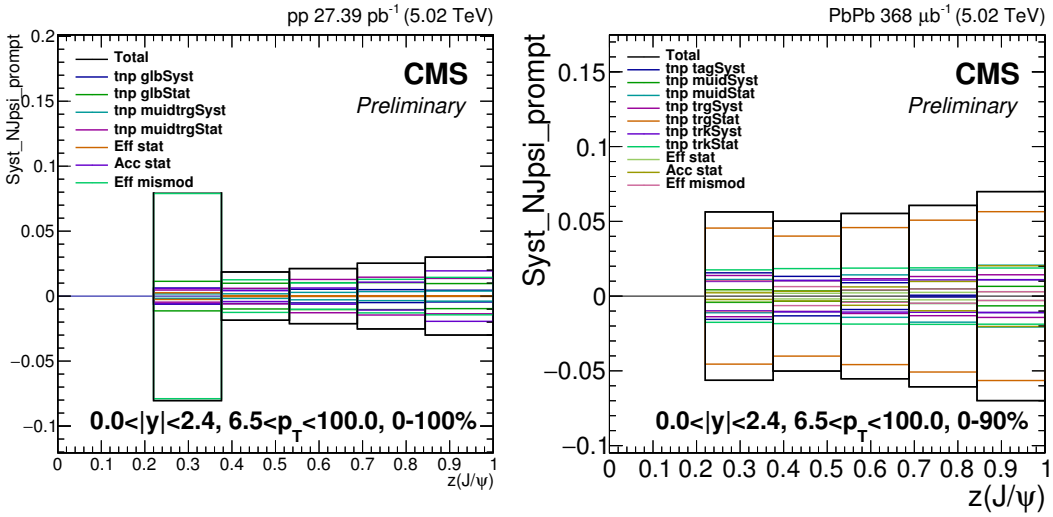

Figure 3.45: Systematic uncertainties of acceptance×efficiency on prompt J/ψ mesons in pp (left) and PbPb (right) rapidity. The values of the uncertainties are given relative to the nominal value.

3.11 Raw quarkonia yields

This section presents the "raw" J/ψ yields, meaning that the yields are fully corrected for acceptance and efficiency but still not corrected for bin migration between the z and jet p_{T} bins. The uncertainties presented are correspondingly only those of the quarkonia yield extraction: 2D fits and acceptance$\times$efficiency. The unfolded results are presented in Chapter 4.

3.11.1 Raw prompt J/ψ yields

Figure 3.46 shows the yield of prompt J/ψ as a function of z in pp and PbPb collisions, for the nominal jet p_{T} range of 30 – 40 GeV. The distributions show a radically different shape in pp and PbPb, which is due to the large combinatorial underlying event in the latter case. A J/ψ of modest p_{T} is very likely to overlap with a jet in this range, leading to a large peak at low z. One also expects a corresponding depletion of J/ψ at large values of z.

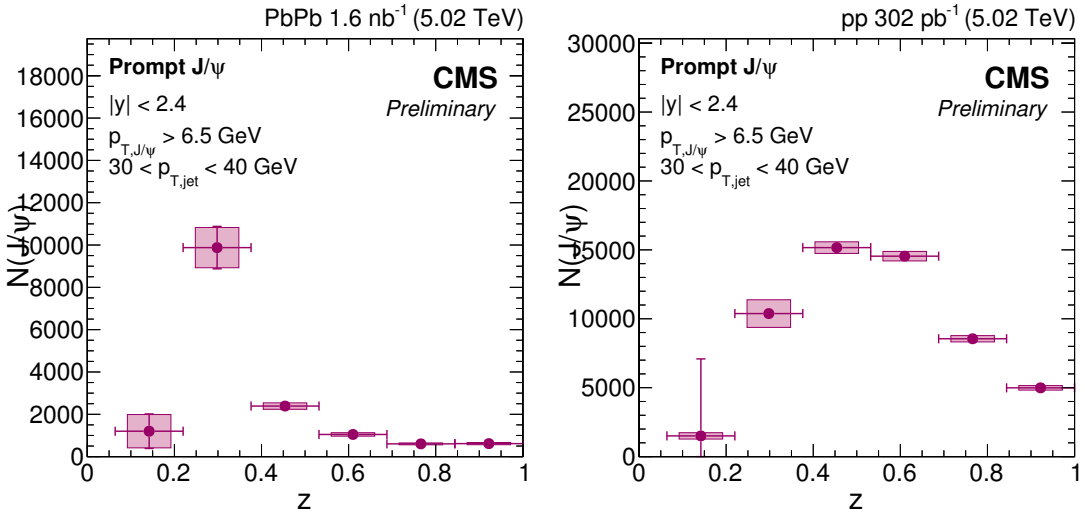

Figure 3.46: Prompt J/ψ yields, as a function of z, in pp collisions (left) and PbPb collisions (right), for the nominal jet p_{T} range of 30 – 40 GeV.

3.11.2 Unfolding input

In order to unfold the effect of bin migration from finite jet resolution, we need to measure the z distribution in lower and higher ranges of jet p_{T}. We measured in three "underflow" ranges of jet p_{T}, 6.5 – 10, 10 – 20, and 20 – 30 GeV, as well as two overflow ranges, 40 – 50 and 50 – 60 GeV.

Low-$p_{\mathrm{T,jet}}$

Figure 3.47 shows the yield of prompt J/ψ as a function of z for in pp and PbPb collisions in three jet $p_{\mathrm{T,jet}}$ underflow bins: $6.5 < p_{\mathrm{T,jet}} < 10$, $10 < p_{\mathrm{T,jet}} < 20$ and $20 < p_{\mathrm{T,jet}} < 30$ GeV.

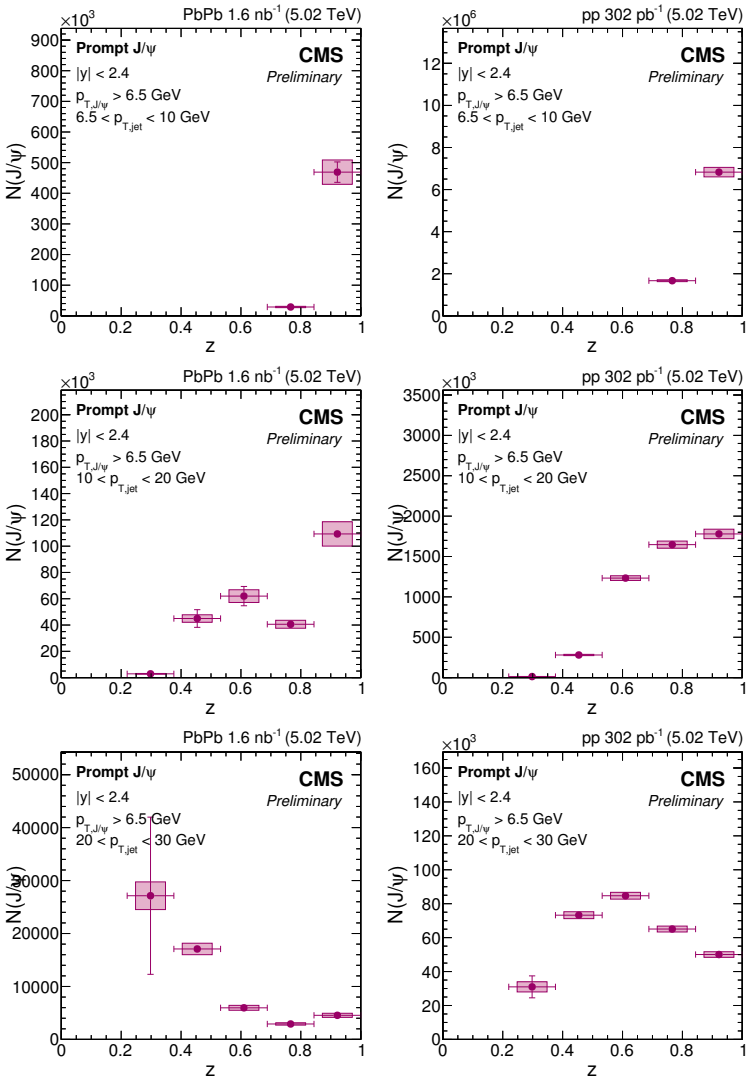

Figure 3.47: Prompt J/ψ yield as a function of z in pp and PbPb collisions for $6.5 < p_{\mathrm{T,jet}} < 10$, $10 < p_{\mathrm{T,jet}} < 20$ and $20 < p_{\mathrm{T,jet}} < 30$ GeV.

High-$p_{T,jet}$

Figure 3.48 shows the yield of prompt J/ψ as a function of z for in pp and PbPb collisions in the two jet p_T overflow bins: $40 < p_{T,jet} < 50$ and $50 < p_{T,jet} < 60$ GeV.

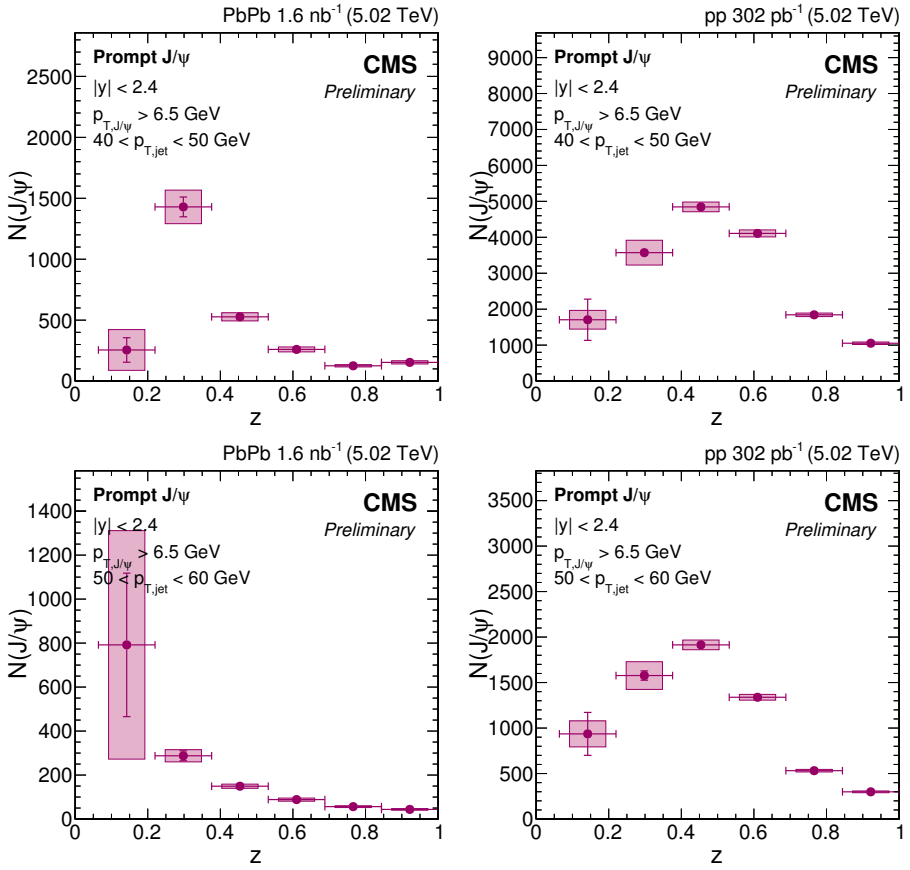

Figure 3.48: Prompt J/ψ yield as a function of z in pp and PbPb collisions for $40 < p_{T,jet} < 50$ and $50 < p_{T,jet} < 60$ GeV.

3.12 Jet energy resolution

The p_T resolution of jets is relatively poor compared to many other physics objects like muons. The resolution needs to be well described by the simulation to avoid any biases that can affect the steeply falling spectra of jets. An example of the jet resolution in simulation, defined as $R_{ptcl} = p_T/p_{T,ptcl}$ with ptcl indicating particle or generator level, is shown in Fig. 3.49 for inclusive jets at 8 TeV [118]. The shape of the distribution is Gaus-

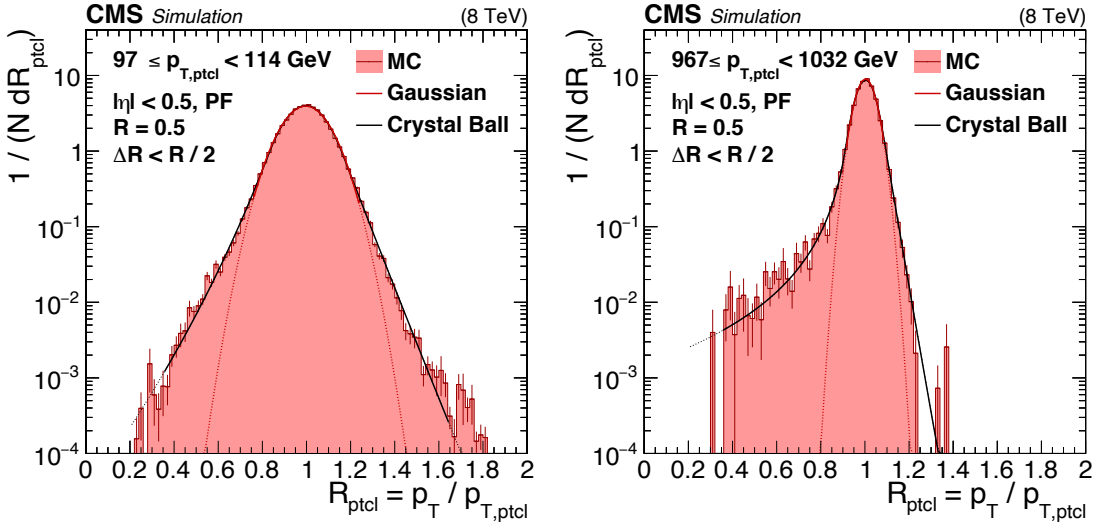

Figure 3.49: Jet p_T resolution distributions in the barrel for two bins of jet p_T [118].

sian with nongaussian low-response tails caused by rare detector effects such as inactive areas of the ECAL and to high-p_T particles punching through the HCAL. The distribution is well modeled with a double-sided Crystal Ball function.
Jet Energy Resolution (JER) is defined as the σ of the Gaussian function of $p_{T,reco}/p_{T,ptcl}$ and is well described by the so-called CSN parametrization as a function of p_T:

$$\sigma(p_T)/p_T = \sqrt{C^2 + S^2/p_T + N^2/p_T^2}. \tag{3.37}$$

where N is a noise term that comes from PU and UE, S is for stochastic fluctuations that scale as 1/E, and C is a constant term with no p_T dependence. The noise term N is negligible compared to the two other contributions in the low pileup pp data used in this analysis (S dominates in the p_T range studied here). In PbPb collisions, simulations are well-described by centrality independent S and C values, with N values that depend on centrality. The CSN parameters are extracted from fits in MC of JER as function of $p_{T,ptcl}$ as shown in Fig. 3.50. The C and S values derived from simulation are 0.06 and 0.98 ($\sqrt{\text{GeV}}$).
The p_T resolution is known to be somewhat different in data and simulation. To take this

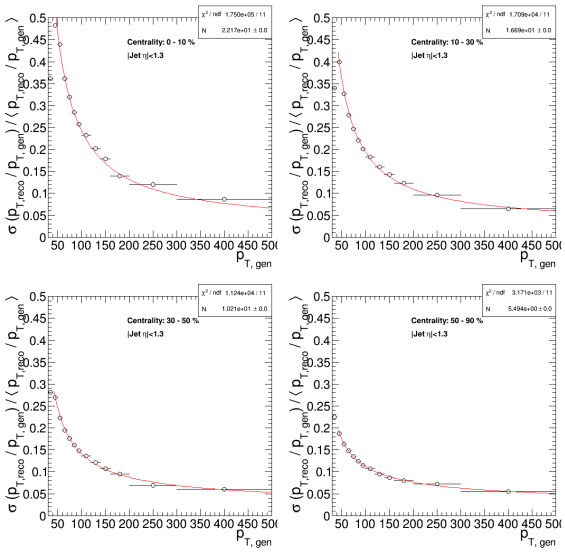

Figure 3.50: The extraction of the CSN parameters via fits to the jet energy resolution for different centrality selections.

into account, the centrality-independent and dependent contributions are treated separately. For the centrality independent contributions, data/MC scale factors are derived from high luminosity pp data in 2017 and 2018 and γ+jet and dijet MC samples with a T&P method. In 2017 they are evaluated from data run that directly preceded the pp reference run used in the analysis. No scale factors are provided for individual running periods, rather the uncertainties cover the variation of detector performance over the year. For the 2018 data, the scale factors are provided for the pp data run just preceding the PbPb run, although these scale factors are not very different from the ones provided that are averaged over the entire year. The measurement of the JER is an extension of the methods used for measuring JES, but looking at the width of the response distribution instead of the mean. In γ+jet events the σ_{JER} can be expressed as:

$$\sigma_{\text{JER}} \equiv \frac{\sigma_{p_{\text{T}}}}{p_{\text{T}}} = \sigma_{\mathcal{B}} k_{rad} \ominus \sigma_{\text{PLI}} \ominus \sigma_{\gamma} \tag{3.38}$$

with $\ominus$ indicating quadratic subtraction. In the first term, $\sigma_{\mathcal{B}}$ is the σ of $p_{\text{T,jet}}/p_{\text{T,fl}}$ and $k_{\mathcal{B}} = \sigma_{\mathcal{B}}(\text{secondary jet activity})/\text{œ}_{\mathcal{B}}$. The other terms are the Particle Level Imbalance effects of the UE and OOC (out-of-cone activity) and σ_{γ} is the resolution of the photon. In dijet events, the JER appears once for each jet. The dijet asymmetry is defined as:

$$\mathcal{A} = \frac{p_{\text{T,1st jet}} - p_{\text{T,2nd jet}}}{p_{\text{T,1st jet}} + p_{\text{T,2nd jet}}} \tag{3.39}$$

If both jets are in the same region and share the same JER:

$$\sigma_{\text{JER}} = \sqrt{2}(\sigma_{\mathcal{A}} k_{rad} \ominus \sigma_{\text{PLI,dijet}}) \tag{3.40}$$

where $\sigma_{\text{PLI,dijet}}$ is the resolution of the asymmetry variable, built with the momenta of particle-level jets extrapolated to zero additional jet activity. It is related to the single jets PLI resolutions through $\sigma_{\text{PLI,dijet}} = 1/2(\sigma_{\text{PLI,tag}} \oplus \sigma_{\text{PLI,probe}})$. If one of the jets is central and the other is forward:

$$\sigma_{\text{JER,forward}} = 2\sigma_{\mathcal{A}} k_{rad} \ominus 2\sigma_{\text{PLI,central-forward}} \ominus \sigma_{\text{PLI,central}} \tag{3.41}$$

where $\sigma_{\text{PLI,central-forward}}$ is $\sigma_{\text{PLI,dijet}}$ determined exclusively for the combination of central and forward jets.
Fig. 3.51 shows the scale factors and the uncertainties as a function of η for 2018 data.

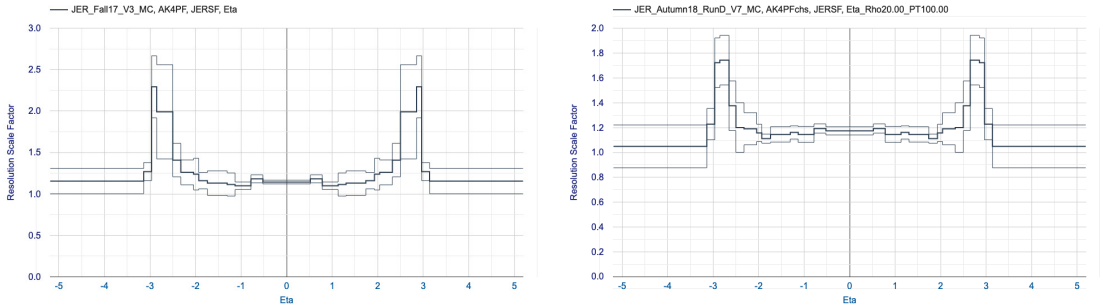

Figure 3.51: Data/MC scale factors as a function of η for pp (left) and PbPb (right). The thick line represents the nominal scale factors and the thin lines represent the uncertainties.

In practice, the MC values are smeared in the transfer matrix used in the unfolding, described in Section 3.13. The reconstructed value of jet p_{T} of the non-J/ψ part of the jet is smeared and reassigned by randomly sampling a Gaussian function. The centroid of the Gaussian is the original value of the reconstructed jet p_{T}. The width of the Gaussian is given by:

$$p_{\text{T,meas}} * \sqrt{C^2 + S^2/p_{\text{T,true}}} * \sqrt{\text{SF}^2 - 1}, \tag{3.42}$$

where $p_{\text{T,meas}}$ and $p_{\text{T,true}}$ are the measured and generator-level p_{T} values, respectively, for the non-J/ψ part of the jet. SF is the scale factor.
A simple toy MC study was used to check the validity of the smearing approach used in this analysis, shown if Fig. 3.52. The p_{T} of jets of 35 GeV is smeared by the CSN parameterization in Eq. 3.37, using two choices of $N = 0$ GeV and $N = 5$ GeV, to represent pp and PbPb, respectively. The exact value is immaterial for this test, $N = 5$ GeV was chosen purely for visibility on the final plots. The jet p_{T} values are smeared a second time inflating the C and S values by an arbitrary scale factor of 1.25. Finally, the jets are smeared according to the procedure used in this analysis. The jets are first smeared by the original factor (without the scale factor) and then additional smearing to the reconstructed jet p_{T} value is applied according to Eq. 3.42. The analysis procedure is found to reproduce the p_{T} distribution of jets with the resolution given by the data/MC scale factors.

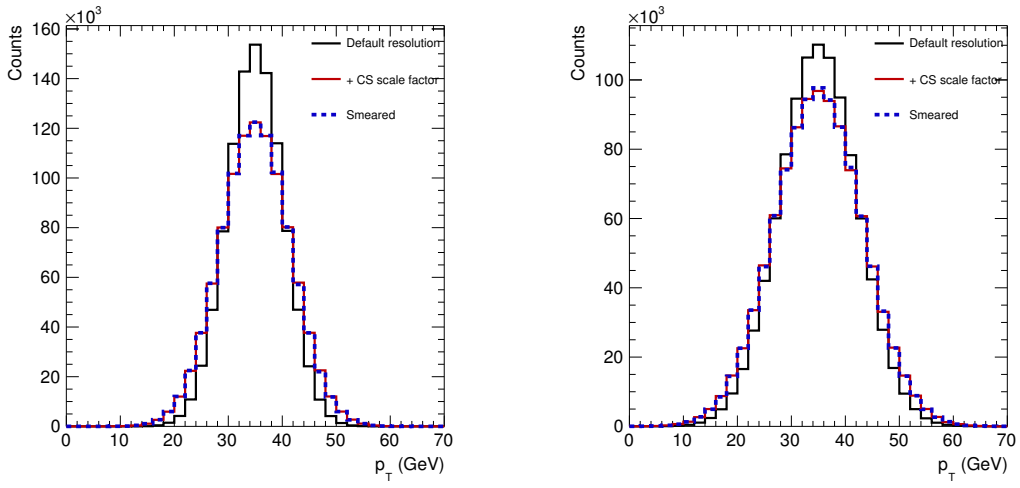

Figure 3.52: Smearing of the JER for jets of 35 GeV with $N = 0$ and $N = 5$. The smeared values are shown with the default C and S values (black line) and with an arbitrary scale factor (red line). The blue line shows the smearing according to the analysis procedure described in the text.

The uncertainty on the value is evaluated based on the random cone studies performed in Ref. [129]. The p_{T} density (ρ) evaluated in random cones was found to be overestimated in MC. Good agreement between data and MC was found by shifting the MC centrality definition by 4.5%, such that, e.g., one compares 0 – 10% data to 4.5 – 14.5% MC. A comparison of the underlying event energy density from random cones in data and simulation is shown in Fig. 3.53. The plots show that a variation by 1.5% in centrality up and down is sufficient to cover data-MC differences in the ρ distribution. We use these variations to the transfer matrix to assign an uncertainty on the jet resolution from the UE.

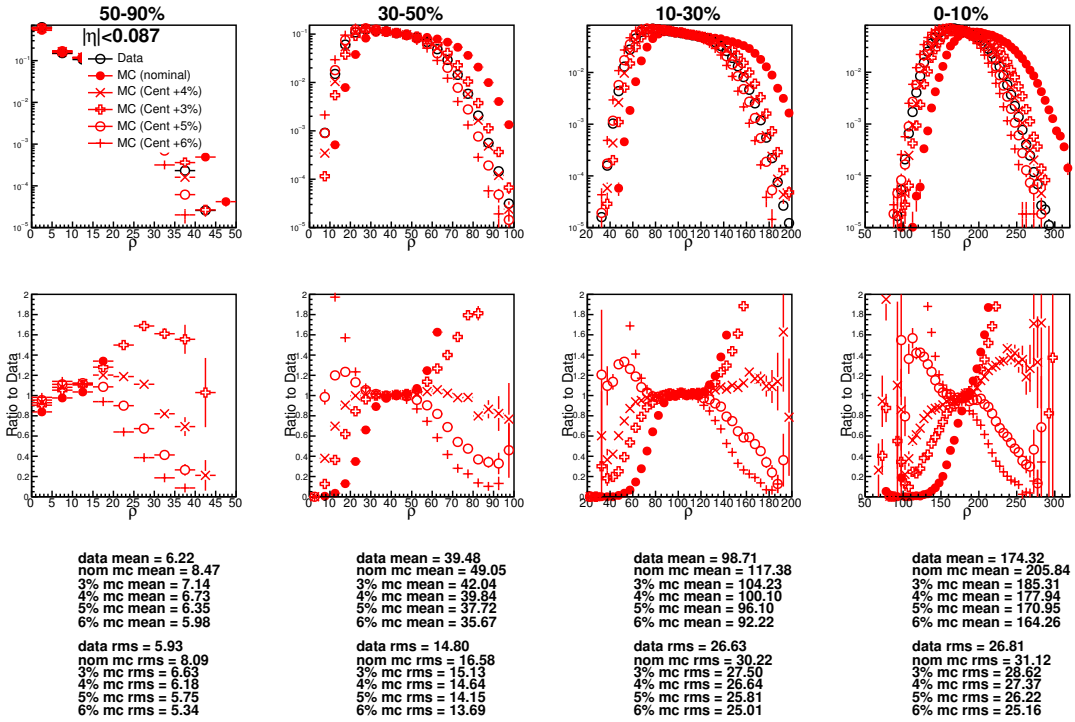

Figure 3.53: Underlying event density (ρ) from random cones in data and HYDJET simulation, for various centrality selections, in a central pseudorapidity region ($\eta < 0.087$). In addition to the default simulation, the simulation is shown shifted by 3,4,5 and 6% in centrality.

3.13 Unfolding bin migration effects

The p_T resolution of inclusive jets in the range where we perform our measurement (30 – 40 GeV), is around 15 – 20% in pp collisions and can reach around 50% in central PbPb collisions. The relatively wide resolution of jets, coupled with their steeply falling spectrum, causes substantial bin migration. The net effect is somewhat smaller on the z distribution than on the p_T spectrum of jets itself, as the fragmentation function scales logarithmically with jet p_T, whereas the yield decreases with p_T according to a power law. However, the effect is by no means negligible, especially in PbPb collisions. This is demonstrated in Fig. 3.54, which compares the generator-level and measured z distributions from prompt MC. The correction of resolution effects requires the application of an unfolding method.

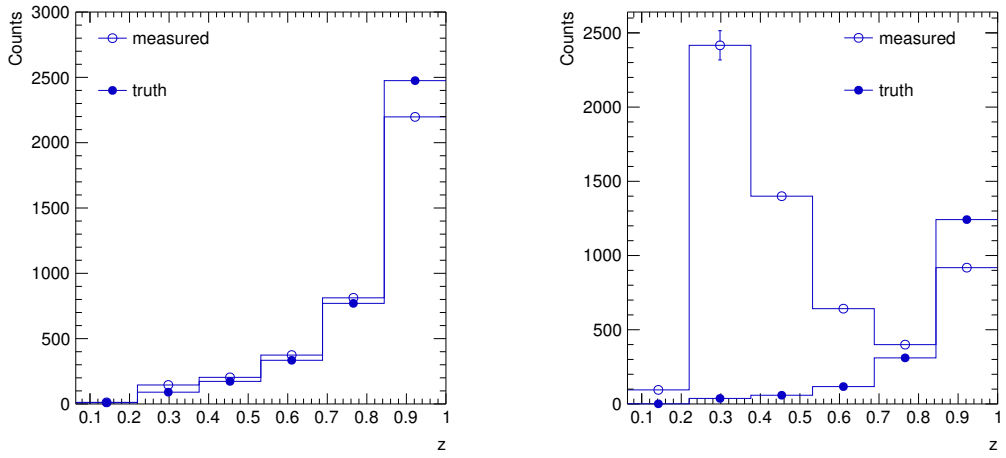

Figure 3.54: A comparison of the MC truth to the measured z distribution in pp (left) and PbPb collisions (right).

It is not sufficient to only correct for the resolution as a function of p_T. As discussed in Section 3.8, if one neglects the resolution of the J/ψ itself, the resolution is proportional to z. To take the dependence of the resolution on both p_T and z into account, the unfolding is done in two dimensions. A framework for doing 2D unfolding is available in the RooUnfold package [130]. The D'Agostini's iterative method [131] is used, which is initialized with a "prior" guess of the unfolded distributions.
As is standard, the transfer matrix, which describes the detector response to the signal of interest, is taken from MC. The transfer matrix encodes the relationship between the measured and truth (labeled "gen" here) values.
The transfer matrices for pp and PbPb are shown in Fig 3.55. The lower and upper limits of 6.5 and 60 GeV, respectively, were chosen such that 99% of jets with a gen p_T in the range of $30 < p_T < 40$GeV are in the measured range. This was tested in both prompt

and nonprompt PbPb MC. The depicted transfer matrices are normalized such that the sum over any gen bin, i.e., integrating over all measured bins, adds to unity. Hence this shows the probability of a given gen value ending up in any of the measured bins. For the case of 2D unfolding, the transfer matrix is a 4D histogram. In Ref. [132], it was found that to minimize finite bin size effects finer binning is required on the gen axes, compared to the measured ones. The number of bins is therefore increased by a factor of 5 for the gen jet p_{T} axis and a factor of 8 for the gen z axis.

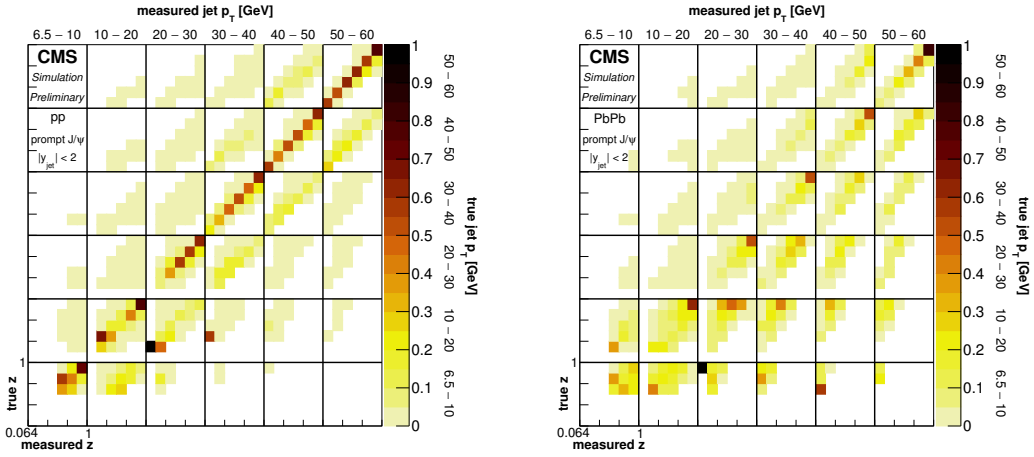

Figure 3.55: The 2D transfer matrix for bin migration in jet p_{T} in pp (left) and PbPb collisions (right).

The unfolding procedure used in this analysis follows closely that used by LHCb in Ref. [66]. By default, RooUnfold initializes the unfolding with the MC truth distribution as the prior. However, such a choice can easily lead to a biased result, particularly in the case when the MC truth is a poor representation of the data. Following LHCb, the unfolding instead starts with a prior which is flat in z, in order not to assume a shape that is peaked to large z, as in prompt MC, or peaked towards lower values, as in nonprompt MC. This is particularly important as the shape of the prompt MC does not reflect the shape in the prompt data. In the interactive method, the unfolded distribution at each iteration is then used as input to the next iteration. After performing a certain number of iterations, which is a tunable parameter, a new "super-iteration" is started. This means that the transfer matrix reverts to the original prior, except the z distribution is initialized to match the output of the previous super-iteration. The number of super iterations is a second tunable parameter. The strength of the regularization depends on both the number of iterations and super-iterations.
The first step was testing the unfolding machinery purely in MC. Using a self-same sample for the measured distribution and transfer matrix, the unfolding performs perfectly. A less trivial test is performed by splitting the same into two equal-sized statistically independent pieces. In this test, used to understand the qualitative features of the unfolding,

the number of iterations is fixed to three, and the behavior is studied as a function of the number of super-iterations. This choice of three iterations was inherited from the LHCb measurement, where it was found to give reasonable results for pp collisions. Fig. 3.56 shows the results of the unfolding for the pp and PbPb prompt J/ψ MC. The left panels show the distributions, while the right panels show the ratio of the unfolding output for selected super-iterations to the measured distributions. The success of the unfolding can be gauged by comparing these curves to the ratio of the truth to measured distributions, which is also shown. For the pp MC, the measured distribution is already relatively close to the truth one. After one super-iteration the unfolded result is quite close to the truth one, removing most of the bin migration effect. Further super-iterations actually degrade the performance, inducing an oscillatory behavior in the results.
Looking at the prompt MC in PbPb, the measured value is found to be quite far from the truth. The truth is peaked towards large z, i.e., the J/ψ in the MC are isolated. When superimposed on the large and fluctuating PbPb underlying event, these isolated J/ψ often appear at low z. The overall yield in the measured distribution is larger, as more jets tend to migrate into the nominal jet p_{T} bin, than out of it, due to the steeply falling jet p_{T} spectrum. The large peak at low z already disappears after a single super-iteration. However, one needs to go to a much larger number of super-iterations to recover the shape of the truth distribution. For illustration, we show the result of 98 and 99 super-iterations. The unfolding converges to a stable result, which is also the case for a large number of (super-) iterations in pp. The general features of the truth distribution are recovered, although the agreement is not perfect.
At this point, we realized that a more careful optimization of the regularization parameters is necessary. We considered that it might be useful to tune not only the number of super-iterations, but the number of standard iterations, as well. Further, we realized that the oscillatory behavior caused by under-regularization, as clearly observed in the pp MC test, should depend on the statistical precision of the measured sample. Therefore, we had better try to emulate the statistical precision of the data. To do so, we smeared each jet p_{T} and z bin in the measured distribution in MC according to the relative uncertainty from the same bin in data. We then ran the unfolding with several choices for the number of iterations per super-iteration. Figure 3.58 (left) shows the χ^2 between the measured and truth distributions for three choices of the number of iterations, 3, 5, 7, 10, and 20, as a function of the number of super-iterations. When computing the χ^2, only the statistical uncertainty of the truth is taken into account. For the initial choice of three iterations, the best agreement is achieved after 25 iterations, after which the performance degrades.
We also considered that the optimal choice of the regularization parameters could depend on the shape of the measured distribution. To test this hypothesis, we performed the unfolding on the nonprompt MC, where the z distribution looks very different. The true z distributions are shown in Fig. 3.57. The corresponding χ^2 scan is shown in the right panel of Figure 3.58. Here it appears that a larger number of iterations improves the performance. The best performance was achieved with 10 iterations. The best number of super-iterations was smaller for the prompt case, showing a shallow minimum of around 9.

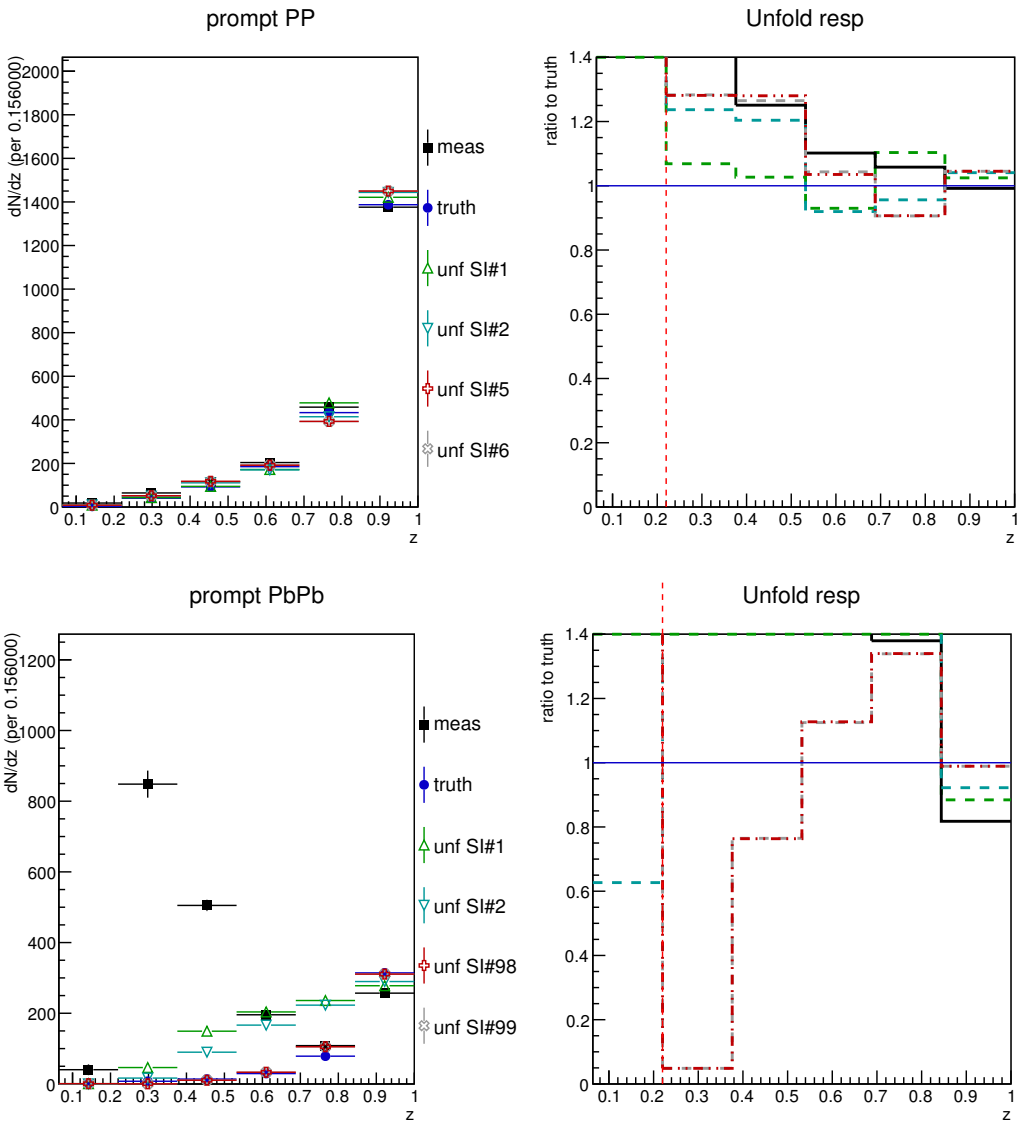

Figure 3.56: Closure test of the unfolding in MC for prompt J/ψ in pp (top) and PbPb (bottom) collisions. The left set of panels shows the truth, measured and unfolded z distribution after selected super-iterations, while the right shows the ratio of these to the true z distribution.

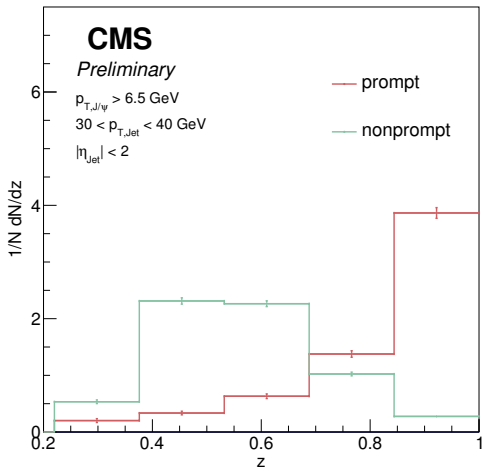

Figure 3.57: MC truth distributions of z in pp for prompt and nonprompt

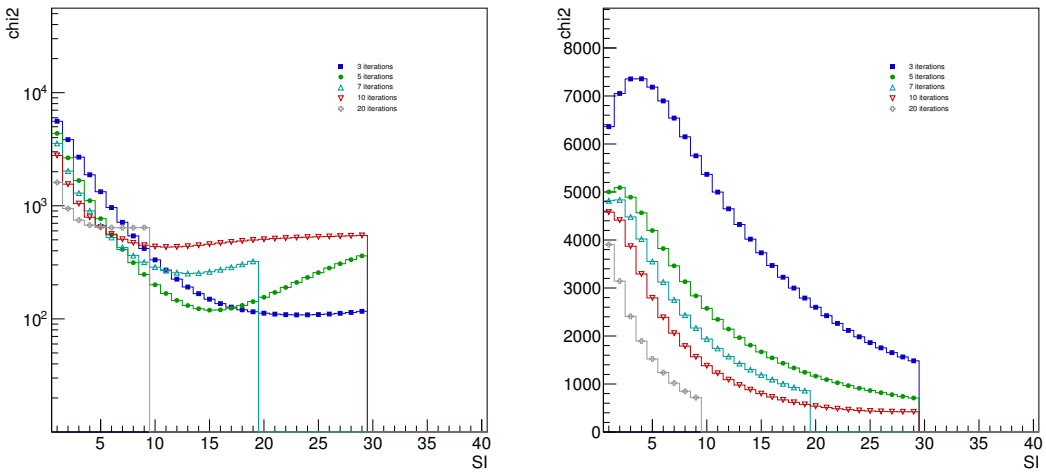

Figure 3.58: χ^2 of the unfolding in MC for prompt J/ψ in PbPb collisions for prompt (left) and nonprompt (right).

The z distributions for the best number of iterations (3 for prompt and 10 for nonprompt) are shown for several super-iterations, up to the best one (25 super-iterations), in Fig 3.59. For prompt MC, we see very good agreement between the unfolded and truth distribution for the best choice of regularization parameters. For the nonprompt case, although the main features of the truth distribution are still recovered, there is a somewhat poorer agreement between the unfolded and truth distributions. This may indicate that the best choice for regularization parameters obtained so far, may still be sub-optimal. We still plan to explore more choices for these parameters to see if better performance can be achieved.

A χ^2 scan was also performed for the pp MC. The best performance was found to be 3 iterations and 1 super-iteration in prompt MC and 10 iterations with 1 super-iteration for nonprompt MC. Fig. 3.60 shows the z distributions, using 3 and 10 iterations for prompt and nonprompt MC, respectively. The unfolded distributions compare reasonably well with the truth-ones for the curves corresponding to one super-iteration.

The same procedure is also done in two centrality ranges: 0–20% and 20–90%. The Closure tests for central PbPb collisions are shown in Fig 3.61. Where 2 iterations and 28 super-iterations were found to be the best option for prompt and 10 iterations and were chosen for nonprompt. The tests for the peripheral collisions are shown in Fig 3.62. 21 super-iterations of 2 iterations are chosen for prompt and 13 super-iterations of 10 iterations were chosen for nonprompt.

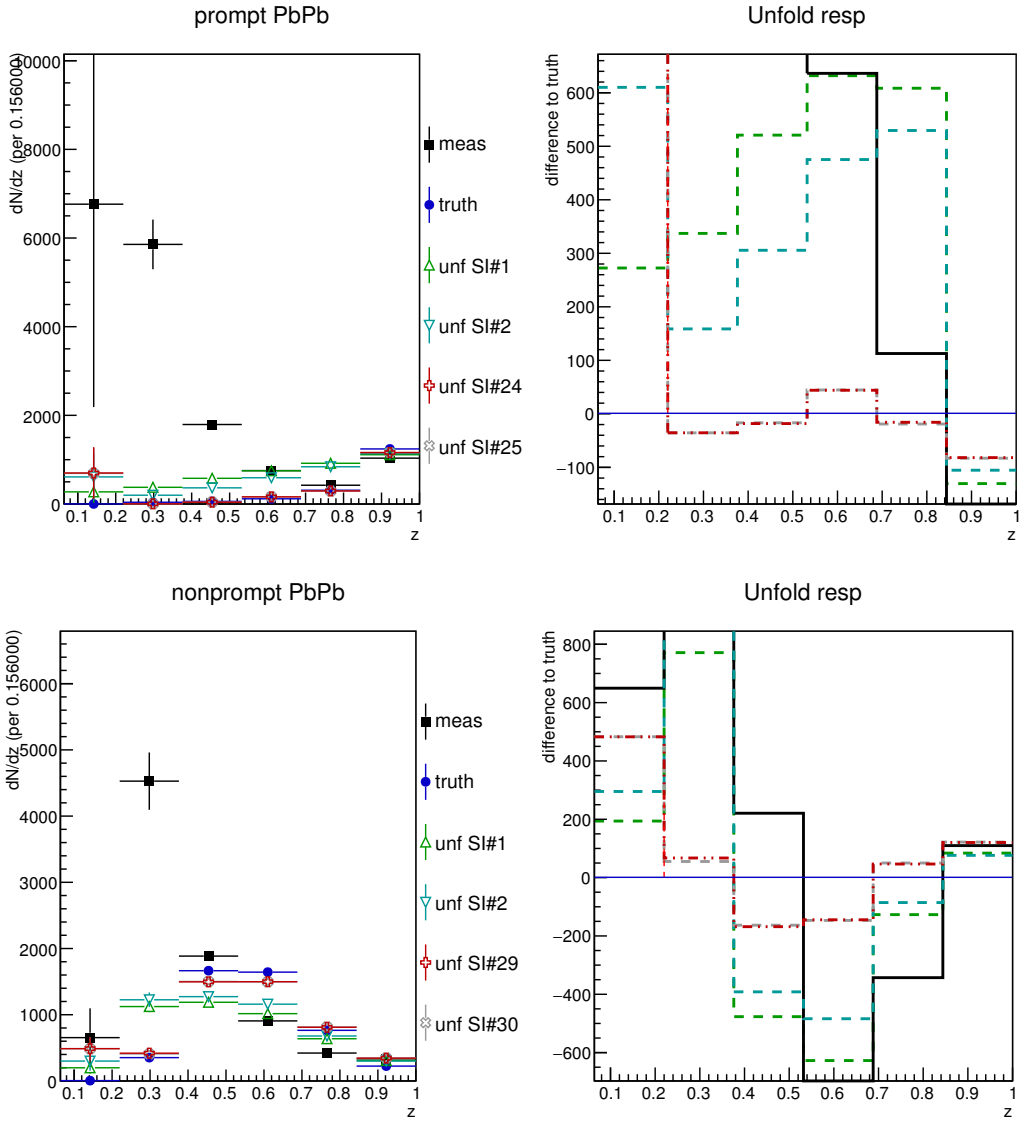

Figure 3.59: Closure test of the unfolding in MC for prompt J/ψ in PbPb collisions for prompt (top) and nonprompt (bottom). The left set of panels shows the truth, measured and unfolded z distribution after selected super-iterations, while the right shows the difference between these and the true z distribution.

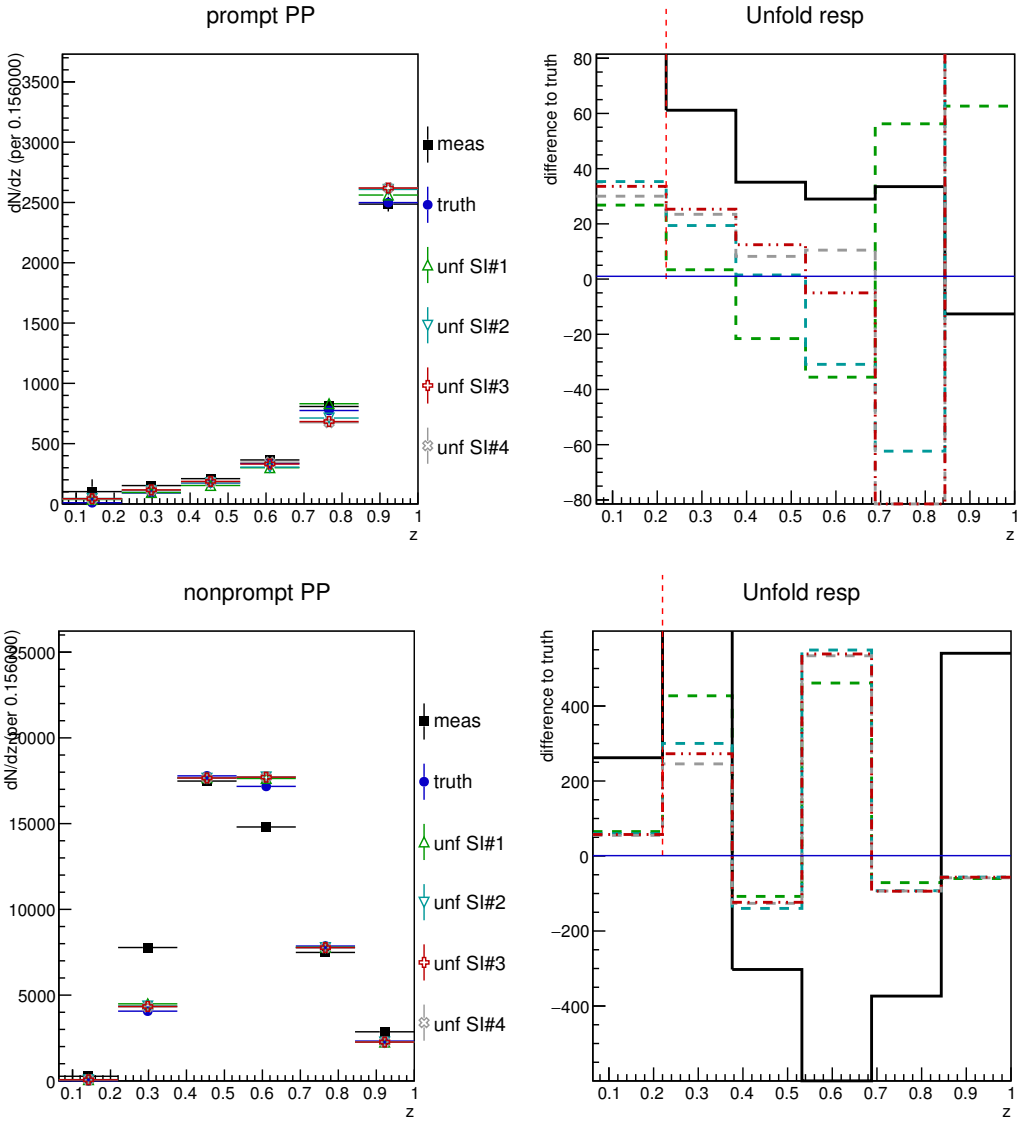

Figure 3.60: Closure test of the unfolding in MC for prompt J/ψ in pp collisions for prompt (top) and nonprompt (bottom), which have been smeared to emulate the statistical precision of real data. The left set of panels shows the truth, measured and unfolded z distribution after selected super-iterations, while the right shows the difference between these and the true z distribution.

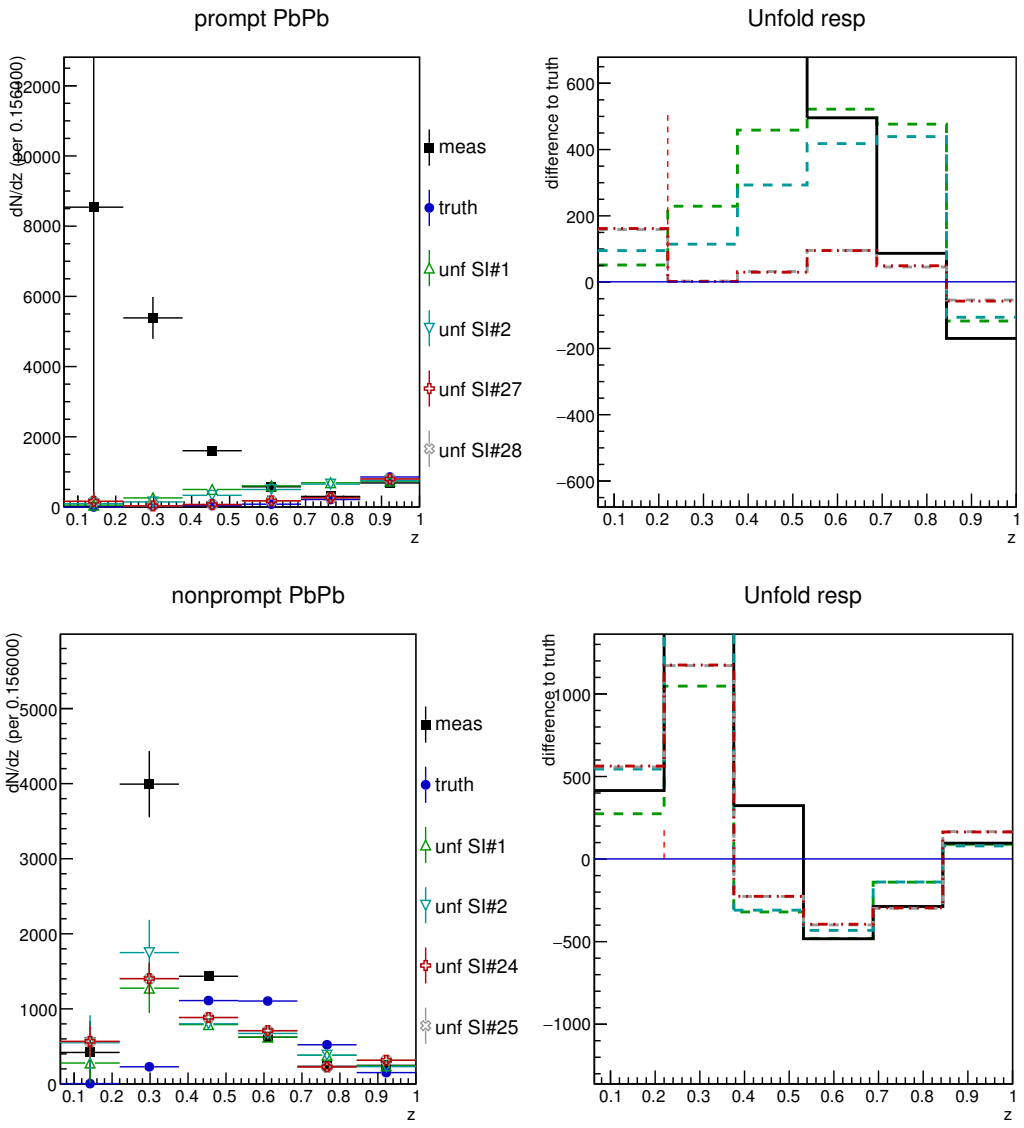

Figure 3.61: Closure test of the unfolding in MC for prompt J/ψ in central PbPb collisions for prompt (top) and nonprompt (bottom). The left set of panels shows the truth, measured and unfolded z distribution after selected super-iterations, while the right shows the difference between these and the true z distribution.

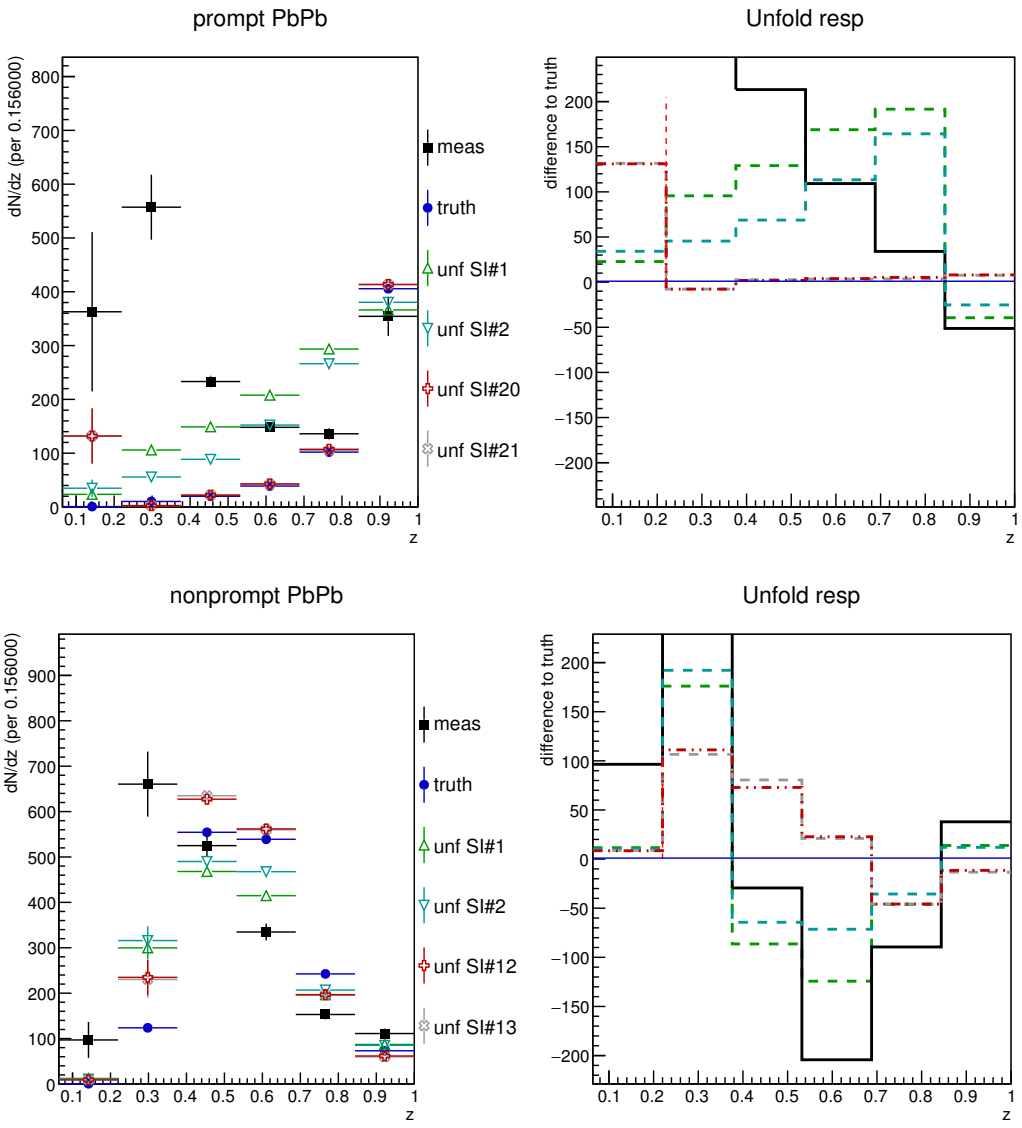

Figure 3.62: Closure test of the unfolding in MC for prompt J/ψ in central PbPb collisions for prompt (top) and nonprompt (bottom). The left set of panels shows the truth, measured and unfolded z distribution after selected super-iterations, while the right shows the difference between these and the true z distribution.

Figure 3.63 shows the unfolding procedure applied to the prompt J/ψ data in pp and PbPb collisions. The transfer matrix is smeared to account for the data-to-simulation difference in jet energy resolution, as described in Section 3.12. The best regularization settings from the test with the smeared prompt MC are used. In pp, where the number of iterations is set to 3, the majority of the difference between the unfolded and truth distributions is already apparent after the first super-iteration (which is the selected setting). Further super-iterations change the result somewhat but are changing very little by super-iteration 6, which is also the case in the MC test. PbPb also shows an evolution that is qualitatively similar to the MC. With the selected setting of 3 iterations, the large peak at low z is already removed by the end of the first super-iteration. As in MC, the PbPb data require a larger number of super-iterations to become stable, but no longer change by the chosen setting of 25 super-iterations.

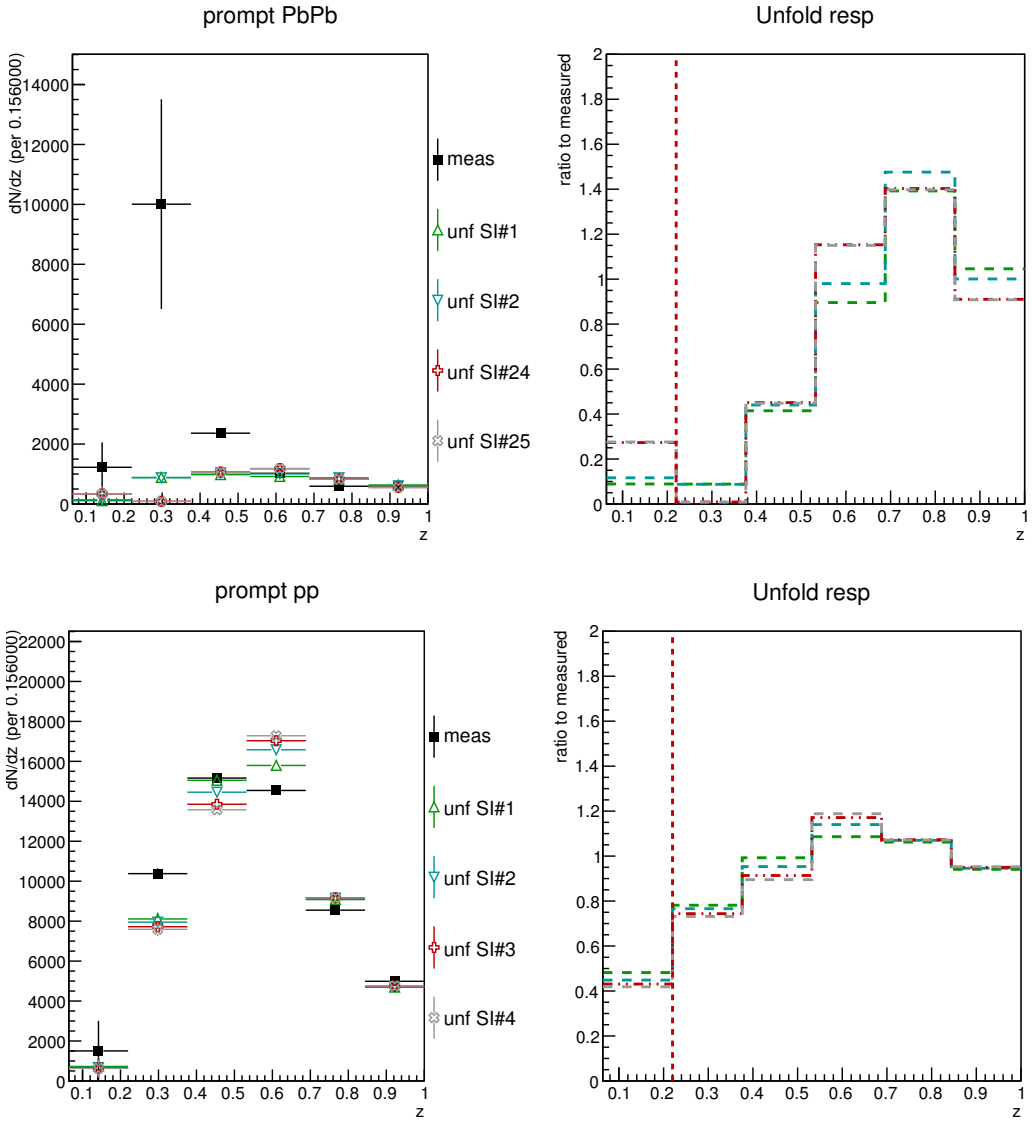

Figure 3.63: Unfolding of prompt J/ψ data for pp (top) and PbPb (bottom). The left panels show the measured z distributions in the nominal jet p_{T} bin, and the unfolded ones after various numbers of super-iterations, as indicated in the legend. The right panels show the ratios of the unfolded distributions to the measured ones.

3.14 Jet-related uncertainties

The jet energy scale uncertainties correspond to the JEC explained in Section. 3.8. The CMS calorimeters are calibrated using the single-pion response (SPR). The simulated jet response corrections are sensitive to SPR calibration, especially at low p_T through neutral hadrons. SPR was checked on proton-proton data, confirming good modeling of the barrel response within $\pm 3\%$. The JEC sensitivity to a $\pm 3\%$ change in SPR is at most 2.3%.
The uncertainty on the residual corrections rises from many sources. The uncertainty on the relative corrections is estimated from uncertainties on the initial- and final-state radiation, the jet p_T resolution, statistics of the MC samples, and the time dependence (estimated from different data-taking periods). The uncertainty on the absolute corrections rises from uncertainties on the fitted absolute scale, the HCAL scale, the statistics of the MC samples, and the bias on the MPF method. More details on each of the variations can be found in Ref. [118].
The uncertainty at $p_T = 30$ GeV, as a function of η is shown in Fig. 3.64. In pp, the uncertainty varies from about 3 – 4%. In PbPb the uncertainty is around 4%, except in the barrel-endcap transition region ($1.2 < \eta < 1.6$), where it reaches around 10%.

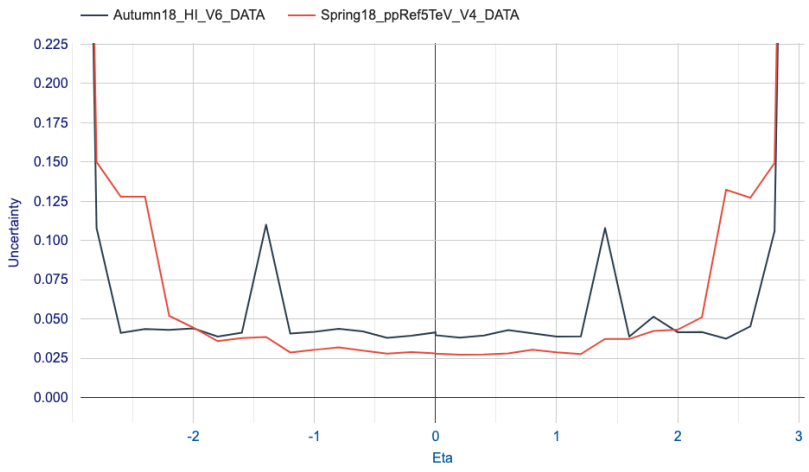

Figure 3.64: Uncertainty on the jet energy scale, as a function of η, in pp and PbPb data.

The uncertainty does not apply to the fraction of the jet that is comprised of the muons from J/ψ, as the muon kinematics are much more precisely known. The J/ψ component of jet does not lead to any uncertainty on the jet energy scale, as the J/ψ p_T enters both the numerator and denominator in the ratio z. The J/ψ does of course have a finite resolution, but this is small compared to the relatively poor resolution of the "jetty" component, i.e., the part of the jet whose momentum is given by $1 - z$.
The variation of the jet energy scale is propagated by shifting the reconstructed jet p_T values in the transfer matrix used in the unfolding. For illustrative purposes, in Fig. 3.65, the

effect of the energy scale shift on the measured z distribution is shown for the nominal jet p_T selection. Rather than perform the fits to extract the prompt yield, we simply select on J/ψ in the mass range of 3 – 3.2 GeV, without applying any lifetime selection.

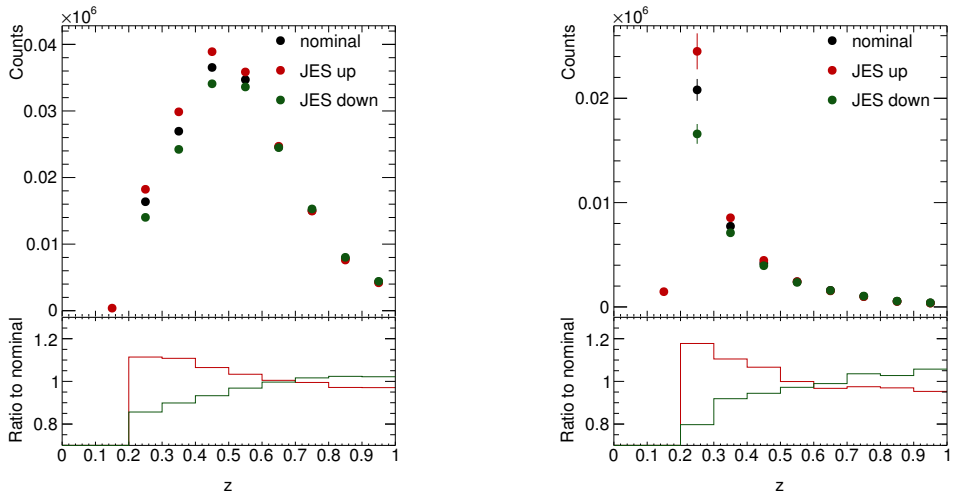

Figure 3.65: Effect of shifting the JES within its uncertainties in pp (left) and PbPb (right) data. Rather than extracting the yield from fits, we restricted the invariant mass of the J/ψ candidate to 3 – 3.2 GeV.

To propagate the uncertainty from jet p_T resolution, the data/MC scale factors discussed in Section 3.12 are varied according to their uncertainties, and the unfolding is repeated. The uncertainties that correspond to the dijet asymmetry rise from ISR+FSR correction and radiation, Particle-level imbalance, Non-Gaussian tails, PU reweighting, Jet energy scale, and parameterization uncertainties. The uncertainties for the γ+jet balance rise from QCD dijet background contamination, flavor uncertainty, OOC showering, jet energy scale, and PU reweighting. More details on each of the uncertainty sources can be found in Ref. [118].
For the 2018 data, the uncertainty on these scale factors ranges from about 3% in mid-rapidity to about 7%, for the endcap and transition regions. For 2017 data, the uncertainty is comparable in the barrel region (2 – 4%, depending on η), but is larger in the endcap and transition regions, where it varies from 10 – 20%, depending on η. The contribution to the jet resolution from the PbPb underlying event is estimated by varying the centrality definition in MC, as described in Section 3.12. The centrality is shifted by 5% for the nominal results. 0% and 10% are taken as uncertainties. Fig. 3.66 shows the unfolded z distributions with the three centrality shifts.
An uncertainty is attributed to the regularization strength used in the unfolding by changing from the best settings derived from prompt J/ψ MC, to the ones derived from non-prompt J/ψ MC, as shown in Fig. 3.67. These settings are explained in Section 3.13.
The statistical uncertainty on the transfer matrix is also estimated. This is done by pro-

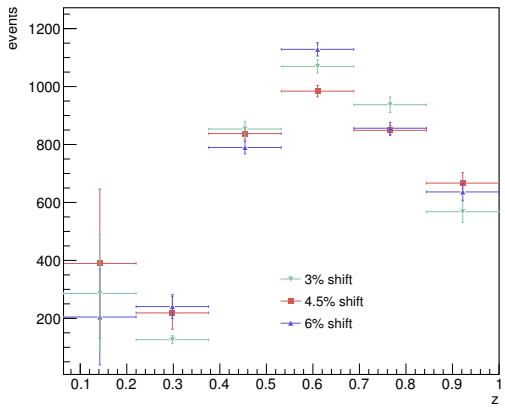

Figure 3.66: Unfolded results with different MC centrality shifts in prompt data for pp (left) and PbPb collisions (right).

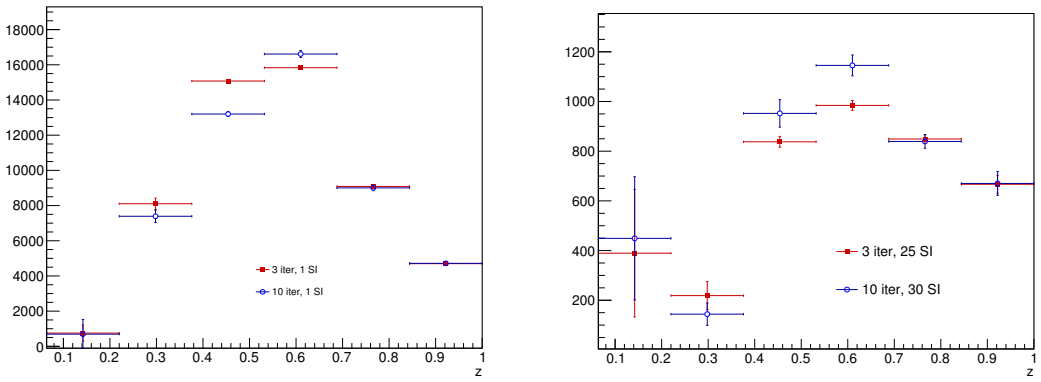

Figure 3.67: Unfolded results with different regularization settings in prompt data for pp (left) and PbPb collisions (right).

ducing 100 toy variations of the MC transfer matrices by smearing the bin contents by their statistical uncertainties (exactly as done for the acceptance x efficiency errors). The uncertainty is shown in Fig 3.68 for pp and PbPb.

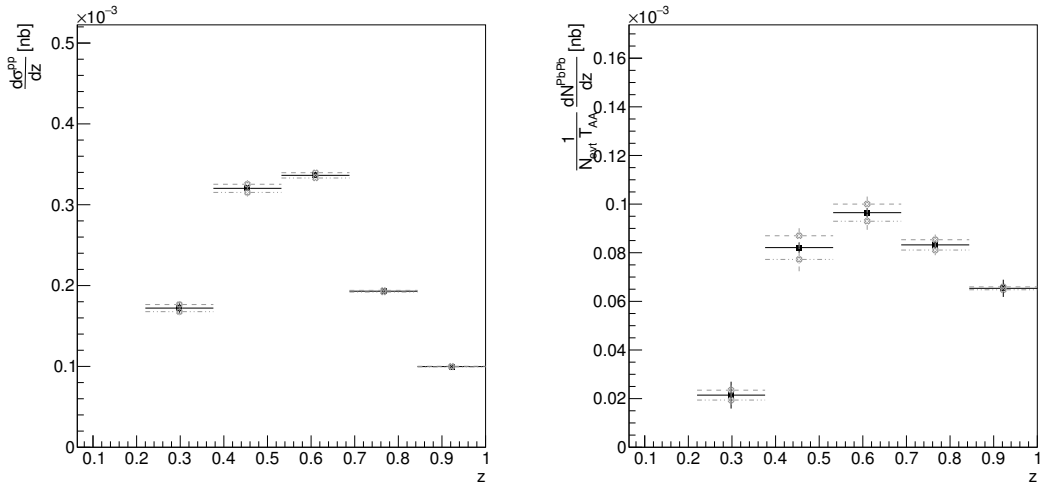

Figure 3.68: Systematic uncertainties coming from the statistical uncertainty on the response matrix for pp (left) and PbPb (right)

Finally, an uncertainty is assigned on the shape of the prior distribution. This is done by relaxing the assumption of a prior that is flat in z, which is quite far from the data, to the z shape taken from nonprompt MC, which is closer to the shape found in pp data by LHCb [66]. Fig 3.69 shows the difference between the unfolded distributions for the two prior choices.

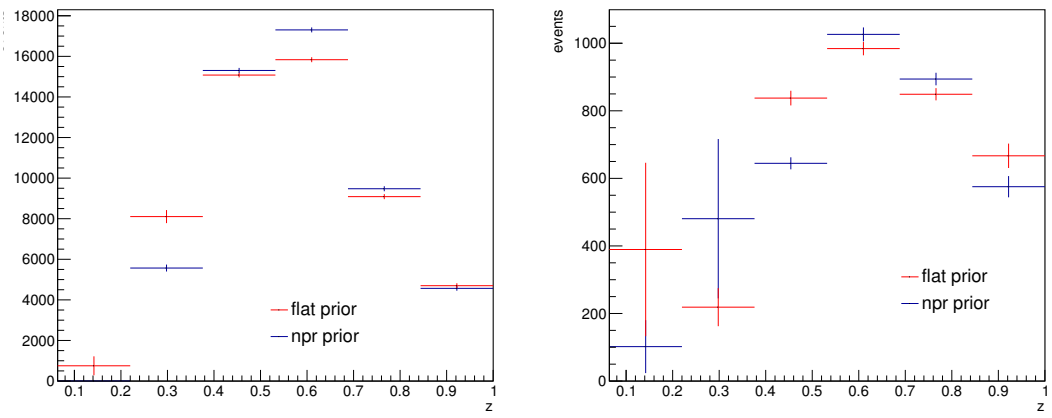

Figure 3.69: Systematic uncertainties coming from the uncertainty on the shape of the prior for pp (left) and PbPb (right)

3.15 Summary of systematic uncertainties

The systematic uncertainty is broken down into several sources shown in Fig. 3.70. The relative uncertainties are shown in Fig. 3.71 All sources of systematic uncertainty on the J/ψ signal extraction, which were presented in Section 3.10, are summed together in quadrature. The various sub-sources of jet related uncertainties, presented in Section 3.14, are shown individually on the plot.

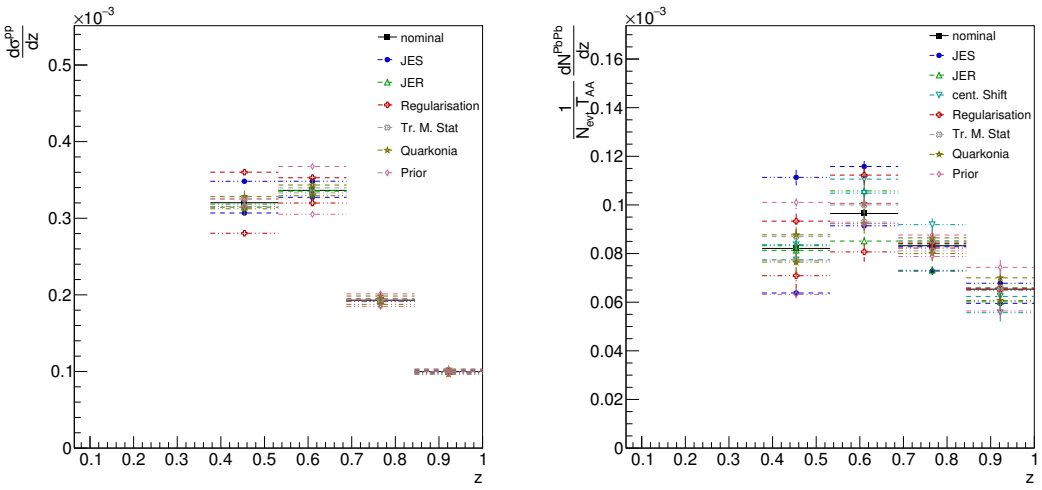

Figure 3.70: Systematic uncertainties for prompt J/ψ mesons in pp (left) and PbPb (right) collisions as a function of z.

Cross-section measurements in pp collisions have an overall uncertainty from the integrated luminosity of 3.5% that is obtained from an analysis of data from a van der Meer scan [133]. The PbPb data are normalized by the equivalent number of hadronic nucleon-nucleon interactions in the data sample and T_{AA}, which is determined from an MC implementation of the Glauber model [134] with a total hadronic PbPb cross-section of 7.644 $\pm$ 0.008 barns. The values of T_{AA} used in this analysis are 6.27 $\pm$ 0.14, 18.79 $\pm$ 0.36, and 2.717 $\pm$ 0.098 mb^{-}1, for the 0-90, 0-20 and 20-90% centrality selections, respectively.
The uncertainty on the number of hadronic interactions has an uncertainty of 1.3% coming from the selection of such events, taking into account possible contamination from electromagnetic interactions and beam backgrounds.

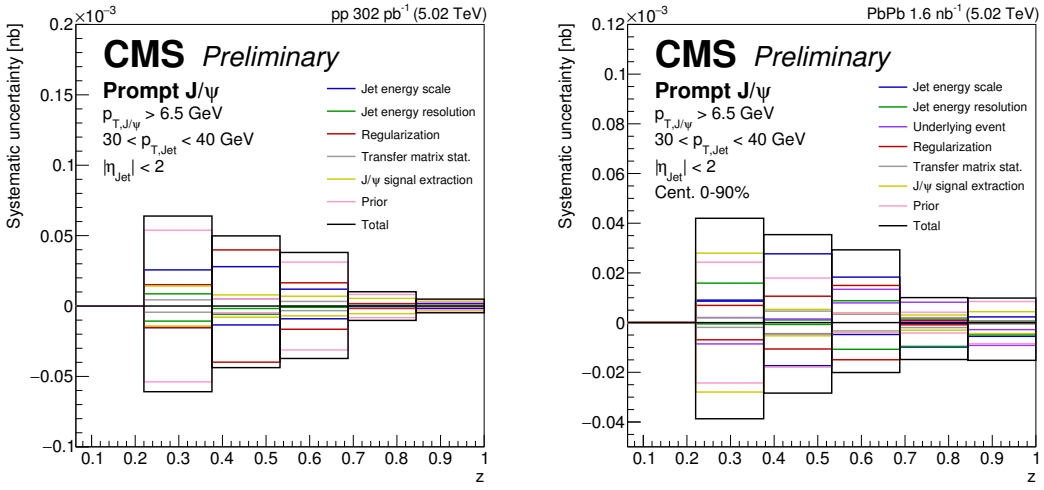

Figure 3.71: Absolute systematic uncertainties for prompt J/ψ mesons in pp (left) and PbPb (right) collisions as a function of z.

Chapter 4

Results

4.1 Prompt and nonprompt J/ψ-in-jets results in pp collisions with 2015 data

The results presented in this section are derived using the 2015 pp reference run at 5 TeV [132]. The fragmentation function of jets containing prompt and nonprompt J/ψ mesons are measured for jets of $25 < p_{\mathrm{T}} < 35$ GeV. The self-normalized z distributions are presented for mid-rapidity and forward rapidity in Figs. 4.1 and 4.2, respectively, compared to generator-level predictions from PYTHIA 8.

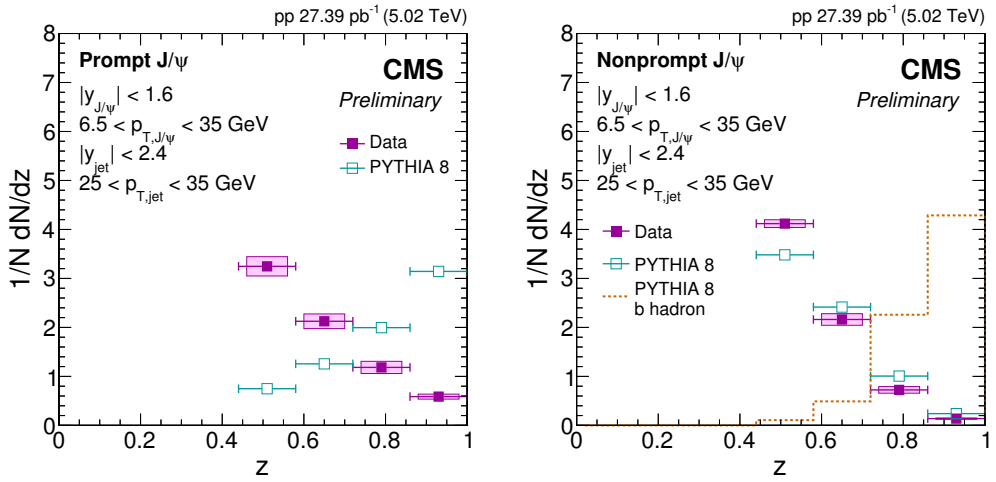

Figure 4.1: Self-normalized prompt (left) and nonprompt z distributions in the rapidity range $|y| < 1.6$, for pp data and PYTHIA 8. For the nonprompt case, the z distribution of the parent b hadron is also shown.

The prompt and nonprompt data show a qualitatively similar trend in each of the rapidity selections. A similar trend is also observed in PYTHIA 8 for nonprompt J/ψ, although

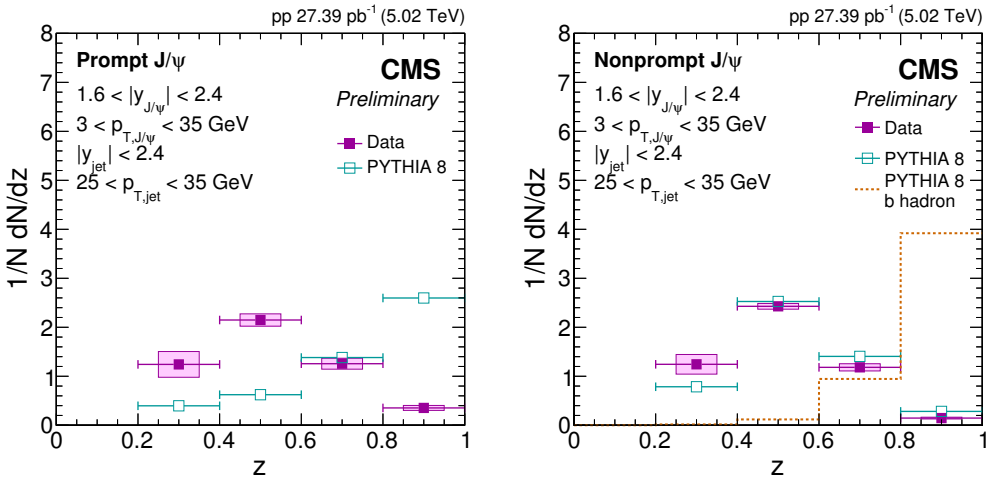

Figure 4.2: Self-normalized prompt (left) and nonprompt z distributions in the rapidity range $1.6 < |y| < 2.4$, for pp data and PYTHIA 8. For the nonprompt case, the z distribution of the parent b hadron is also shown.

the z distributions are slightly harder than the data. The trend for prompt J/ψ in PYTHIA 8, on the other hand, is very different than that observed in data. The z distribution is much harder and peaked at $z = 1$, indicating that the jet activity accompanying J/ψ mesons is underestimated. These results confirm the trends observed in Ref. [66] but in a different rapidity range and per-nucleon center-of-mass energy. For the nonprompt case, the z distribution of the parent b hadron from PYTHIA 8 is also shown, which is peaked at much larger values of z compared to the daughter J/ψ. The apparent similarity of the prompt and nonprompt J/ψ in data should therefore be interpreted with caution, as decay kinematics play a large role in the latter case.

While the jet activity around J/ψ mesons appears to be underestimated by PYTHIA, only a small fraction of J/ψ belong to jets in the selected p_{T} range of 25 to 35 GeV. The fraction of prompt and nonprompt J/ψ mesons in jets, as well as the data-to-MC ratio of these fractions, is shown in Fig. 4.3, for J/ψ above the minimum p_{T} threshold of 6.5 and 3 GeV, at mid and forward rapidity, respectively. To evaluate this ratio, the numerator is taken by integrating the z distributions, without applying the self-normalization. The systematic uncertainties are treated as uncorrelated point-to-point. The denominator is evaluated by performing the 2D fitting procedure without any constraint on the associated jet. We find that the fraction of J/ψ produced in jets in the selected p_{T} range is underpredicted by PYTHIA 8 for both prompt and nonprompt J/ψ, for both rapidity selections. The nonprompt J/ψ show a larger jet fraction than is observed for prompt J/ψ. This suggests that J/ψ at lower values of p_{T} are less jet-like than nonprompt J/ψ. These J/ψ-in-jet fractions have not been studied before, to our knowledge, and provide complementary information to the z distributions that should prove useful for model comparisons.

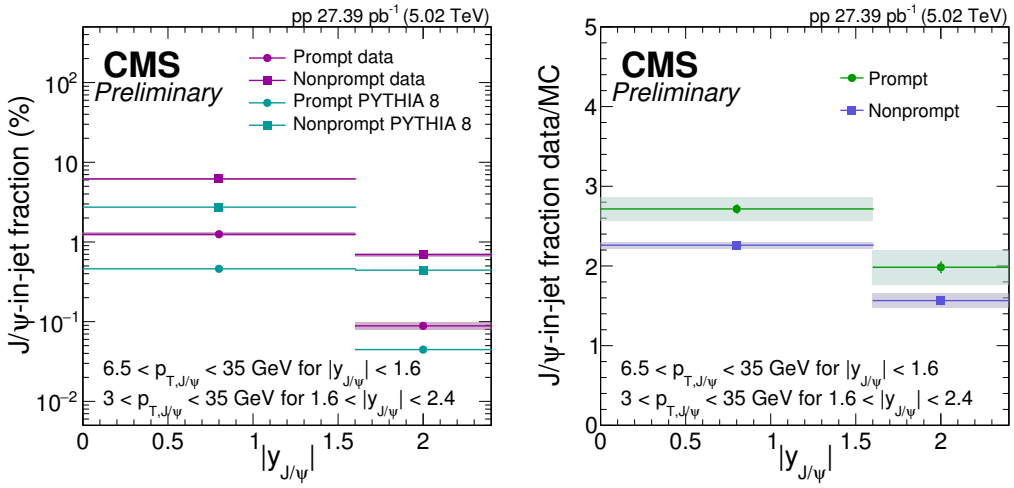

Figure 4.3: Left: The fraction of prompt and nonprompt J/ψ in jets of $25 < p_{\mathrm{T}} < 35$GeV in pp data and in PYTHIA 8, compared to the total number of J/ψ in the relevant the p_{T} interval, as indicated on the Figure. Right: The ratio of these J/ψ-in-jet fractions in data compared to simulation for prompt and nonprompt J/ψ.

4.2 Prompt J/ψ-in-jets results in pp and PbPb with 2017 and 2018 data

The results presented in this section are derived from the 2017 pp reference run at 5 TeV and the 2018 PbPb data taking. The fragmentation function of jets containing prompt J/ψ mesons are measured for jets of $30 < p_{\mathrm{T}} < 40$ GeV and $|\eta| < 2$. Figure 4.4 shows the self-normalized distribution of the fragmentation variable z for prompt J/ψ mesons in pp data. A shape comparison is performed to generator-level predictions from PYTHIA 8 for prompt and nonprompt J/ψ signal. In contrast to the PYTHIA 8 simulation, the data show a relatively large degree of surrounding jet activity, and the distribution resembles more closely that of nonprompt than prompt J/ψ simulation, similarly to what was seen in the previous section for different kinematics.
Figure 4.5 (left) shows the same z distribution in pp collisions, this time normalized as a differential cross-section, along with the per-event yield of prompt J/ψ mesons in PbPb collisions. In order to compare the two collision systems, the PbPb yields are scaled by the nuclear overlap factor T_{AA}. The PbPb data are also peaked at an intermediate value of z, indicating a sizeable amount of small-angle hadroproduction.
The PbPb data show a suppression level that is quantified by the ratio of these two distributions, R_{AA}, shown in Fig. 4.5 (right). The data show a slight rising trend as a function of z. In the largest z bin, isolated J/ψ are less suppressed in comparison to lower values of z, where the J/ψ is surrounded by a large degree of jet activity.
Figure 4.6 shows the R_{AA} for two centrality selections, 0–20 and 20–90%. A larger degree

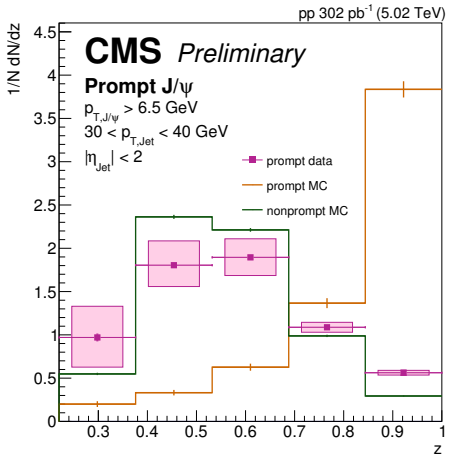

Figure 4.4: Normalized z distribution in pp collisions, compared to prompt and non-prompt J/ψ in PYTHIA8, at the generator level.

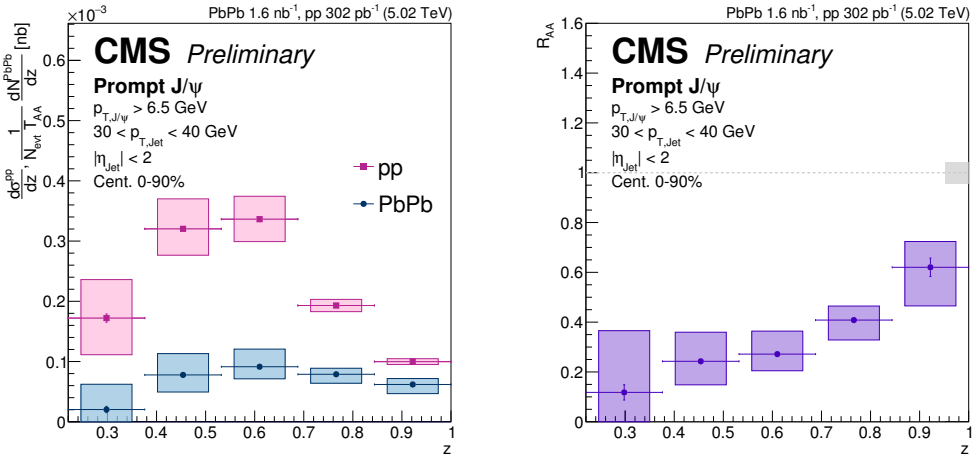

Figure 4.5: Left: J/ψ yields, as a function of z in pp and PbPb collisions. Right: the nuclear modification factor R_{AA}, as a function of z. The box around unity shows the normalization uncertainty.

of suppression is observed for the more central selection. The rising trend with increasing z is also more pronounced in central events.

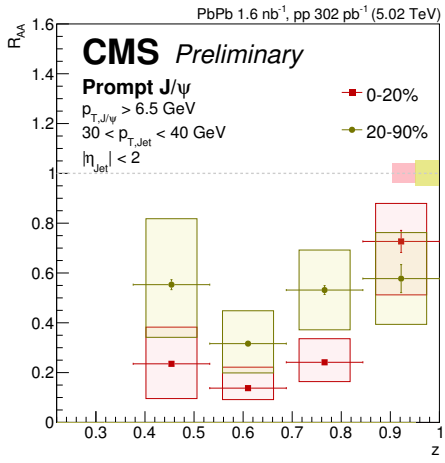

Figure 4.6: The nuclear modification factor R_{AA} for two centrality selections of PbPb collisions, as a function of z. Due to limited statistical precision, the lowest z bin is excluded. The boxes around unity show the normalization uncertainties.

4.3 Discussion

The larger jet activity observed in pp data compared to Leading-Order NRQCD calculations implemented in PYTHIA 8 cannot be explained by the classical J/ψ production picture. However, the NLL' calculations presented in Section. 1.2.4 introduce the production of prompt J/ψ inside of parton showers. The z distributions with this new approach showed a much better agreement with data. The assumption of J/ψ being produced in a parton shower does not only affect the small-angle hadroproduction around the J/ψ meson, but it also implies that J/ψ are produced at a later time to what is assumed in the classical picture. In the new approach, the rising trend of R_{AA} of prompt J/ψ in jets as a function of z can be explained by jet quenching, i.e. E_{Loss} processes. A J/ψ meson with a low value of z tends to be produced late in the parton shower. The cascade of partons traversing the hot medium loses energy by interacting with the deconfined color states in the QGP. E_{loss} processes can affect the J/ψ in two ways: The partons can lose energy before the formation of the J/ψ. In this case, the entire jet including the J/ψ is affected and can be suppressed or migrate outside of the jet p_T selection. The second is after the J/ψ is formed. The partons of the jet keep losing energy before they hadronize. The J/ψ itself does not lose energy so it shifts towards higher z values. Of course, the J/ψ is still susceptible to Debye screening and can dissociate. The c and the $\bar{c}$ can also lose energy by interacting with the QGP before they are bound into a J/ψ state.

Since the jet p_T range is limited to 30–40 GeV, the z range of 0.22–1 is comparable to J/ψ p_T of ∼6.5–30 GeV. The rising trend of J/ψ in jets as a function of p_T is qualitatively similar to the rising trend observed for inclusive prompt J/ψ, i.e. without an explicit jet requirement, for the comparable p_T range that was shown previously in Fig. 1.18 in Section. 1.2.4 compared to open charm R_{AA} and can also be seen in Fig. 4.7 compared to hidden beauty R_{AA}. Even though the fraction of prompt J/ψ produced in jets of 30–40 GeV is small compared to the total number of prompt J/ψ mesons because of the jet p_T constraint, a measurement that was done by CMS at 8 TeV [135] showed that $(85 \pm 3\ (\text{stat}) \pm 7\ (\text{syst}))\%$ of J/ψ of $E_{J/\psi} > 15$ GeV are produced with a jet of $E_{Jet} > 19$ GeV.
To disentangle the different sources of J/ψ suppression, one can look at other measurements like bottomonium suppression in heavy-ion collisions. The suppression of Y states in PbPb is dominated by Debye screening. Within the systematic uncertainties, the Y R_{AA}, presented in Fig.4.7, show no clear dependence on p_T and does not rise at high p_T in comparison to J/ψ R_{AA}.

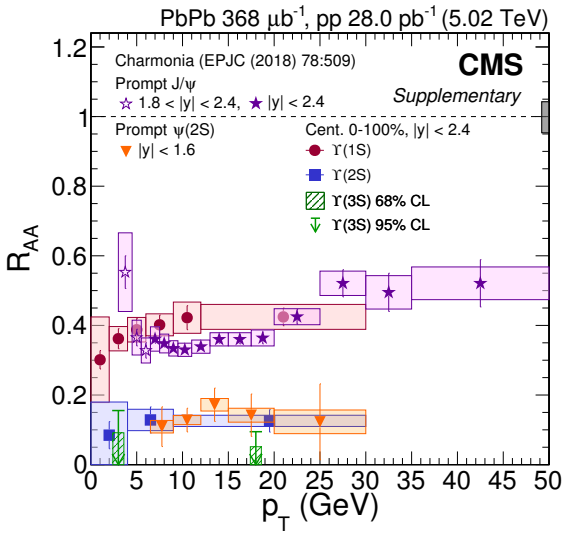

Figure 4.7: Nuclear modification factor for the Y(1S), Y(2S) and Y(3S) mesons [136] as well as the J/ψ and ψ(2S) mesons [123] as a function of p_T at 5.02 TeV.

This further hints in the direction of E_{Loss} processes explaining the rise of J/ψ at high p_T. The b quark is heavier than the c quark. So even in the case of quarkonium production in parton showers, charmonia would be more affected by the medium than bottomonia. The study of Y mesons in jets can provide very useful information for quarkonium production. Since Y mesons can be measured down to $p_T = 0$ in CMS, the fragmentation function can also be measured down to $z = 0$. Measuring the fragmentation function of jets containing an Y state in pp data can provide a direct comparison to NLO and NLL' NRQCD models. After that, measuring the fragmentation function in PbPb would allow a direct comparison in R_{AA} between charmonia and bottomonia in PbPb collisions.

With more statistics, it would also be very interesting to duplicate the J/ψ measurement in different jet p_{T} ranges, which should prove useful for model comparisons in pp and PbPb, since jet fragmentation functions are usually measured as a function of jet p_{T}. The comparison between charmonium ground and excited states regarding their production in jets is also intriguing since Debye screening is expected to be different for states with different binding energies, but collisional and radiative $\mathrm{E_{Loss}}$ processes are unsusceptible to the final state.

Chapter 5

Conclusions

The J/ψ meson is a powerful tool to probe the Quark-Gluon Plasma. It is used in heavy-ion collisions to study the characteristic of the hot medium. However, the production of the prompt J/ψ is still not fully understood. Despite the big efforts on the theory sides, the existing models for prompt J/ψ production are not able to reproduce both the cross-section and the polarization measurements. The study of the fragmentation function of jets containing a J/ψ meson can provide helpful information about the isolation of J/ψ in its production. It was seen that leading-order nonrelativistic QCD calculations, implemented in simulation, do not reproduce the results of the fragmentation function of prompt J/ψ in pp collisions. A new approach based on the assumption of the J/ψ being produced in parton showers displayed a better agreement with data than LO NRQCD. This assumption implies that the J/ψ is produced at later times and can alter the usual interpretation of J/ψ results in heavy-ion collisions.
In this thesis, the fragmentation function of jets containing a J/ψ was first measured for prompt and nonprompt J/ψ in pp collisions for jets of 25 – 35 GeV. I was responsible for the J/ψ signal extraction including the bidimensional fitting and the acceptance and efficiency corrections, and their systematic uncertainties. Afterward, the fragmentation function was measured for prompt J/ψ in pp and PbPb collisions for jets of 30 – 40 GeV. This time, I was responsible for the J/ψ signal extraction, the acceptance and efficiency corrections, and the 2D unfolding procedure. I was also responsible for providing the centrality calibration and the Tag&Probe scale factors for low-p_{T} muons for the 2018 PbPb run.
When the self-normalized pp distributions were compared to simulation the discrepancy was still present. The comparison between the cross-section in pp and the per-event yield in PbPb showed suppression of prompt J/ψ in jets in all bins of the fragmentation variable $z \equiv p_{\mathrm{T,J/}\psi} / p_{\mathrm{T,jet}}$. The ratio of the two distributions, $\mathrm{R_{AA}}$, showed a rising trend as a function of p_{T} that can be explained using jet quenching mechanisms according to the assumption of J/ψ being produced in parton showers.

Chapter 6

Resumé en Français

Quelques microsecondes après le Big Bang, la matière existait sous la forme d'un plasma de quarks et de gluons asymptotiquement libres appelé QGP. Pour recréer des conditions similaires à celles de l'univers primitif, de puissants accélérateurs heurtent des noyaux lourds pour former de nombreuses petites boules de feu dans lesquelles les nucléons "fondent" en plasma de quarks et de gluons. Le QGP a une courte durée de vie et ne peut pas être vu directement. Alors, de nombreuses particules sont utilisées comme signatures de sa formation et comme outils pour étudier ses propriétés. L'une d'entre elles est le méson J/ψ, une particule composée d'un quark charme et d'un anti-charme qui, en presence du QGP, ne peuvent pas former l'état de J/ψ. Dans ce cas le J/ψ est supprimé. Mais la production de J/ψ n'est pas encore complètement comprise, malgré le grand progrès réalisé dans les collisions d'ions lourds, et celles de protons où la formation de QGP n'est pas attendue. Les modèles actuels de la chromodynamique quantique ne peuvent pas reproduire toutes les mesures expérimentales de J/ψ. Une approche théorique récente évoque la production des mésons J/ψ dans les gerbes de parton ou dans les jets. Ceci est étudié expérimentalement en mesurant la fonction de fragmentation des jets contenant un J/ψ, c'est-à-dire en vérifiant le degré d'isolation du méson J/ψ pendant sa production. La thèse rapporte le travail de deux analyses qui mesurent la fragmentation des jets contenant un méson J/ψ dans les collisions pp et PbPb.

Chapitre 1 commence par une description générale de la chromodynamique quantique et termine par les principales questions auxquelles cette thèse tente de répondre. Une grande partie concerne la formation du plasma de quark gluon et les sondes utilisées pour l'étudier. La section suivante se concentre sur le méson J/ψ et sa production dans les collisions pp et PbPb. À la fin du chapitre, les résultats de la fonction de fragmentation des jets contenant un méson J/ψ dans les collisions pp, par la collaboration LHCb, sont présentés avec une comparaison avec différentes approches théoriques. La comparaison favorise l'idée que les mésons J/ψ sont produits dans des gerbes de parton.

Chapitre 2 contient une description des appareils expérimentaux utilisés pour collecter les données. Dans le LHC, deux faisceaux de particules sont accélérés dans des directions opposées dans des tubes de faisceaux séparés et se croisent en quatre points d'interaction. Le détecteur CMS, qui le détecteur par lequel les données utilisées dans cette thèse ont été

recueillies, est situé autour un des points d'interactions. CMS est composé de plusieurs sous détecteurs, chacun ayant un rôle spécifique dans la détection et la reconstruction des particules: un trajectographe pour identifier la charge et l'impulsion des particules chargées, des calorimètres pour mesurer l'énergie des photons, électrons et hadrons, et un système à muons pour identifier et reconstruire les muons. Les mesures très précises de l'impulsion sont possibles grâce à l'aimant de CMS qui est le solénoïde supraconducteur le plus puissant jamais construit.
Chapitre 3 concerne la procédure d'analyse utilisée pour obtenir les fonctions de fragmentation des jets contenant un méson J/ψ. Il commence par la reconstruction des objets à partir des impacts et des amas dans le détecteur. Le canal muonique est utilisé pour détecter les mésons J/ψ. Les muons sont reconstruits à partir des impacts dans le trajectographe et les chambres à muons. Les jets sont reconstruits à l'aide de l'algorithme de "Particle Flow" qui utilise les informations de tous les sous-détecteurs pour reconstruire chaque objet dans l'événement. Puis, les objets sont regroupés en jets à l'aide de l'algorithme anti-kt. Les événements et les objets répondent à des critères de sélection, tels que le trigger et l'identification du muon. La calibration de la centralité est également abordée. Les événements sont divisés en 200 cases de centralité depuis les événements les plus centraux, où les noyaux entrent en collision frontale, jusqu'aux événements périphériques, où les noyaux se chevauchent partiellement.
Après la sélection et la détermination de la centralité, les J/ψ et les jets sont associés et la variable de fragmentation, z, est calculée comme la fraction du pt du jet prise par le J/ψ. Les candidats J/ψ sont divisés en z et jet pt et une procédure de fit en deux dimensions est utilisée pour obtenir les taux de production de J/ψ prompt et non-prompt dans les jets, le prompt étant le J/ψ produit directement dans les collisions et le non-prompt étant le J/ψ provenant de la désintégration des hadrons B. La procédure de montage se fait sur la masse et la durée de vie du J/ψ. Les taux sont corrigés en fonction de l'acceptation du détecteur et de l'efficacité de la reconstruction du muon et des critères de sélection. Avant d'obtenir les résultats finaux, une procédure de "unfolding" est appliquée pour corriger la migration de pt de jet. Elle est effectuée en deux dimensions : pt de jet et z.
Dans les chapitres 4 et 5, les résultats réalisées dans le cadre de cette thèse sont présentées, suivis d'une discussion sur l'impact de ces résultats sur notre compréhension de la production de méson J/ψ en pp et PbPb. En pp, la fonction de fragmentation de J/ψ dans les jets a montré que les mésons J/ψ ont une activité de jet plus importante que ce qui est prédit par les modèles de NRQCD. Les résultats de PbPb ont montré un comportement similaire à celui de pp mais avec une suppression de J/ψ dans les jets dans tous les bins de z. La comparaison entre pp et PbPb a montré que les J/ψ isolés sont moins supprimés que ceux qui viennent avec une activité de jet plus importante. Les résultats favorisent la production de J/ψ dans les gerbes de parton et au rôle de "quenching" des jets en tant que mécanisme contribuant à la suppression de méson J/ψ.

Bibliography

[1] G. Dissertori. The Determination of the Strong Coupling Constant. *Adv. Ser. Direct. High Energy Phys.*, 26:113–128, 2016.

[2] F. Karsch. Lattice QCD at high temperature and density. *Lect. Notes Phys.*, 583:209–249, 2002.

[3] John C. Collins and M. J. Perry. Superdense Matter: Neutrons Or Asymptotically Free Quarks? *Phys. Rev. Lett.*, 34:1353, 1975.

[4] Raimond Snellings. Elliptic Flow: A Brief Review. *New J. Phys.*, 13:055008, 2011.

[5] Edward V. Shuryak. The QCD vacuum, chiral phase transition and quark - gluon plasma. pages 211–263, 3 1995.

[6] G. Baym, B.L. Friman, J.P. Blaizot, M. Soyeur, and W. Czyz. Hydrodynamics of Ultrarelativistic Heavy Ion Collisions. *Nucl. Phys. A*, 407:541–570, 1983.

[7] Ulrich W. Heinz and Maurice Jacob. Evidence for a new state of matter: An Assessment of the results from the CERN lead beam program. 1 2000.

[8] John Adams et al. Experimental and theoretical challenges in the search for the quark–gluon plasma: The STAR Collaboration's critical assessment of the evidence from RHIC collisions. *Nucl. Phys. A*, 757:102, 2005.

[9] K. Adcox et al. Formation of dense partonic matter in relativistic nucleus-nucleus collisions at RHIC: Experimental evaluation by the PHENIX Collaboration. *Nucl. Phys. A*, 757:184, 2005.

[10] I. Arsene et al. Quark-gluon plasma and color glass condensate at RHIC? The perspective from the BRAHMS experiment. *Nucl. Phys. A*, 757:1, 2005.

[11] B.B. Back, M.D. Baker, M. Ballintijn, D.S. Barton, B. Becker, et al. The PHOBOS perspective on discoveries at RHIC. *Nucl. Phys. A*, 757:28, 2005.

[12] National Research Council. *Nuclear Physics: Exploring the Heart of Matter*. The National Academies Press, Washington, DC, 2013.

[13] Michael L. Miller, Klaus Reygers, Stephen J. Sanders, and Peter Steinberg. Glauber modeling in high-energy nuclear collisions. *Ann. Rev. Nucl. Part. Sci.*, 57:205, 2007.

[14] B. Alver, M. Baker, C. Loizides, and P. Steinberg. The PHOBOS Glauber Monte Carlo. 5 2008.

[15] B. Alver and G. Roland. Collision geometry fluctuations and triangular flow in heavy-ion collisions. *Phys. Rev. C*, 81:054905, 2010. [Erratum: Phys.Rev.C 82, 039903 (2010)].

[16] R. Nouicer. New State of Nuclear Matter: Nearly Perfect Fluid of Quarks and Gluons in Heavy Ion Collisions at RHIC Energies. *Eur. Phys. J. Plus*, 131(3):70, 2016.

[17] J. Bartke et al. Neutral strange particle production in sulphur sulphur and proton sulphur collisions at 200-GeV/nucleon. *Z. Phys. C*, 48:191–200, 1990.

[18] E. Andersen et al. Strangeness enhancement at mid-rapidity in Pb Pb collisions at 158-A-GeV/c. *Phys. Lett. B*, 449:401–406, 1999.

[19] B.I. Abelev et al. Enhanced strange baryon production in Au + Au collisions compared to p + p at s(NN)**(1/2) = 200-GeV. *Phys. Rev. C*, 77:044908, 2008.

[20] Betty Bezverkhny Abelev et al. Multi-strange baryon production at mid-rapidity in Pb-Pb collisions at $\sqrt{s_{NN}}$ = 2.76 TeV. *Phys. Lett. B*, 728:216–227, 2014. [Erratum: Phys.Lett.B 734, 409–410 (2014)].

[21] J. Adams, C. Adler, M. M. Aggarwal, Z. Ahammed, J. Amonett, B. D. Anderson, M. Anderson, D. Arkhipkin, G. S. Averichev, S. K. Badyal, and et al. Evidence from d+Au Measurements for Final-State Suppression of High-pTHadrons inAu+AuCollisions at RHIC. *Physical Review Letters*, 91(7), Aug 2003.

[22] Ning-Bo Chang, Yasuki Tachibana, and Guang-You Qin. Nuclear modification of jet shape for inclusive jets and γ-jets at the LHC energies. *Phys. Lett. B*, 801:135181, 2020.

[23] Nihar Ranjan Sahoo. Measurement of γ+jet and π^0+jet in central Au+Au collisions at $\sqrt{s_{\mathrm{NN}}}$ = 200 GeV with the STAR experiment. 8 2020.

[24] Vardan Khachatryan et al. Charged-particle nuclear modification factors in PbPb and pPb collisions at $\sqrt{s_{\mathrm{N\,N}}} = 5.02$ TeV. *JHEP*, 04:039, 2017.

[25] Albert M Sirunyan et al. Nuclear modification factor of D^0 mesons in PbPb collisions at $\sqrt{s_{\mathrm{NN}}} = 5.02$ TeV. *Phys. Lett. B*, 782:474–496, 2018.

[26] Albert M Sirunyan et al. Measurement of the $B^{\pm}$ Meson Nuclear Modification Factor in Pb-Pb Collisions at $\sqrt{s_{NN}} = 5.02$ TeV. *Phys. Rev. Lett.*, 119(15):152301, 2017.

[27] Albert M Sirunyan et al. Measurement of prompt and nonprompt charmonium suppression in PbPb collisions at 5.02 TeV. *Eur. Phys. J. C*, 78(6):509, 2018.

[28] Agnes Mocsy, Peter Petreczky, and Michael Strickland. Quarkonia in the Quark Gluon Plasma. *Int. J. Mod. Phys. A*, 28:1340012, 2013.

[29] J.J. Aubert et al. Experimental Observation of a Heavy Particle J. *Phys. Rev. Lett.*, 33:1404–1406, 1974.

[30] J.E. Augustin et al. Discovery of a Narrow Resonance in e^+e^- Annihilation. *Phys. Rev. Lett.*, 33:1406–1408, 1974.

[31] Estia Eichten, S. Godfrey, Hanna Mahlke, and Jonathan Rosner. Quarkonia and their transitions. *Reviews of Modern Physics*, 80, 02 2007.

[32] J. Beringer et al. Review of Particle Physics (RPP). *Phys. Rev. D*, 86:010001, 2012.

[33] Bo Liu and Yu-Bing Dong. Quark binding potential and Debye screening length. *Commun. Theor. Phys.*, 26:425–432, 1996.

[34] T. Matsui and H. Satz. J/ψ suppression by quark-gluon plasma formation. *Phys. Lett. B*, 178:416, 1986.

[35] A. Adare, S. Afanasiev, C. Aidala, et al. J/ψ suppression at forward rapidity in Au+Au collisions at $\sqrt{s_{NN}} = 200$ GeV. *Phys. Rev. C*, 84:054912, Nov 2011.

[36] Xiaojian Du and Ralf Rapp. Sequential Regeneration of Charmonia in Heavy-Ion Collisions. *Nucl. Phys.*, A943:147–158, 2015.

[37] Betty Bezverkhny Abelev et al. Centrality, rapidity and transverse momentum dependence of J/ψ suppression in PbPb collisions at $\sqrt{s_{\rm NN}}$ = 2.76TeV. 2013. Submitted to Phys. Lett. B.

[38] Jaroslav Adam et al. J/ψ suppression at forward rapidity in Pb-Pb collisions at $\sqrt{\mathbf{s}_{\rm NN}} = \mathbf{5.02}$ TeV. 2016.

[39] A. Adare, S. Afanasiev, C. Aidala, N.N. Ajitanand, Y. Akiba, et al. J/ψ suppression at forward rapidity in AuAu collisions at $\sqrt{s_{\rm NN}}$ = 200GeV. *Phys. Rev. C*, 84:054912, 2011.

[40] R. Vogt. Cold Nuclear Matter Effects on J/ψ and Y Production at energies available at the CERN Large Hadron Collider (LHC). *Phys. Rev. C*, 81:044903, 2010.

[41] B. Alessandro et al. Charmonium production and nuclear absorption in p A interactions at 450-GeV. *Eur. Phys. J. C*, 33:31–40, 2004.

[42] E.G. Ferreiro, F. Fleuret, J.P. Lansberg, and A. Rakotozafindrabe. Impact of the Nuclear Modification of the Gluon Densities on J/ψ production in pPb collisions at $\sqrt{s_{NN}} = 5$ TeV. *Phys. Rev. C*, 88(4):047901, 2013.

[43] R. Vogt. Shadowing effects on J/ψ and Y production at energies available at the CERN Large Hadron Collider. *Phys. Rev. C*, 92(3):034909, 2015.

[44] Francois Arleo and Stephane Peigne. J/ψ suppression in p-A collisions from parton energy loss in cold QCD matter. *Phys. Rev. Lett.*, 109:122301, 2012.

[45] François Arleo, Rodion Kolevatov, Stéphane Peigné, and Maryam Rustamova. Centrality and pT dependence of J/psi suppression in proton-nucleus collisions from parton energy loss. *JHEP*, 05:155, 2013.

[46] M. Cacciari, S. Frixione, M.L. Mangano, P. Nason, and G. Ridolfi. QCD analysis of first b cross-section data at 1.96-TeV. *JHEP*, 07:033, 2004.

[47] Matteo Cacciari, Stefano Frixione, and Paolo Nason. The p(T) spectrum in heavy flavor photoproduction. *JHEP*, 03:006, 2001.

[48] R. Aaij et al. First observation of $B_s^0 \to J/\psi f_0(980)$ decays. *Physics Letters B*, 698(2):115 – 122, 2011.

[49] M.B. Einhorn and S.D. Ellis. Hadronic Production of the New Resonances - Are Gluons Important? *Phys. Rev. Lett.*, 34:1190–1193, 1975.

[50] J.P. Lansberg. On the mechanisms of heavy-quarkonium hadroproduction. *Eur. Phys. J. C*, 61:693–703, 2009.

[51] Harald Fritzsch. Producing Heavy Quark Flavors in Hadronic Collisions: A Test of Quantum Chromodynamics. *Phys. Lett. B*, 67:217–221, 1977.

[52] Geoffrey T. Bodwin, Eric Braaten, and Jungil Lee. Comparison of the color-evaporation model and the NRQCD factorization approach in charmonium production. *Phys. Rev. D*, 72:014004, 2005.

[53] Mathias Butenschoen and Bernd A. Kniehl. J/ψ production in NRQCD: A global analysis of yield and polarization. *Nucl. Phys. B Proc. Suppl.*, 222-224:151–161, 2012.

[54] A. Andronic et al. Heavy-flavour and quarkonium production in the LHC era: from proton–proton to heavy-ion collisions. *Eur. Phys. J. C*, 76(3):107, 2016.

[55] F. Abe et al. J/ψ and $\psi(2S)$ production in $p\bar{p}$ collisions at $\sqrt{s} = 1.8$ TeV. *Phys. Rev. Lett.*, 79:572–577, 1997.

[56] N. Brambilla et al. Heavy quarkonium physics. 12 2004.

[57] R. Aaij et al. Measurement of J/ψ production in pp collisions at $\sqrt{s}$ = 7TeV. *Eur. Phys. J. C*, 71:1645, 2011.

[58] B. Abelev, A.Abrahantes Quintana, D. Adamova, A.M. Adare, M.M. Aggarwal, et al. J/ψ polarization in pp collisions at $\sqrt{s}$ = 7TeV. *Phys. Rev. Lett.*, 108:082001, 2011.

[59] Yan-Qing Ma, Kai Wang, and Kuang-Ta Chao. $J/\psi(\psi')$ production at the Tevatron and LHC at $\mathcal{O}(\alpha_s^4 v^4)$ in nonrelativistic QCD. *Phys. Rev. Lett.*, 106:042002, 2011.

[60] J.P. Lansberg. $\Upsilon(2S)$ production in proton-proton collisions at RHIC, Tevatron and LHC energies. *PoS*, ICHEP2012:293, 2013.

[61] P. Artoisenet, John M. Campbell, J.P. Lansberg, F. Maltoni, and F. Tramontano. Y Production at Fermilab Tevatron and LHC Energies. *Phys. Rev. Lett.*, 101:152001, 2008.

[62] Anthony D. Frawley, T. Ullrich, and R. Vogt. Heavy flavor in heavy-ion collisions at RHIC and RHIC II. *Phys. Rept.*, 462:125–175, 2008.

[63] Mathias Butenschoen and Bernd A. Kniehl. J/ψ polarization at Tevatron and LHC: Nonrelativistic-QCD factorization at the crossroads. *Phys. Rev. Lett.*, 108:172002, 2012.

[64] Bin Gong, Lu-Ping Wan, Jian-Xiong Wang, and Hong-Fei Zhang. Polarization for Prompt J/ψ and ψ(2S) Production at the Tevatron and LHC. *Phys. Rev. Lett.*, 110(4):042002, 2013.

[65] Kuang-Ta Chao, Yan-Qing Ma, Hua-Sheng Shao, Kai Wang, and Yu-Jie Zhang. J/ψ Polarization at Hadron Colliders in Nonrelativistic QCD. *Phys. Rev. Lett.*, 108:242004, 2012.

[66] Roel Aaij et al. Study of J/ψ Production in Jets. *Phys. Rev. Lett.*, 118(19):192001, 2017.

[67] Reggie Bain, Lin Dai, Adam Leibovich, Yiannis Makris, and Thomas Mehen. NRQCD Confronts LHCb Data on Quarkonium Production within Jets. *Phys. Rev. Lett.*, 119(3):032002, 2017.

[68] Johan Alwall, Michel Herquet, Fabio Maltoni, Olivier Mattelaer, and Tim Stelzer. MadGraph 5 : Going Beyond. *JHEP*, 06:128, 2011.

[69] Mathias Butenschoen and Bernd A. Kniehl. World data of J/psi production consolidate NRQCD factorization at NLO. *Phys. Rev. D*, 84:051501, 2011.

[70] Mathias Butenschoen and Bernd A. Kniehl. Next-to-leading-order tests of NRQCD factorization with J/ψ yield and polarization. *Mod. Phys. Lett. A*, 28:1350027, 2013.

[71] Geoffrey T. Bodwin, Hee Sok Chung, U-Rae Kim, and Jungil Lee. Fragmentation contributions to J/ψ production at the Tevatron and the LHC. *Phys. Rev. Lett.*, 113(2):022001, 2014.

[72] François Arleo. Quenching of Hadron Spectra in Heavy Ion Collisions at the LHC. *Phys. Rev. Lett.*, 119(6):062302, 2017.

[73] Morad Aaboud et al. Prompt and non-prompt J/ψ elliptic flow in Pb+Pb collisions at $\sqrt{s_{\rm NN}} = 5.02$ Tev with the ATLAS detector. *Eur. Phys. J. C*, 78(9):784, 2018.

[74] Vardan Khachatryan et al. Suppression and azimuthal anisotropy of prompt and nonprompt J/ψ production in PbPb collisions at $\sqrt{s_{\mathrm{NN}}} = 2.76$ TeV. *Eur. Phys. J. C*, 77(4):252, 2017.

[75] Shreyasi Acharya et al. J/ψ elliptic flow in Pb-Pb collisions at $\sqrt{s_{\mathrm{NN}}} = 5.02$ TeV. *Phys. Rev. Lett.*, 119(24):242301, 2017.

[76] Betty Bezverkhny Abelev et al. Azimuthal anisotropy of D meson production in Pb-Pb collisions at $\sqrt{s_{\mathrm{NN}}} = 2.76$ TeV. *Phys. Rev. C*, 90(3):034904, 2014.

[77] Serguei Chatrchyan et al. Measurement of the elliptic anisotropy of charged particles produced in PbPb collisions at nucleon-nucleon center-of-mass energy = 2.76TeV. *Phys. Rev. C*, 87:014902, 2013.

[78] Serguei Chatrchyan et al. Azimuthal anisotropy of charged particles at high transverse momenta in PbPb collisions at $\sqrt{s_{\mathrm{NN}}}$ = 2.76TeV. *Phys. Rev. Lett.*, 109:022301, 2012.

[79] M A Hone. The duoplasmatron ion source for the new CERN Linac preinjector. Technical Report CERN-PS-LR-79-37, CERN, Geneva, Nov 1979.

[80] W Fischer and J M Jowett. Ion Colliders. *Rev. Accel. Sci. Technol.*, 7(CERN-ACC-2015-0015):49–76. mult. p, Jan 2015.

[81] K. Aamodt et al. The ALICE experiment at the CERN LHC. *JINST*, 3:S08002, 2008.

[82] J. Schukraft. Heavy-ion physics with the ALICE experiment at the CERN Large Hadron Collider. *Philosophical Transactions: Mathematical, Physical and Engineering Sciences*, 370(1961):917–932, 2012.

[83] G Aad et al. The ATLAS Experiment at the CERN Large Hadron Collider. *JINST*, 3:S08003. 437 p, 2008. Also published by CERN Geneva in 2010.

[84] R. Adolphi et al. The CMS experiment at the CERN LHC. *JINST*, 3:S08004, 2008.

[85] Jr. Alves, A.Augusto et al. The LHCb Detector at the LHC. *JINST*, 3:S08005, 2008.

[86] O Adriani et al. The LHCf detector at the CERN large hadron collider. *Journal of Instrumentation*, 3(08):S08006–S08006, aug 2008.

[87] G Anelli et al. The TOTEM experiment at the CERN large hadron collider. *Journal of Instrumentation*, 3(08):S08007–S08007, aug 2008.

[88] Malcolm Fairbairn and James L. Pinfold. MoEDAL – a new light on the high-energy frontier. *Contemporary Physics*, 58(1):1–24, 2017.

[89] G. L. Bayatian et al. CMS Physics: Technical Design Report Volume 1: Detector Performance and Software. 2006.

[90] V I Klyukhin, N Amapane, V Andreev, A Ball, B Cure, A Herve, A Gaddi, H Gerwig, V Karimaki, R Loveless, and et al. The CMS Magnetic Field Map Performance. *IEEE Transactions on Applied Superconductivity*, 20(3):152?155, Jun 2010.

[91] S Chatrchyan et al. Precise Mapping of the Magnetic Field in the CMS Barrel Yoke using Cosmic Rays. *JINST*, 5:T03021, 2010.

[92] Armen Tumasyan et al. The Phase-2 Upgrade of the CMS Tracker. 6 2017.

[93] H. Abramowicz et al. Measurement of shower development and its Molière radius with a four-plane LumiCal test set-up. *Eur. Phys. J. C*, 78(2):135, 2018.

[94] P. Adzic et al. Energy resolution of the barrel of the CMS electromagnetic calorimeter. *JINST*, 2:P04004, 2007.

[95] J. Man and et al. Cms technical design report for the phase 1 upgrade of the hadron calorimeter.

[96] Serguei Chatrchyan et al. The Performance of the CMS Muon Detector in Proton-Proton Collisions at $\sqrt{s} = 7$ TeV at the LHC. *JINST*, 8:P11002, 2013.

[97] M. Abbrescia et al. Beam test results on double-gap resistive plate chambers proposed for CMS experiment. *Nucl. Instrum. Meth. A*, 414:135–148, 1998.

[98] Vardan Khachatryan et al. The CMS trigger system. *JINST*, 12(01):P01020, 2017.

[99] J. Fulcher, J. Lingemann, D. Rabady, T. Reis, and H. Sakulin. The New Global Muon Trigger of the CMS Experiment. *IEEE Transactions on Nuclear Science*, 64(6):1467–1473, 2017.

[100] CMS Technical Design Report for the Level-1 Trigger Upgrade. 6 2013.

[101] A. Zabi et al. Triggering on electrons, jets and tau leptons with the CMS upgraded calorimeter trigger for the LHC RUN II. *JINST*, 11(02):C02008, 2016.

[102] Jonathan Fulcher, Joschka Lingemann, Dinyar Rabady, Thomas Reis, and Hannes Sakulin. The New Global Muon Trigger of the CMS Experiment. *IEEE Trans. Nucl. Sci.*, 64(6):1467–1473, 2017.

[103] Jean-Marc Andre et al. Performance of the new daq system of the cms experiment for run-2. pages 1–4, 06 2016.

[104] R. Fruhwirth. Application of Kalman filtering to track and vertex fitting. *Nucl. Instrum. Meth. A*, 262:444–450, 1987.

[105] Torbjörn Sjöstrand et al. An Introduction to PYTHIA 8.2. *Comput. Phys. Commun.*, 191:159–177, 2015.

[106] V.N. Ivanchenko. Geant4 toolkit for simulation of HEP experiments. *Nucl. Instrum. Meth. A*, 502:666–668, 2003.

[107] I.P. Lokhtin, L.V. Malinina, S.V. Petrushanko, A.M. Snigirev, I. Arsene, and K. Tywoniuk. Heavy ion event generator HYDJET++ (HYDrodynamics plus JETs). *Computer Physics Communications*, 180(5):779?799, May 2009.

[108] D. J. Lange. The EvtGen particle decay simulation package. *Nucl. Instrum. Meth. A*, 462:152, 2001.

[109] Marcin Konecki. Muon reconstruction and identification in CMS. *PoS*, EPS-HEP2009:131, 2009.

[110] A.M. Sirunyan et al. Performance of the CMS muon detector and muon reconstruction with proton-proton collisions at $\sqrt{s} = 13$ TeV. *JINST*, 13(06):P06015, 2018.

[111] A.M. Sirunyan et al. Particle-flow reconstruction and global event description with the CMS detector. *Journal of Instrumentation*, 12(10):P10003?P10003, Oct 2017.

[112] Ryan Atkin. Review of jet reconstruction algorithms. *J. Phys. Conf. Ser.*, 645(1):012008, 2015.

[113] Victor Coco, Pierre-Antoine Delsart, Juan Rojo-Chacon, Gregory Soyez, and Christian Sander. Jets and jet algorithms. In *HERA and the LHC: 4th Workshop on the Implications of HERA for LHC Physics*, pages 182–204, 3 2009.

[114] Matteo Cacciari, Gavin P. Salam, and Gregory Soyez. The anti-k_t jet clustering algorithm. *JHEP*, 04:063, 2008.

[115] Peter Berta, Martin Spousta, David W. Miller, and Rupert Leitner. Particle-level pileup subtraction for jets and jet shapes. *JHEP*, 06:092, 2014.

[116] Matteo Cacciari, Gavin P. Salam, and Gregory Soyez. The Catchment Area of Jets. *JHEP*, 04:005, 2008.

[117] The Heavy-Ion Dilepton PinG. Muon performance studies in 2018 pbpb tev data. CMS Note 2018/316, 2018.

[118] Vardan Khachatryan et al. Jet energy scale and resolution in the CMS experiment in pp collisions at 8 TeV. *JINST*, 12(02):P02014, 2017.

[119] D. Hangal Y. Chen, S. Obrasztsov. Jet performance in 2018 PbPb heavy ion run. CMS Analysis Note 2019/017, 2019.

[120] Albert M Sirunyan et al. Relative Modification of Prompt ψ(2S) and J/ψ Yields from pp to PbPb Collisions at $\sqrt{s_{NN}} = 5.02$ TeV. *Phys. Rev. Lett.*, 118(16):162301, 2017.

[121] Carlos Loureŋo, Hermine K. Wohri, Ilse Kratschmer, Johannes Brandstetter, Linlin Zhang, Pietro Faccioli, Valentin Knunz, and Wei Guo. Prompt J/ψ and ψ(2S) differential cross sections in pp collisions at $\sqrt{s} = 7$TeV. CMS Note AN-2014/003, 2014.

[122] Wouter Verkerke and David P. Kirkby. The RooFit toolkit for data modeling. *eConf*, C0303241:MOLT007, 2003. [,186(2003)].

[123] Albert M Sirunyan et al. Nuclear modification factor of charmonia in PbPb collisions at $\sqrt{s_{\mathrm{NN}}} = 5.02$ TeV. 2017.

[124] J.C. Mason and David C. Handscomb. *Chebyshev Polynomials*. Chapman and Hall/CRC, New York, 2002.

[125] N. Karjanto. Properties of chebyshev polynomials, 2020.

[126] M. Pivk and F.R. Le Diberder. ${}_s\mathcal{P}lot$: a statistical tool to unfold data distributions. *arxiv:physics/0402083*, 2005.

[127] Kyle Cranmer, George Lewis, Lorenzo Moneta, Akira Shibata, and Wouter Verkerke. HistFactory: A tool for creating statistical models for use with RooFit and RooStats. Technical Report CERN-OPEN-2012-016, Jan 2012.

[128] Kyle S. Cranmer. Kernel estimation in high-energy physics. *Comput. Phys. Commun.*, 136:198–207, 2001.

[129] Study of in-medium modification of dijets in PbPb collisions at 5.02 TeV. 8 2020.

[130] Tim Adye. Unfolding algorithms and tests using RooUnfold. In *PHYSTAT 2011*, pages 313–318, Geneva, 2011. CERN.

[131] G. D'Agostini. A Multidimensional unfolding method based on Bayes' theorem. *Nucl. Instrum. Meth. A*, 362:487–498, 1995.

[132] Production of prompt and nonprompt J/ψ mesons in jets in pp collisions at $\sqrt{s} =$ 5.02 TeV. Technical Report CMS-PAS-HIN-18-012, CERN, Geneva, 2018.

[133] S van der Meer. Calibration of the effective beam height in the isr. Technical Report CERN-ISR-PO/68-31, CERN, Geneva, 1968.

[134] Constantin Loizides, Jason Kamin, and David d'Enterria. Improved Monte Carlo Glauber predictions at present and future nuclear colliders. *Phys. Rev. C*, 97(5):054910, 2018. [Erratum: Phys.Rev.C 99, 019901 (2019)].

[135] Albert M Sirunyan et al. Study of J/ψ meson production inside jets in pp collisions at $\sqrt{s} = 8$ TeV. *Phys. Lett. B*, 804:135409, 2020.

[136] Albert M Sirunyan et al. Measurement of nuclear modification factors of Y(1S), Y(2S), and Y(3S) mesons in PbPb collisions at $\sqrt{s_{\mathrm{NN}}} = 5.02$ TeV. *Phys. Lett. B*, 790:270–293, 2019.

List of Figures

List of Tables

ECOLE DOCTORALE

Titre : Fragmentation des jets contenant un méson J/ψ dans les collisions PbPb et pp à 5 TeV dans CMS

Mots clés : Collisions d'ions lourds, plasma des quarks et des gluons, J/ψ, jets

Résumé : Le plasma des Quarks et des Gluons (QGP) est un état de la matiére dans lequel les quarks et les gluons sont asymptotiquement libres et non confinés dans les hadrons. Les collisions ultra relativistes d'ions lourds sont un outil unique pour produire le QGP en laboratoire. Il ne peut pas être directement observé, et des sondes, dont le méson J/ψ, sont donc utilisées pour mesurer ses propriétés. Cependant, la production de J/ψ n'est pas encore complètement comprise.
Dans cette thèse, la fragmentation de J/ψ en jets est mesurée en collisions pp et PbPb à une énergie au centre de masse de 5 TeV. Les fonctions de fragmentation de J/ψ prompts et non-prompts sont montrées et comparées aux modèles en pp. Le facteur de modification nucléaire de J/ψ dans les jets est également montré. Les résultats J/ψ-en-jets indiquent que les mésons J/ψ prompts sont produits dans des gerbes de partons et sont affectés par des processus de perte d'énergie en présence d'un milieu chaud, dense et interagissant fortement.

Title : Fragmentation of jets containing a J/ψ meson in pp and PbPb collisions at 5 TeV with the CMS detector

Keywords : Heavy-ion collisions, Quark-Gluon Plasma, J/ψ, jets

Abstract : The Quark-Gluon Plasma (QGP) is a state of matter where quarks and gluons are asymptotically free, and not confined in hadrons. Ultrarelativistic heavy-ion collisions are a unique tool to produce the QGP in laboratory frame. Since it cannot be directly seen, probes are used to measure its properties, one of which is the J/ψ meson. The J/ψ production, however, is still not completely understood.
In this thesis, the fragmentation of J/ψ in jets is measured in pp and PbPb collisions at a center-of-mass energy of 5 TeV. Prompt and nonprompt J/ψ fragmentation functions are shown and compared to the models in pp. The nuclear modification factor of J/ψ in jets is also shown. The J/ψ-in-jets results indicate that prompt J/ψ mesons are produced in parton showers and are affected by energy loss processes in the presence of a hot and dense strongly-interacting medium.

Institut Polytechnique de Paris
91120 Palaiseau, France